

7-1-2011

A variable compliance controller for cooperative vision guided robotic assembly

Kevin Ruybal

Follow this and additional works at: https://digitalrepository.unm.edu/me_etds

Recommended Citation

Ruybal, Kevin. "A variable compliance controller for cooperative vision guided robotic assembly." (2011).
https://digitalrepository.unm.edu/me_etds/51

This Thesis is brought to you for free and open access by the Engineering ETDs at UNM Digital Repository. It has been accepted for inclusion in Mechanical Engineering ETDs by an authorized administrator of UNM Digital Repository. For more information, please contact disc@unm.edu.

Kevin R. Ruybal

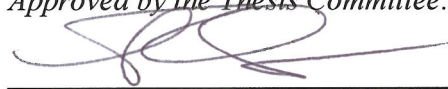
Candidate

Mechanical Engineering

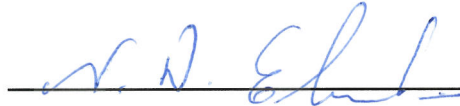
Department

This thesis is approved, and it is acceptable in quality and form for publication:

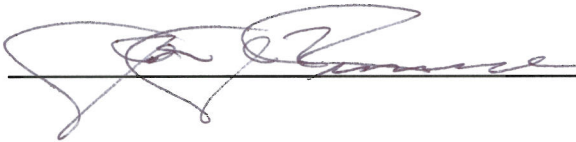
Approved by the Thesis Committee:



Dr. Ronald Lumia, Chairperson



Dr. Nader Ebrahimi



Dr. John Russell

**A VARIABLE COMPLIANCE CONTROLLER FOR COOPERATIVE
VISION GUIDED ROBOTIC ASSEMBLY**

BY

KEVIN R. RUYBAL

**PREVIOUS DEGREES
BACHELOR OF SCIENCE, MECHANICAL ENGINEERING
UNIVERSITY OF NEW MEXICO
MAY 2009**

THESIS

Submitted in Partial Fulfillment of the
Requirements for the Degree of
Master of Science in Mechanical Engineering

The University of New Mexico
Albuquerque, New Mexico

May, 2011

DEDICATION

This work is dedicated to the memory of my three grandfathers, Jose Benito Ruybal, Franklin P. Dibble, and Lawrence H. Smith, who have all passed away within a year of the completion of this thesis. This work would have been much more difficult had I not inherited their extraordinary aptitudes for math, engineering, and design. Moreover, I would not have had as many opportunities or be the person I am today without their lifetimes of hard work and dedication to their families. I am forever thankful for everything they have contributed to my life and I am privileged to have known them.

“If I have seen further, it is by standing on the shoulders of giants.”

- Isaac Newton

ACKNOWLEDGMENTS

I would like to thank everyone who contributed to the writing of this thesis. First and foremost, I would like to thank Dr. Ron Lumia, my advisor and thesis committee chair, who gave me the opportunity to work in UNM's robotics research laboratory. The experience I gained from this work and from his continuous guidance and advice will be some of the most important things I take away from graduate school. I am also most appreciative of the time and effort he invested in the writing and review of this thesis. I would also like to thank my committee members, Dr. John Russell and Dr. Nader Ebrahimi, for everything they have taught me in the classroom and for taking the time to review this work.

I would like to thank Dr. Robert W. Duffner of the Air Force Research Laboratory for being a valuable mentor. I have been privileged to work in his office for the last four years, and I have learned a lot from him about all aspects of life. The decision to continue my education and achieve a master's degree was largely due to his encouragement, and I am thankful for that. I would also like to thank Elizabeth Luebchow of the AFRL Phillips Research Site Technical Library for her help in locating the conference papers and journal articles needed to conduct my state of the art research. This provided me access to much more information than I could have obtained on my own.

Finally, I would especially like to thank my mom, dad, brother, sisters, in-laws, and wonderful wife, Sarah, for all of their support, interest, and understanding of the time commitment required by this work. Without Sarah's company, the long hours of night-time research in the lab would have been much less bearable. Love and thanks to all.

This work was supported by the US Department of Energy under Grant #DE-FG52-2004NA25590.

**A VARIABLE COMPLIANCE CONTROLLER FOR COOPERATIVE
VISION GUIDED ROBOTIC ASSEMBLY**

BY

KEVIN R. RUYBAL

ABSTRACT OF THESIS

Submitted in Partial Fulfillment of the
Requirements for the Degree of
Master of Science in Mechanical Engineering

The University of New Mexico
Albuquerque, New Mexico

May, 2011

**A VARIABLE COMPLIANCE CONTROLLER FOR COOPERATIVE VISION
GUIDED ROBOTIC ASSEMBLY**

by

Kevin R. Ruybal

B.S., Mechanical Engineering, University of New Mexico, 2009

M.S., Mechanical Engineering, University of New Mexico, 2011

ABSTRACT

Successful peg and hole insertion systems allow the peg to translate and rotate to accommodate contact forces that arise from different contact states between the peg and hole during assembly. Typically, a position or force controlled robotic insertion system is fitted with a specialized mechanically compliant wrist, known as a remote center compliance (RCC) device, to allow the system to accommodate the forces [1]. Using design principles similar to those developed for the RCC, a variable compliance control system is produced in this thesis. This control system allows a dual seven degree of freedom robotic arm system to cooperatively perform rigid peg and hole assembly with human-like performance at a 100% success rate without the use of mechanically compliant attachments. Additionally, a novel finite state machine with visual feedback is developed to improve the positional accuracy of the robots' impedance controllers and boost the reliability and performance of the entire system. Finally, a unique design process is developed to obtain the optimum variable compliance controller control law equations with respect to task success, reliability, and coupled robotic arm stability.

TABLE OF CONTENTS

LIST OF FIGURES	x
LIST OF TABLES	xiii
CHAPTER 1: INTRODUCTION.....	1
1.1 The General Robotic Peg and Hole Problem and Proposed Solution.....	1
1.2 Goal.....	4
1.3 Contribution	4
1.4 Scope of Research.....	5
1.5 Thesis Organization	5
CHAPTER 2: LITERATURE SURVEY.....	7
2.1 Passive Compliance: The RCC.....	8
2.2 Active Compliance: Impedance Control.....	14
2.3 System Design for Peg and Hole Assembly	21
2.4 State of the Art Contribution	25
CHAPTER 3: HARDWARE OVERVIEW.....	27
CHAPTER 4: IMPEDANCE CONTROLLER.....	31
4.1 Impedance Controller Functionality	33
4.2 Impedance Controller Performance	39
CHAPTER 5: SYSTEM MODELING.....	48
5.1 Peg and Hole Kinematic Analysis	48
5.2 Coupled Impedance Control Stability Analysis.....	79
CHAPTER 6: SYSTEM LEVEL CONTROLLERS.....	90
6.1 Vision System.....	90
6.2 Visual Trajectory Compensation Controller.....	95
6.3 Variable Compliance Controller	106
CHAPTER 7: PARAMETER OPTIMIZATION.....	111
7.1 Applying the Stability Criteria.....	111
7.2 System Assumptions and Dimensions.....	114
7.3 Introduction to <i>ModeFrontier</i>	119

7.4 Finding Optimum Parameters with <i>ModeFrontier</i>	121
7.5 Defining Acceptable Compliance Ranges	130
CHAPTER 8: SYSTEM PERFORMANCE.....	136
CHAPTER 9: CONCLUSION.....	145
9.1 Review of Thesis	145
9.2 Future Work.....	146
REFERENCES.....	148

LIST OF FIGURES

Figure 2.1.	Jamming and Wedging Failure Diagrams	11
Figure 2-2.	Compliant Structure RCC.	12
Figure 3-1.	Robot System Hardware Diagram.	27
Figure 3-2.	WAM Reading <i>Simulink</i> Model.....	29
Figure 3-3.	WAM Writing <i>Simulink</i> Model.....	30
Figure 4-1.	Basic <i>Simulink</i> Impedance Controller.....	32
Figure 4-2.	Compliance Center Location Definition.	37
Figure 4-3.	Compliance Center Behavior Demonstration.	38
Figure 4-4.	Complete <i>Simulink</i> Impedance Controller.	39
Figure 4-5.	Impedance Controller Trajectory Following Performance.	40
Figure 4-6.	Impedance Controller Lateral Force vs. Displacement Relationship.....	43
Figure 4-7.	Impedance Controller Rotational Force vs. Displacement Relationship.	44
Figure 4-8.	Impedance Controller Gain vs. Physical Lateral Stiffness Plot.	46
Figure 4-9.	Impedance Controller Gain vs. Physical Rotational Stiffness Plot.....	47
Figure 5-1.	Stages of Successful Peg and Hole Assembly.	48
Figure 5-2.	Chamferless Peg and Hole Insertion Strategy.....	50
Figure 5-3.	Peg and Hole Wiggle Angle.....	54
Figure 5-4.	Diagram of a Wedged Peg and Hole.....	55
Figure 5-5.	Minimum Friction Angle for Wedging	56
Figure 5-6.	Lateral Displacement vs. Rotational Error.....	58
Figure 5-7.	Wedging Diagram	60
Figure 5-8.	Jamming Diagram	61

Figure 5-9. Chamfer Crossing Diagram.....	64
Figure 5-10. Chamfer Angle Variation.....	66
Figure 5-11. Chamfer Crossing Free Body Diagram.....	67
Figure 5-12. One-Point Contact Diagram.....	72
Figure 5-13. Two-Point Contact Diagram.....	75
Figure 5-14. Coupled Impedance Control SMD Model.....	82
Figure 5-15. Graphical Representation of Coupled Stability Constraints.....	88
Figure 6-1. Two Camera Placement Strategy.....	92
Figure 6-2. Images After Color Filtering.....	93
Figure 6-3. <i>Simulink</i> Image Processing Model.....	94
Figure 6-4. Vision Integration Block Diagram.....	97
Figure 6-5. <i>Simulink</i> Visual PID Controller Simulation.....	98
Figure 6-6. FSM Visual Compensation State Diagram.....	99
Figure 6-7. Error Compensation State Diagram.....	100
Figure 6-8. <i>Simulink</i> FSM Visual Controller Simulation.....	101
Figure 6-9. Visual Controller Step Response Comparison.....	102
Figure 6-10. Visual Controller Trajectory Following Performance.....	103
Figure 6-11. Actual System Trajectory Following Performance.....	106
Figure 6-12. Impedance Controller Stiffness Gain Diagram.....	107
Figure 6-13. Variable Compliance Controller Block Diagram.....	110
Figure 6-14. Complete <i>Simulink</i> System Controller.....	110
Figure 7-1. Coupled Stability Constraints on Experimental System.....	113
Figure 7-2. Experimental Peg and Hole Dimensions.....	119

Figure 7-3.	ModeFrontier Workflow Model.....	122
Figure 7-4.	Spider Chart of Optimized Parameters	124
Figure 7-5.	Parallel Coordinates Plot for All Experiments.....	126
Figure 7-6.	Filtered Parallel Coordinates Plot – Good Results.....	127
Figure 7-7.	Filtered Parallel Coordinates Plot – Desired RCC.....	128
Figure 7-8.	Filtered Parallel Coordinates Plot – Low Stiffness.....	129
Figure 7-9.	Contour Plot of Jamming Diagram Parameter Check.....	131
Figure 7-10.	Labeled Contour Plot	132
Figure 8-1.	Images From Successful Experimental Insertion.....	137
Figure 8-2.	Insertion Force History Comparison.....	138
Figure 8-3.	Variable Compliance Controller Output	139
Figure 8-4.	Free-space vs. Insertion Trajectory Following Performance	140
Figure 8-5.	Insertion Force History from Position Controlled Failure	142
Figure 8-6.	Images From Failed Experimental Insertion.....	143
Figure 8-7.	Insertion Force History from Jamming Failure.....	144

LIST OF TABLES

Table 4-1. Trajectory Following Percent Error as a Function of Stiffness	41
Table 4-2. Lateral Impedance Controller Gains and Physical Equivalents	45
Table 4-3. Rotational Impedance Controller Gains and Physical Equivalents	47

CHAPTER 1

INTRODUCTION

This chapter presents a general discussion of the automated peg and hole assembly problem. Then, the research goals and contributions of this thesis are explained. This is followed by a description of the scope of the research presented and an overview of how the rest of the thesis is organized.

1.1 The General Robotic Peg and Hole Problem and Proposed Solution

Robots have become increasingly common in the manufacturing environment. This is mostly due to the high level of speed, consistency, and reliability at which they can perform tasks for long periods of time. All of these factors can remarkably increase the efficiency of any type of factory, and spare humans from injuries due repetitive stress and fatigue. However, robots cannot currently be used to perform all kinds of assembly operations. For example, tasks that require significant interaction with an external rigid environment, a human, or another robot are typically not considered for robotic automation. This is due to the error and external force rejection limitations of position-based robot controllers, which are most common in manufacturing. As a result, it is desirable to design new ways in which robots can be applied to these types of applications.

The general peg and hole assembly problem embodies many aspects that are difficult for robots to perform. Among the most difficult are the varying position and external force constraints caused by different types of constrained motion that vary as a

function of insertion depth. Thus, designing a system that can perform general peg and hole assembly can most likely be applied to a broad range of assembly tasks that require the robot to work in an environment that is constrained by mechanical contact. In manufacturing, this is directly applicable to many types of two-part mating tasks that can be modeled as a variations of the peg and hole problem. As a result, the peg and hole assembly problem has been widely studied and is used as a means to judge the performance of robotic manufacturing systems. This is why peg and hole assembly was chosen as the main focus of this thesis.

The success of any peg and hole assembly system is determined by the internal forces generated as a result of the contact between the parts being assembled. How well the total system is able to accommodate these forces is a strong indication of the system's probability of success. Positioning error and misalignment create reaction forces between the peg and the hole that can cause the parts, or their supports, to break, jam, or wedge, resulting in failure. To avoid these problems, mechanically compliant fixtures have been used to support the parts during assembly. These fixtures absorb errors by allowing the peg to physically deflect in the presence of contact forces. The most common type of compliant fixture is the remote center compliance (RCC) device [1]. The RCC is a compliant wrist that is attached to the peg's manipulator to aid in peg and hole operations. While quite successful, the RCC exhibits several limitations which are discussed in more detail in section 2.1.

When the peg and hole are to be assembled by a robotic system, there are additional complications. Robotic peg and hole assembly is an interactive process that requires a robotic manipulator to come into physical contact with its environment. This

can cause problems for the typical position controlled robots currently used in industry. Position control algorithms often lack robustness to large positional errors caused by interference or external contact, which can lead to large control forces and controller instability. Additionally, the inevitable end effector position error that results from less than infinite encoder resolution, drivetrain dynamics, and workspace inconsistencies can cause the assembly process to fail for the same physical reasons that justify the use of an RCC. Since this positional error is often inconsistent, the total system may be successful sometimes, but fail at other times even though the initial conditions for all the operations appear identical. This “fragile” quality associated with standard position controlled robots limits their applications in automated assembly.

For a robot to interact with its environment, or another robot, the controller must maintain a predefined force relationship between the two systems. Impedance control is one method that accomplishes this task, and it allows the robot to respond to external disturbances in a controlled way. This style of control uses a linear relation between the position of the robot’s end effector and joint torques, which manifests behavior comparable to an end effector that is compliantly supported by linear lateral and rotational springs that can be varied by changing controller gain parameters. By dynamically modifying the compliance parameters of the robot’s impedance controller, the robot will exhibit all of the benefits of an RCC equipped system during peg and hole assembly, without any of the physical limitations. Also, the torque controlled nature of impedance control removes the position controlled “fragility” from the robotic system. The result is a robust, self-contained robotic system for peg and hole assembly tasks .

1.2 Goal

The goal of this thesis research was to develop a reliable and highly stable dual seven degree of freedom (DOF) robot system to cooperatively perform rigid peg and hole assembly tasks with a very high probability of success and human-like performance. This was to be accomplished through the design of a variable compliance controller with visual feedback that exhibits behavior similar to fixed mechanical systems used for robotic peg and hole assembly in industry. The variables of compliance were to be optimized with respect to coupled robot controller stability and the physical mechanics of peg and hole assembly process to produce the desired system reliability and performance.

1.3 Contribution

The goal of this thesis was to produce a robust, robotic assembly system to perform peg and hole assembly with a greater probability of success than other systems by continuously varying each robot's compliance to meet the requirements of the assembly process mechanics and controller stability. This research represents a new approach to the peg and hole assembly problem by combining classic design for manufacturing techniques with modern robotic and computational capabilities. Time tested RCC principles were improved and integrated into the robot controller to aid the assembly process without the use of additional force sensors. The proposed optimization technique can be applied to other robotic assembly systems to identify parameter values that increase the performance of the entire system. This technique provides a tangible methodology to fully design the compliance variables that were tuned by trial and error in the past, resulting in a fully engineered system.

1.4 Scope of Research

The primary focus of this research was placed on the design and optimization process of the variable compliance controller that was unique to this system. This included the design of the compliance controller itself and the optimization process used to define its optimum controller parameters. Performing this work required the adaptation of many other areas of research that have already been well established. For example, the aim of this thesis was not to increase the state-of-the-art in impedance controllers, vision systems, peg and hole jamming analysis, or coupled system stability. Instead, each of these individual topics was modified and adapted to benefit the novel variable compliance controller, which was the true contribution of this work. The variable compliance controller increases the state-of-the-art of peg and hole assembly, and was the main focus of this thesis. The development of a controller network that uses visual feedback to perform peg and hole assembly with behavior that is analogous to a variable RCC was a completely new research topic. As a result, the rest of this thesis will be dedicated to the development of this controller network.

1.5 Thesis Organization

Chapter 2 presents an overview of the current research that represents the state-of-the-art in peg and hole assembly as well as adaptive impedance control systems. Chapter 3 briefly describes the hardware used to research and develop the final system. Chapter 4 describes the design and implementation of the variable impedance controller used to perform the robot control aspects of the final system. Chapter 5 derives the equations of the physical system model. This model is used to obtain the optimum control parameters

for the variable compliance controller when used to assemble the experimental peg and hole parts. Chapter 6 explains the design of the control computer based system level controllers, including the visual trajectory compensation controller and the variable compliance controller. The optimum parameters for the variable compliance controller are found using the *modeFrontier* software package in Chapter 7. Chapter 8 presents the performance of the completed system, and Chapter 9 concludes the thesis with a review and description of future work.

CHAPTER 2

LITERATURE SURVEY

Robots have become a major component of the manufacturing industry. Due to their accuracy and unparalleled repeatability, they are becoming more prominent as technology becomes more sophisticated. New technologies are allowing robots to perform more and more tasks that were previously deemed too challenging for automation and reserved exclusively for human workers. As a result, the goal of achieving human-like performance in general assembly tasks has become the target for a major section of manufacturing and robotics research. One of the most common areas of research is the peg and hole assembly task due to its far reaching applications through many manufacturing processes. Peg and hole assembly is typically performed in two independent stages, *gross motion* and *fine motion*. Gross motion refers to the large ballistic movements that move the peg from its starting position to a point very close to the hole. These motions are performed in free-space, without any interaction between the robot and its environment. Fine motion refers to the rest of the movement that actually performs the assembly of the two parts [1, 2]. This is the most studied part of the assembly process due to the challenges that arise from the interaction between the robot and its environment during rigidly constrained movements. The main objective of all fine motion research is to implement new hardware, software, or motion strategies to achieve human-like performance during the interaction phase of assembly, where good performance is defined by movements that are fast and robust to tight tolerances and robot positional uncertainty. This goal is particularly important because the tolerances of

the parts being assembled are often smaller than the resolution of the robot controllers [3].

2.1 Passive Compliance: The RCC

Most of the research done in the area of peg and hole problems appears to follow the same form. First, the desired peg and hole system is modeled in two or three dimensions so that contact forces resulting from different peg and hole contact configuration states can be predicted based on preexisting knowledge of the system's geometry. For the specific case of a cylindrical peg and hole, it has been shown using screw theory that the three dimensional problem can essentially be solved using a two-dimensional study [4]. The next step in typical research produces a piece of passive hardware, software, or a motion strategy to accommodate the predicted contact forces to facilitate successful assembly of the two parts in the presence of reasonable positioning errors. The first person to present a thorough study on this topic was Whitney in 1982 [5]. He developed a chamfered peg and hole contact model and presented a passive compliant wrist that could be attached to a robot to aid in assembly. This wrist was the first remote center compliance device, or RCC. He referred to the flexibility and stiffness designed into the RCC as "engineered compliance," which implies that the stiffness of the system must be carefully designed and integrated into the robot as a system to produce desirable behavior.

There are two different goals when designing the engineered compliance settings of a system. The first goal is called "consistent compliance," which aspires to ensure that all contact forces remain bounded by leaving some directions of the robot's movement

position controlled while the directions perpendicular to environmental constraints are force controlled. The second and most researched goal is called “error corrective compliance,” which designs compliance values such that contact forces always push the peg and hole closer towards successful assembly [6]. This goal is the most useful when there is a specific final configuration that must be achieved for the system to be successful. Thus, error corrective compliance is the main focus of most peg and hole research.

There is always a certain amount of inevitable compliance and positional uncertainty built into any robot due to flexibility of the robot links, back-drivability of the joints, backlash in the drivetrain, etc. Some work has been done to utilize these perceived shortcomings to facilitate peg and hole assembly. One such algorithm was proposed to find robot configurations that combine the individual joint uncertainties and compliances in such a way as to create an acceptable level of uncertainty and compliance at the end effector of the entire system [7]. While this approach is novel, it is unlikely that the available range and resolution of possible compliance outcomes would be sufficient to meet the goals of a specific task. Since there has been significant effort invested in modeling to be used as a guide for the selection of compliance parameters, it is naturally desirable to have a system capable of exactly performing the engineered compliant behavior when implementing a compliant system design.

Additionally, the ability to accurately and consistently control the compliance of an assembly system is vital to its reliability. Whitney showed that the success of peg and hole assembly depends on how the parts interact with each other as they pass through different contact states during insertion. Each contact state presents different internal

forces which can cause two specific modes of failure as shown in figure 2-1. The first mode is called wedging. Wedging occurs when contact forces become compressive forces that store energy and hold a peg in its hole. To avoid this condition, the robot must minimize the angular error between the peg and its hole at all times. The second condition is called jamming, which occurs when the resultant insertion force is too far off of the insertion axis to allow the assembly to be completed. Jamming is avoided by allowing the peg and hole to rotate and correct for misalignment. This movement will change the relationship between the insertion force, lateral force, and reaction moment applied to the peg and change the direction of the single resultant force [1]. The RCC is essentially an error absorber that provides a specific six DOF (three lateral and three rotational) compliance for a peg and hole during assembly to allow the peg to move in response to reaction forces and avoid these failure conditions [1]. The RCC performs two functions to achieve this goal. First, it moves the peg's center of compliance, or the "pivot" point on the peg at which it can independently rotate and translate, to a point that minimizes contact forces and errors by allowing the peg to more easily reposition itself relative to the hole. Second, the RCC physically allows the peg to rotate and translate about the center of compliance with a specific stiffness. By imposing a single center of compliance, the RCC allows the system to be largely governed by the general six element vector representation of the six DOF stiffness applied to the peg. This is a great benefit to the system designer since the number of relevant compliance variables drops from a full six-by-six matrix to a diagonalized compliance matrix with six non-zero terms [8]. This simplifies the compliance selection considerably and makes the design process more tangible and understandable for humans.

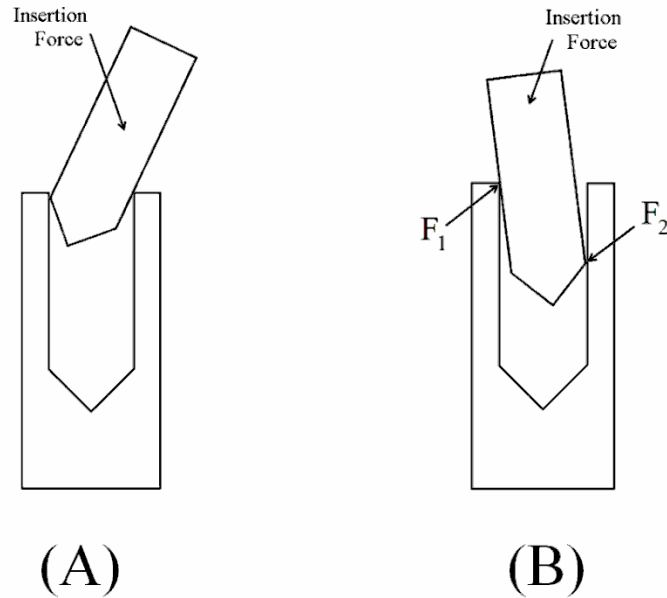


Figure 2-1. General diagrams of failure due to jamming (A) and wedging (B).

There are two different generic types of RCCs presented in research literature. The first type is based on a series of three parallel platforms that are connected by flexible links. The upper platform connects to the robot's wrist while the bottom platform connects to the peg that is to be inserted. This combination of linkages allows the center of compliance, which is typically located at the tip of the peg held by the RCC, to both rotate and translate as a reaction to contact forces. The second generic type of RCC is called the compliant structure RCC. This type of RCC is easily adapted to absorb errors in all six DOF so it is exclusively used in manufacturing. All commercial RCCs are compliant structures that utilize three or six shear pads to allow one side of the RCC to rotate and translate relative to the other. Shear pads are stacks of rubber and metal disks organized in alternating layers that deform laterally much more easily than they do axially in a compressive sense. This configuration allows the RCC to be easily modeled

for small deflections using a set of linear equations. Figure 2-2 shows a simplified example of a compliant structure RCC.

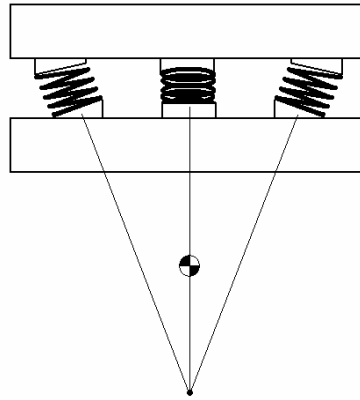


Figure 2-2. A compliant structure RCC with three shear pads (shown as springs) at rest. The shear pads allow the bottom platform and its attached peg to rotate and translate relative to the top platform about the compliance center.

While simple and currently used in some forms of manufacturing, the RCC still has many limitations. One of the biggest limitations is a result of the mechanical nature of the RCC. Since it is a mechanical addition to the robot and not part of its control system, it cannot help if the positional errors are so large that the mating surfaces of the peg and hole do not initially meet during assembly. The mechanical nature of the device also limits the total amount of error that can be absorbed since a compliant structure can only deform a limited distance. Also, current RCCs have a fixed compliance center location, which means they must be redesigned for each application. The RCC is not designed to be used in any orientation other than vertically downward without significant counter-weighting and redesign due to the effects of gravity. Also, an RCC can only prevent jamming since wedging is heavily dependent on initial error that is controlled by

the robot controller and not the RCC. Despite the success of the RCC, all of these limitations leave a lot to be desired by a robotic assembly system.

Some researchers have worked to create RCCs that are better suited for specific tasks. For example, Sturges and Laowattana developed the spatial remote center compliance (SRCC), which is a mechanical compliant wrist used to perform the peg and hole assembly of prismatic objects. This device differs from a typical RCC in that it allows an additional axial rotation of the peg to take place, which was designed to accommodate the non-axial symmetry of prismatic pegs [9, 10]. Another passive device, called the dynamic RCC, was designed to hold a peg during high-speed insertion. The purpose of this device was to stop the peg from bouncing along the chamfers of the hole after an impact. The dynamic RCC accomplished this by moving compliance center to the tip of the peg and reducing its virtual mass in the directions perpendicular to the walls of the hole [11]. Other RCC variants allow the user to manually adjust the position of the compliance center by inserting rods of varying stiffness into the shear pads of the RCC [12]. However, the vast majority of current research has shown that compliant control of the robot's end effector is a more viable solution to the peg and hole problem. This method of compliantly controlling the end effector of a robot through its joint controller's control law is called active compliance, as opposed to mechanical passive compliance.

Though active compliance implies that all compliant behavior is controlled by the robot's controller, some active compliance systems also employ mechanical components to achieve the desired behavior. One such controller was invented to control a light-weight, human-like robot arm called the DLR light-weight robot III [13]. This robot used joint torque feedback based impedance control to shape the robot's joint motor inertia

and equivalent potential energy using a system of state based controllers. This approach is called joint passivity control, and it allows the robot to be simultaneously controlled by joint torque and position using a single controller, resulting in high performance joint control from a weakly damped system. Another unique robot controller was implemented for the seven DOF MIA robot [14]. MIA stands for “Mechanical Impedance Adjuster” and it refers to a spring and brake system that is contained in each joint of the robot to mechanically apply impedance characteristics to the robot’s motion. This system demonstrated good results when interacting with humans, but it was quite complex. This complexity corresponds to low reliability and high cost, so the typical approach has been to impose compliant behavior using only the robot control strategy.

2.2 Active Compliance: Impedance Control

While the theory of back projection can be used to create an active compliance peg and hole assembly system that does not need feedback [15], active compliance is typically composed of a robust control strategy that allows the robot to interact with its environment in a controlled way using feedback from a sensor. There are many ways to achieve a controller that exhibits this kind of behavior. Raibert and Craig were among the first to do this with a hybrid force and position robot controller in 1981 [16]. Their system allowed the end effector of a robot to rigidly track position inputs in one direction and track desired force relationships in other directions using a force sensor mounted on the wrist of the robot. A similar control system defined a “configuration space” that limited forces and movements in some directions while allowing the robot to move freely in others. The resulting control strategy is similar to hybrid control with the exception

that it employs predictive “guarded moves” to move from one position to the next [17]. A more modern implementation of this system can be found in [18]. Whitney also developed a similar method of control in 1987. He called his system force feedback. Using force feedback, the robot is commanded with measured end effector force trajectories as an input instead of position or velocity commands [19]. Very successful variations of this algorithm are still currently used in manufacturing plants, such as Ford Motor Company, which uses a force controlled robot to assemble highly complex triple clutch transmissions [20]. However, force control naturally incurs a sensory delay, which typically makes these control systems relatively slow and increases the possibility of controller instability.

Other systems have incorporated computer vision to help fill the gaps in force feedback systems. One system, for example, implemented a visual PD controller to perform micro peg and hole assembly [21]. Due to the small scale of the assembly, a complex algorithm to retrieve depth information using focal length and an image Jacobian were used instead of taking force measurements. Other, more conventional systems used standard stereo vision along with six DOF robot arms to perform prismatic peg and hole assembly tasks [22]. Another less conventional system was developed to create object trajectories in image coordinates. These trajectories were then translated into Cartesian movements for the robots to follow without any feedback from other sensors [23]. A more practical system used computer vision to calibrate the tool of an assembly robot in an effort to reduce the positional uncertainty problem associated with peg and hole assembly [24]. These systems, and many others, all seem to use vision as a “look-then-act” system, in which measurements are taken and then applied to a trajectory

or a controller. These kinds of strategies do not use their vision systems to their greatest potential since the actual actions are performed without visual feedback. Thus, the resulting systems are not truly active.

There is another class of active compliance that seeks to emulate passive compliant behavior through an active system. These systems employ a controller that regulates a constant interaction relationship between the robot and its environment through a single point of contact instead of working to regulate position or contact force. This relationship, otherwise known as the impedance of the system, is typically represented by a transfer function of the system. This transfer function can be either the ratio of Cartesian displacement to input force or the ratio of Cartesian velocity to input force for the given system. Robot controllers that fit into this category are called “impedance controllers.” One type of impedance controller, called the position based impedance controller, measures the interaction force at the end effector of the robot and adjusts its Cartesian trajectory input to increase or decrease the force exerted on the environment by the robot [25]. Instantaneous model impedance control is another control strategy that actively alters the robot’s motion to control the impedance characteristics of the system [26]. The force-impedance controller acts like a modified force controller to allow the robot to act as both a force limited manipulator and a position limited manipulator by changing the values of the robot’s incoming position trajectory based on end effector force measurements. This force controlled system is beneficial because it allows the desired impedance behavior to be obtained without any knowledge of the environment [27]. Another force tracking impedance controller has been proposed to control the robot’s trajectory to maintain a specified relationship between the force,

velocity, and acceleration error of the entire system. This technique actively compensates for uncertainties in the robot's dynamics model using time-delayed information [28]. All of these systems act as impedance controllers by definition, though they are not what is typically intended by the term impedance control.

The most widely used method of compliant control, or what is typically meant by the term impedance control, was developed by Hogan in 1985. This method of impedance control actively enforces a desired stiffness and damping relationship between the robot and its environment [29]. This form of impedance control considers several factors to specify how a robot will react when an external force is applied to it. An approximation of this impedance controller would be a state space controller with a three element state vector containing position, velocity, and desired output force, where the controller is capable of maintaining a relationship between all the variables instead of reacting to a single input. This multiple input property has many advantages when a robot must interact with external forces applied by its environment. Because the impedance controller maintains a stable and constant impedance relationship when a robot's end effector comes into contact with an object, it is capable of performing both the gross and fine motion portions of assembly [29]. Additionally, impedance control does not require the inverse kinematics of the manipulator to be known to control the robot using Cartesian position inputs, which is helpful when using redundant robots for which the unique and direct inverse kinematics needed for real-time control may not exist.

Implementing an impedance control algorithm is straight forward. However, selecting the impedance relationships necessary to complete a specific task has

manifested its own body of research. Fasse claims that impedance control has primarily been reserved for research environments because it is difficult to specify the correct system impedance to accomplish a specific task in a manufacturing environment. He also mentions that it would be difficult to vary the stiffness variables in an organized manner to facilitate the different phases of assembly [30]. Research on this topic has produced many different solutions to these problems. Fasse himself proposed a compliant system called spatial impedance control. Spatial impedance control divides the compliance variables into spatial and non-spatial parameters. Then reference frames are attached to both the end effector of the robot and its desired goal position so that a potential energy function can be defined. This function is minimized when the two frames are aligned, and the minimization process is a function of the compliance variables of the controller during each step of assembly. While spatial impedance control simplifies some aspects of the compliance selection process by creating a visual representation, the complex algorithms needed to implement the system are not desirable when programming a real-time control system [30, 31].

Another design process has been proposed to produce a stable impedance controller for heavy and stiff industrial robots. This design approach is said to be all inclusive, as it takes all aspects of the controller design into consideration. The resulting system is an accurate impedance controller that can maintain stable impedance characteristics during all stages of an assembly process while allowing the industrial robots to work with very low stiffnesses [32]. However, the drawback of this complete design method is that it requires very detailed knowledge of the system, as even small uncertainties can cause stability problems for the intended industrial robots. To address

this problem, machine learning has been implemented in many systems to allow the robot to compensate for small modeling errors. For example, one system consists of a model-free machine learning algorithm that learns the proper values needed by a variable impedance control algorithm based on path integrals and optimal control principles. Using a reference trajectory, this system learns a gain schedule to increase the gains from a base low gain system when needed to extract the desired system performance [33].

Kelly et al. created an adaptive impedance controller to address these same problems without using machine learning methods. They instead use an adaptive impedance controller to overcome problems that arise from unmodeled dynamics in a robot system. This is useful because the dynamic behavior of rigid manipulators is complex and non-linear, which makes it difficult to design a high-performance model-based control strategy. When a robot is acting in a constrained environment, these unmodeled dynamics can cause unpredictable behavior. This adaptive impedance scheme uses joint position and velocity sensors in addition to an end effector force sensor to follow a constrained trajectory. This type of controller is capable of maintaining a constant relation between motion error and the force being applied by the robot's end effector using only an initial estimate of the robot's dynamic parameters because the controller creates an adaptive integration gain matrix from sensor feedback [34, 35]. Controllers of this kind have been introduced to find a solution to the accuracy/robustness dilemma that occurs from the trade-off between output impedance accuracy and the overall robustness of the impedance controller to modeling errors. Other closed loop hybrid impedance control systems that improve the robot's dynamics model can be found in [25, 36]. While these types of model-improvement impedance control schemes

increase robot control accuracy, which is a large benefit, they do little to help the robot interact with its environment or successfully complete a task.

Aside from the dynamic model correction type of impedance control, other adaptive impedance control systems have been developed to actively change impedance parameters to meet or maintain specific goals of the robotic system. One research group created a dual loop controller to produce their desired robot behavior. The inner loop of the controller was created using model reference adaptive control (MRAC), which basically linearizes the robot's dynamics to compensate for them while following a trajectory in free space. This is used as a direct model of the system for the outer loop of the controller which produces a "virtual model" of the system. This virtual model can be strategically modified to achieve desired system behavior. This system allows the robot to be set to perform normally when needed, and if an obstacle is encountered, it is capable of responding with predefined mechanical impedance [37]. However their adaptability is focused on the performance of the robot as opposed to the success of the application.

There have been a few other adaptable impedance control systems presented in literature to allow a robot to exhibit unique behavior, or operate with a different form of sensory feedback. One example was created to independently control the impedance of a robot over multiple points of contact when the robot touches its environment in more than one place. This controller was called the multi-priority Cartesian impedance controller and it would be useful to control a robotic hand as it grasps an object. In this application, the hand would have a separate desired impedance set for each point at which its fingers independently touch the object, allowing the designer to control how hard the hand can

squeeze the object without using force sensors or strain gauges [38]. Another type of impedance control uses feedback from a vision system to maintain the desired contact force relationships between the manipulator and any object [39]. The controller is known as virtual impedance control, and it works like regular impedance control. However it does not require any physical contact to provide the reaction forces of an external system. The controller instead works by drawing an imaginary boundary around objects of interest. If the vision system detects that the robot has crossed the imaginary boundary, then it begins to push back on the robot with a fixed impedance. This method has many applications, but it requires a high speed vision system with very good resolution to produce an effective system. Aside from the above examples, there are also specialized impedance control systems that actively vary control law parameters to exhibit better performance under tracking and stability [40], overcome harmful vibrations or dynamics [41], or minimize impedance force error [42]. While each of these controllers has its own benefits, all of them focus on obtaining desired behavior from the robot. However, they lack consideration of the behavior of the environment the robot is intended to interact with. This is a key requirement if the system will be performing a highly coupled task, such as cooperative assembly using two impedance controlled robots.

2.3 System Design for Peg and Hole Assembly

To integrate an impedance controller into a complete system that includes the dynamics of the peg, the hole, and the two manipulators, all aspects of the system must be taken into consideration. For this reason, there has also been a great deal of specialized research on the contact forces generated during peg and hole assembly. One example of

this research is the use of Lagrange's impact model to derive a general impact equation to estimate the forces generated by an industrial manipulator performing peg and hole assembly [43]. Another method uses an impulse model to minimize the impact during a collision between a manipulator and its environment [44]. Other impact models have been developed to represent the collision of a robot with a free floating object, such as a satellite in outer space [45]. Accurate modeling of the impact forces generated during robot interaction can also give an estimate of the dynamics and frequencies encountered during the transition from a free-space to constrained environment. This type of data has been used to design a controller that minimizes and reacts to the forces generated during impact [46]. Another area of related research focuses on the dynamic properties of the friction forces that impede assembly [47]. These are all examples of ways in which the entire system was modeled during the design and integration of the impedance controller. However, system modeling can be utilized further to design more aspects of the control system.

Once a controller has been designed, it is sometimes also necessary to design new techniques or motion strategies to perform the assembly task. For example, one algorithm generates different compliant assembly strategies for the beginning, middle, and end of an assembly process based on 28 possible geometric constraint conditions defined by a model of the assembly task [48]. This algorithm is essentially capable of providing a unique hybrid force-position controller for any possible contact geometry encountered during a task. Based on 17 predefined relative part geometries, a formal mating model is built to decide which compliance strategy and force constraints are to be used. Another algorithm creates a compliance and damping matrix that is programmed into a robotic

system offline to eliminate the possibility of error buildup within the system [49]. Using friction cones and Hooke's law to model the elastic behavior of the system, they can ensure that any contact forces between the peg and hole will provide error-corrective behavior and guide the system towards success by absorbing errors. Similar studies have also been implemented using analysis by D'Alembert's principle to model the energy interaction of the system [50].

The most extensive system models have been created for the three dimensional contact forces that result from the simultaneous insertion of multiple pegs into corresponding holes. Several models have been produced for dual peg and hole insertion tasks [51, 52]. This work models all possible contact states between two coupled pegs and their corresponding two holes and attempts to define a control strategy that accomodates all of them. Another research group outlined a multiple peg and hole insertion task with three pegs arranged in an equilateral triangle shape [53]. They chose to reduce the problem to three degrees of freedom and approach the potential contact states in much the same way as other systems.

Further study of the peg and hole system makes it possible to devise a general trajectory or motion plan to increase the likelihood of successful assembly by taking advantage of certain aspects of the system. For example, one approach is to model the compliant system using a technique called back propagation [54]. This method transforms the peg and hole into a simplified model of a point being moved into a hole that is narrower than the width of the peg. The trajectory of this point is created backwards from the point's goal position back to the robot's current position to plan the motion of the peg into the hole. Another similar approach is the back projection of the

peg's allowable range [55]. Similar to the previous case, the algorithm begins with a peg almost completely in the hole, and within the bounds of an allowable angular range defined by the system's geometry. Then a trajectory is mapped from this point to the peg's starting point. Other algorithms instead choose to plan the ideal impedance parameters and trajectories for a given task to maximize a performance index [29], or to maintain favorable single-point contact states that reduce the positional error of the system [56]. These are all examples of how system modeling has been used to design all aspects of a peg and hole assembly system. However, they all seem to lack quantitative and measureable goals that are usually associated with an engineered system. For example, a performance index may be applicable to a task, but it is not simultaneously focused on the needs of the robot's controller. Also, there is no way to specify the "best" trajectory from back propagation with respect to any goal, as any successful trajectory is deemed as good as another. This is why these approaches lack the design aspects needed to produce a truly engineered and optimized impedance control system.

No matter what type of impedance controller has been designed, there are still other design parameters to be considered, such as the desired hardware configuration. Peg and hole assembly has been performed by many different configurations of robotic systems. Each of these systems must also be integrated into the design of the total system. One approach is to use two manipulators to perform peg and hole assembly without the use of fixtures [57]. The positive argument is that the system will be more easily adaptable to different tasks since there is no physical hardware specialized for any specific task. However, this particular system suffered from a complex force control algorithm that tried to characterize force conditions and move both arms to minimize the

resultant forces. This type of controller, contrary to the goal of the system, would be heavily specialized for each specific task. Other force controlled systems for assembly utilized simpler systems, such as a three DOF planar robot [58], with greater success. Other purely mechanical systems resorted to random vibrations to help clear jams and complete contact assembly tasks [59]. While demonstrated to be successful, there are definitely reliability concerns that would rule out this type of system as an option for any large scale manufacturing system. For each of these systems, the goal was to produce a universal peg and hole assembly system that could mate various parts without making any changes to the system. However, each of them resorted to specializing some piece of their hardware or software to accommodate the experimental task. Since this need to adapt automated systems to accomplish specific tasks is almost inevitable, it would instead be more realistic to design a system whose hardware and controllers remain constant between different tasks with the exception of a few software parameters that could be easily defined and changed.

2.4 State of the Art Contribution

The peg and hole assembly system developed by this thesis aims to eliminate the peg and hole assembly and impedance controller design shortcomings mentioned above. The experimental system used in this thesis was composed of two redundant robotic arms that cooperatively perform assembly tasks using a new approach to adaptive impedance control. By creating an impedance controller with inputs to change the six DOF stiffness parameters and compliance center locations of the peg and hole attached to each robot, the system electronically exhibits the compliant behavior of a mechanical RCC without

any of its limitations. This allows the system models previously derived for mechanical RCCs to be directly applied to the new system during the design phase. Additionally, the robot controllers are completely self contained and do not rely on external force sensors or mechanical devices, which are proven to increase the response time and decrease the stability of the system. In conjunction with the robot impedance controllers, additional system-level vision and variable compliance controllers were simultaneously run to increase the positional accuracy of the system as well as assign the optimum impedance controller stiffness parameters with respect to quantitative goals for coupled system stability and wedging and jamming avoidance. Finally, the straight forward controller parameter design algorithm developed in this thesis allows the system's impedance parameters to be designed with respect to the performance and success of the entire system based only on the geometry of the peg and hole to be assembled. The design and control processes used to obtain all of these benefits are unlike any other in published literature, so they constitute the contribution of this thesis to the state-of-the-art of peg and hole assembly.

CHAPTER 3

HARDWARE OVERVIEW

The system developed in this thesis is composed of equipment that was already present in the robotics research lab in UNM's South Campus MTTC building. Specifically, the system is composed of two Barrett Technology Whole Arm Manipulators (WAMs), a vision system, reflective memory, and a control computer as shown in figure 3-1 below.

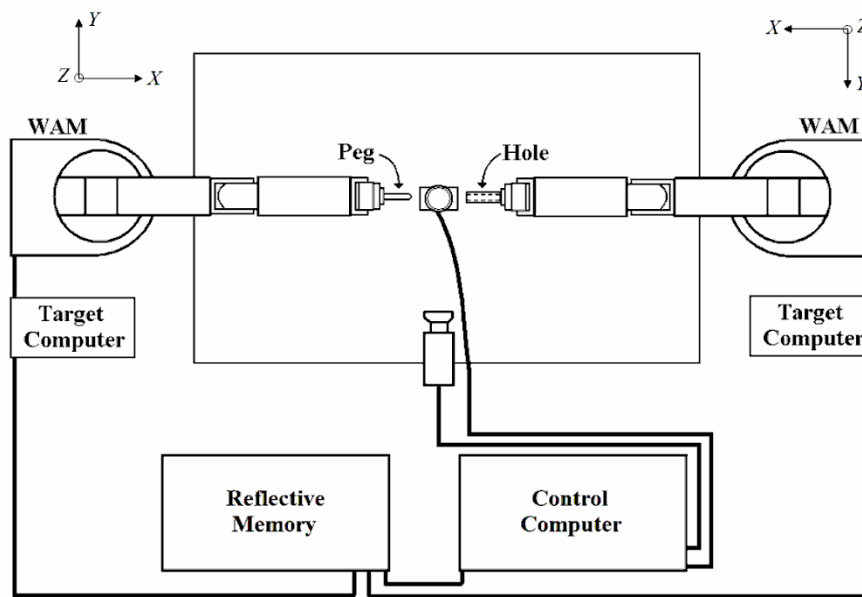


Figure 3-1. Relevant hardware organization in the MTTC robotics research lab. Also shown are the individual coordinate systems attached to each WAM.

Each WAM is a light-weight, seven DOF redundant robot arm. Though they are mounted on a one dimensional track which adds an eighth DOF to each arm, they will remain stationary for the experiments in this thesis. Each WAM communicates with an

individual *Linux* based target computer that runs compiled *Simulink* control programs. In this thesis, a specialized variable impedance controller was programmed in *Simulink*, compiled, and loaded onto each robot's target computer. This controller is explained in detail in Chapter 6. In addition to communicating with each WAM, the target computers are also able to read from and write to specific memory addresses, called nodes, in the reflective memory system. This is where the WAMs write joint position and joint torque data to the control computer, and read Cartesian commands and compliance parameters from the control computer. The control computer hardware is typified by its 2.53 GHz Intel Core2 Quad processor and four gigabytes of memory. This computer simultaneously sends trajectory commands to each WAM, runs the trajectory compensation controller, and runs the variable compliance controller explained in Chapter 6. These controllers are programmed as *Simulink* models that run compiled user-defined functions. These functions communicate with the reflective memory and control the robots whenever a model "simulation" is run. This computer is responsible for receiving image data from two BASLER A602-fc cameras through FireWire connections and computing all commands to perform the peg and hole assembly.

It is also worth noting that the Cartesian position commands sent to the WAMs are represented by homogeneous four-by-four transformation matrices. However, the trajectory and compensation vectors computed by the control computer are in quaternion representation due to its beneficial continuous representation of three dimensional rotations. Planning robot motion trajectories in quaternion representation reduces the possibility of singularities and allows cubic trajectories to be easily computed for the robots. This is beneficial in robotics as cubic trajectories provide smoother acceleration

and velocity behavior. Thus, each *Simulink* controller must also contain functions to convert between the two Cartesian position representations.

To communicate with the robots through the reflective memory, a new *Simulink* block had to be written in the C programming language and compiled into a user defined function. This block uses a flag input to change Pose its function. Its list of possible functions include opening and closing the memory interface, as well as writing and reading to and from different memory addresses allocated for each WAM. For example, the *Simulink* model shown in figure 3-2 is used by the control computer to read the current joint position, which is converted to a quaternion position of the end effector through forward kinematics, and joint torques from both WAMs in real-time. This particular model also keeps a running standard deviation of the individual joint torques to recognize if either WAM has collided with an immovable object.

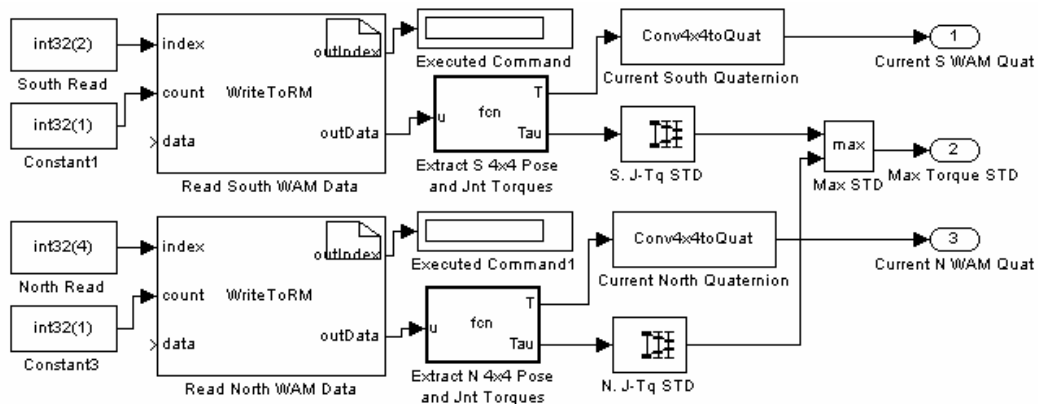


Figure 3-2. *Simulink* model that reads current joint positions and torques from each WAM in real-time. Notice the running standard deviation block attached to the joint torque output to monitor the system for contact with an immovable object.

In another implementation, the *Simulink* model in figure 3-3 shows the block configuration that intakes a quaternion Cartesian position command and stiffness parameters for each WAM and writes them to the reflective memory so that each target computer can execute the desired motion.

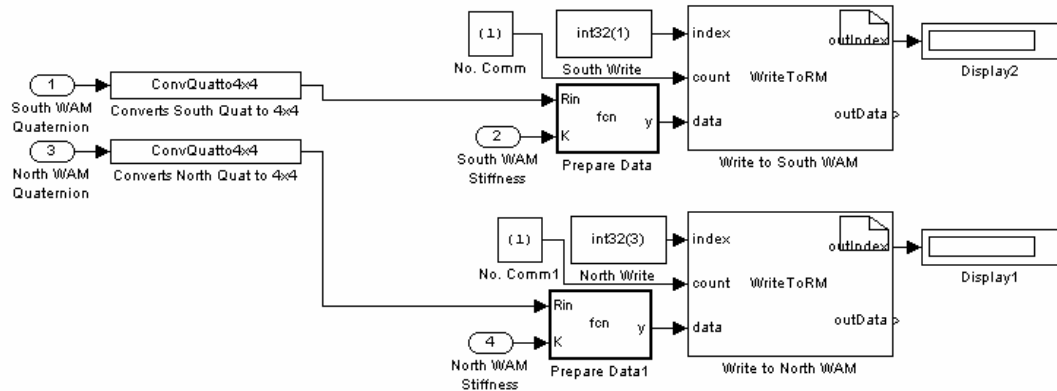


Figure 3-3. *Simulink* model that converts quaternion trajectory points computed by the control computer to homogeneous four-by-four transformation matrices and writes them to the reflective memory with stiffness parameters to command each WAM.

Last, the peg and hole end effectors used for the experiments are made from machined aluminum and are rigidly attached to the wrist of their respective WAM. The “peg” has also been fitted with a JR3 force and torque sensor. This sensor is not part of any controllers, but it is used to experimentally verify the performance of the system components in Chapters 4 and 8. The JR3 is connected to a data acquisition computer that records six DOF force and torque measurements every 0.01 seconds. This concludes the basic description of the hardware and interface that were used to create the overall system in this thesis. The detailed description and design process for each controller is presented in the following chapters.

CHAPTER 4

IMPEDANCE CONTROLLER

As described in Chapter 2, there are many different control strategy options for controlling a robot while it is in contact with its environment. The method used to control the WAM robots in this thesis is called impedance control. Impedance control allows a robot to interact with its environment by controlling the relationship between the impedance of the robot and the admittance of its environment through the interaction port located at the point of contact between them. To control this relationship in an organized way, the impedance controller simultaneously manages a relationship between the position and velocity of the robot's end effector and the forces applied to it by the environment. In addition to enabling the robots to reject disturbances in a predictable way, impedance control also provides a means to control redundant robots, or those with more than six DOF, by eliminating the need to calculate the inverse kinematics of the robot. In this system, the impedance controller is implemented through a compiled *Simulink* model. This model is shown in figure 4-1.

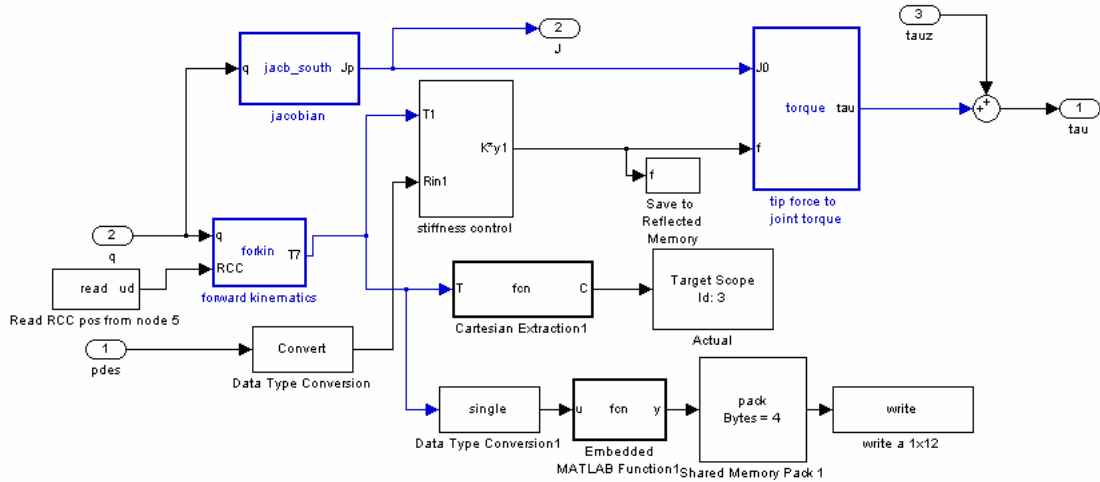


Figure 4-1. *Simulink* model that represents the basic impedance control functions for each WAM. The inputs to the system are the current joint positions and the desired Cartesian position and rotation of the end effector. The output is a vector of joint torques needed to move the WAM from its current position to the desired position. The parameters that control the compliant behavior of the system are read from reflective memory along with the desired position and implemented in the stiffness control block.

This model intakes the current joint positions of the WAM and the desired Cartesian position and rotation of the WAM’s end effector. The output from the impedance control model is a vector of joint torques that is sent to the WAM’s motor drive hardware to achieve the desired position while maintaining the desired stiffness and damping behavior of the robot. In addition to these impedance controller tasks, this model also writes the current joint positions, stiffness gains, and joint torques of each WAM to the reflective memory in real-time. It should be noted that the Cartesian goal position prescribed to each WAM is relative to its individual global coordinate system. There is no simple global coordinate system for the two robots, so their trajectories are controlled independently.

4.1 Impedance Controller Functionality

This section presents the theory and implementation of the impedance controller models used to control the WAMs. When designing an impedance controller, the first step is to define a relationship between the force output by the controller and the resulting displacement of the end effector in Cartesian coordinates. This requires the target robot to have a special set of hardware characteristics. More specifically, the target robot must have joints that are controlled by command torques, T , encoders that are capable of reading joint positions, θ , and the forward kinematics, L , of the robot must be known to relate the robot's joint positions to the corresponding Cartesian end effector position, X , by the function $X = L(\theta)$. Assuming the target robot possesses these characteristics, the resulting impedance controller will be able to follow a desired cartesian trajectory with reasonable performance as well as interact with external forces from environmental contact in a controlled and predictable way. An important benefit of these impedance control characteristics for peg and hole assembly is the ability to easily transition between gross and fine motion since there is only one control strategy needed to accomplish both types of movement.

The quality of the system's trajectory following performance is measured by Cartesian accuracy and is controlled by the effective stiffness of the controller. The effective stiffness is a controller gain that defines the desired relationship between Cartesian accuracy and control force applied to the end effector of the robot. If the effective stiffness is represented by K , the force applied to the end effector to move the robot or react to the environment is given by equation (4.1).

$$F = K[X_0 - X] \quad (4.1)$$

Where X_0 is the initial position of the end effector and X is the desired position.

Notice that this relationship is simply an adaptation of the equation for a linear spring, $F = Kx$. This implies that the output robot behavior can be modeled as an end effector that is supported by a combination of six linear springs. Six springs are needed because the effective stiffness, K , is actually a six-by-one vector that represents the stiffness of the robot over all Cartesian six DOF. Next the Jacobian matrix, $J(\theta)$, must be computed. The Jacobian matrix is a constant matrix that relates a robot's joint velocities to the Cartesian velocity of its end effector using the relation $dX = J(\theta)d\theta$. From the virtual work principle, the joint torques necessary to create the desired force or displacement change can be found using the Jacobian matrix's transpose in the equation $T = J'(\theta)F$. Combining all of these equations into a single controller relation results in equation (4.2). This equation relates joint torque to the desired stiffness behavior and trajectory following performance of the robot and controller.

$$T = J'(\theta)K[X_0 - L(\theta)] \quad (4.2)$$

Similarly, a relationship between the force applied to the end effector of the WAM and its velocity can be defined. If the damping behavior of the robot can be represented by a coefficient, B , changing this value would modify how the robot would

respond to velocity errors during its movement. The relation between force and acceleration can be defined as equation (4.3).

$$F = B[V_0 - V] \quad (4.3)$$

Where V_0 is the initial velocity of the end effector and V is the desired velocity.

The definition of the Jacobian matrix can be rewritten to show that $V = J(\theta)\omega$. Using the same principle of virtual work as above, the actuator force can be related to a desired change in velocity with equation (4.4).

$$T = J'(\theta)B[V_0 - J(\theta)\omega] \quad (4.4)$$

To complete the controller, a gravity compensation loop must be included to keep the robot from falling under its own weight. A null space controller must also be included to keep the robot from naturally favoring low friction joints during movement. This condition would result in awkward reaching geometry that would approach the joint limits of certain joints of the WAM after repeated movements. The impedance controller must also account for the inertial effects of the robot. All of these extra features require additional terms to be considered by the controller. To simplify this task, the robot is assumed to follow the constraints of rigid body motion. This allows the controller to use predefined mass and moment information about the links of the robot to compute the mass, M , and inertia, $I(\theta)$ matrices for the controller. The mass and inertia information

for this system is measured from CAD models of the WAM robots provided by their manufacturer. While there is likely some modeling error in these models, the resulting matrices have proved to be accurate enough to allow the impedance controller to perform reasonably well. Combining the position, velocity, inertial, and gravitational effects into a single control equation yields a single equation to define the torque needed by each joint of a robot to achieve a desired position and velocity from a current state. This final result is shown as equation (4.5).

$$\begin{aligned}
T = & I(\theta)J^{-1}(\theta)M^{-1}K[X_0 - L(\theta)] + S(\theta) + I(\theta)J^{-1}(\theta)M^{-1}B[V_0 - J(\theta)\omega] \\
& + V(\omega) + I(\theta)J^{-1}(\theta)M^{-1}F - J'(\theta)F - I(\theta)J^{-1}(\theta)G(\theta, \omega) + C(\theta, \omega)
\end{aligned} \tag{4.5}$$

Where $S(\theta)$ is the position dependent torques, $V(\omega)$ is the velocity dependent torques, $G(\theta, \omega)$ is the accelerative coupling terms, and $C(\theta, \omega)$ is the inertial coupling terms [29].

All terms in equation (4.5) are constant physical or measured values. The two gains explained above, K and B , are the two gains that will be changed to obtain the desired performance and behavior from the robot during peg and hole assembly. For this reason, these two parameters are connected to specific nodes of the reflective memory system. This allows the control computer to actively vary these parameters as needed to change the behavior of the system.

One more parameter from the impedance controller is also connected to the system control computer through the reflective memory. During peg and hole insertion, the point on the peg at which it is allowed to translate and rotate is called the compliance center and it can play a key role in the behavior of the system during assembly. This

position is fixed for most systems, but the implementation of variable impedance control allows this point to be actively varied during insertion. This point is represented by a single parameter in the impedance controller and it defines the distance of the desired compliance center from the tip of the peg. This distance, L , can be varied by the control computer through the reflective memory and is shown in figure 4-2 below.

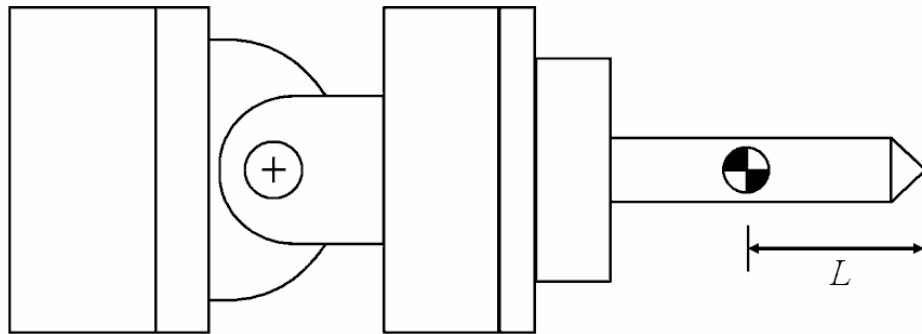


Figure 4-2. The distance L is the distance from the tip of the peg to the desired compliance center. This is the point on the peg at which it is allowed to independently rotate and translate in response to applied forces.

Modifying this length changes where the forward kinematics calculates the tip of the robot's end effector to be. Since the impedance controller tries to maintain the position of the tip of the end effector in the presence of disturbances, this point is effectively where the peg is allowed to rotate. An example of how this parameter changes the behavior of the peg is shown in figure 4-3. In this figure, it is assumed that contact forces between the peg and the hole have generated a torque that is applied to the peg due to misalignment. Figure 4-3 demonstrates two types of behavior that could result from this torque depending on the compliance center location.

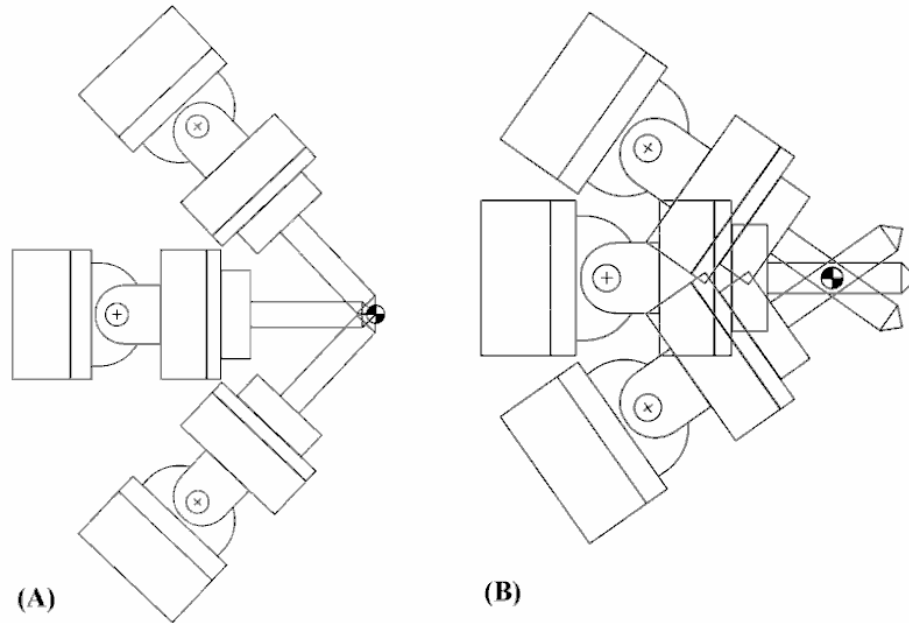


Figure 4-3. This figure demonstrates the behavior associated with different compliance center locations. (A) is generally considered to be the most beneficial for peg and hole assembly since it offers the most direct control over lateral and rotational positioning. (B) shows the typical location of the compliance center for a robot holding a peg in a mechanical fixture without a RCC.

With this last piece of the impedance controller added to the *Simulink* model, everything needed to control the behavior of the peg during assembly to guarantee success is available to the control computer. The overall *Simulink* model that implements all aspects of the impedance control, gravity compensation, and null-space control is shown in figure 4-4. This model is compiled and sent to the WAM target computers where it is run at 500Hz.

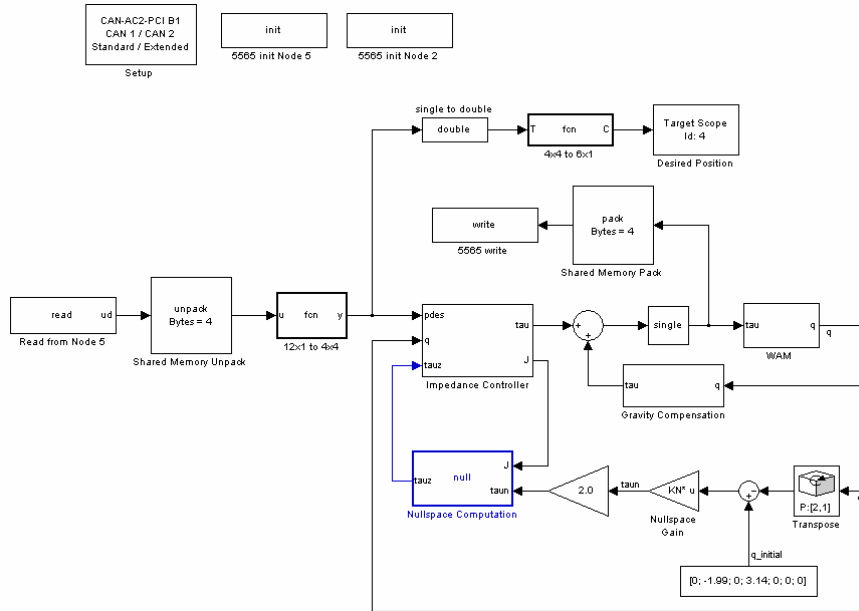


Figure 4-4. This is the complete *Simulink* model that performs all functions of the impedance controller control law, including gravity compensation and nullspace control. This is the model that is compiled and sent to the target computer for each WAM. Notice the read and write blocks that interface with the reflective memory.

4.2 Impedance Controller Performance

Once the controller is completed and functioning, it is important to understand the performance of the system to gain insight into the effects of changing different controller parameters. Through experimentation, it has been found that varying the damping gain of the controller generally produces wild and unpredictable results. Thus, the design strategy will be to instead choose a single damping value and assign it to the controller offline and let it remain constant throughout assembly. The stiffness gains, on the other hand, produce very predictable changes in behavior as they are varied. For example, decreasing the stiffness gains will produce accurate and linearly decreasing control force output for a given Cartesian position error. However, lowering the stiffness of the impedance controller is analogous to hanging a mass from a weaker spring, which will cause the end

effector of the robot to “droop” more under its own weight. This makes the system work harder to follow a Cartesian trajectory. To demonstrate the relationship between controller stiffness and the total performance of the system, a desired Cartesian trajectory was sent to the impedance controller. The WAM was then programmed to follow the trajectory with different stiffness gains. As the WAM completed each trajectory, it wrote out a data structure that contained its actual Cartesian trajectory. This data was used to compare the trajectory following performance of the impedance controller for different stiffness levels. Figure 4-5 shows this information graphically.

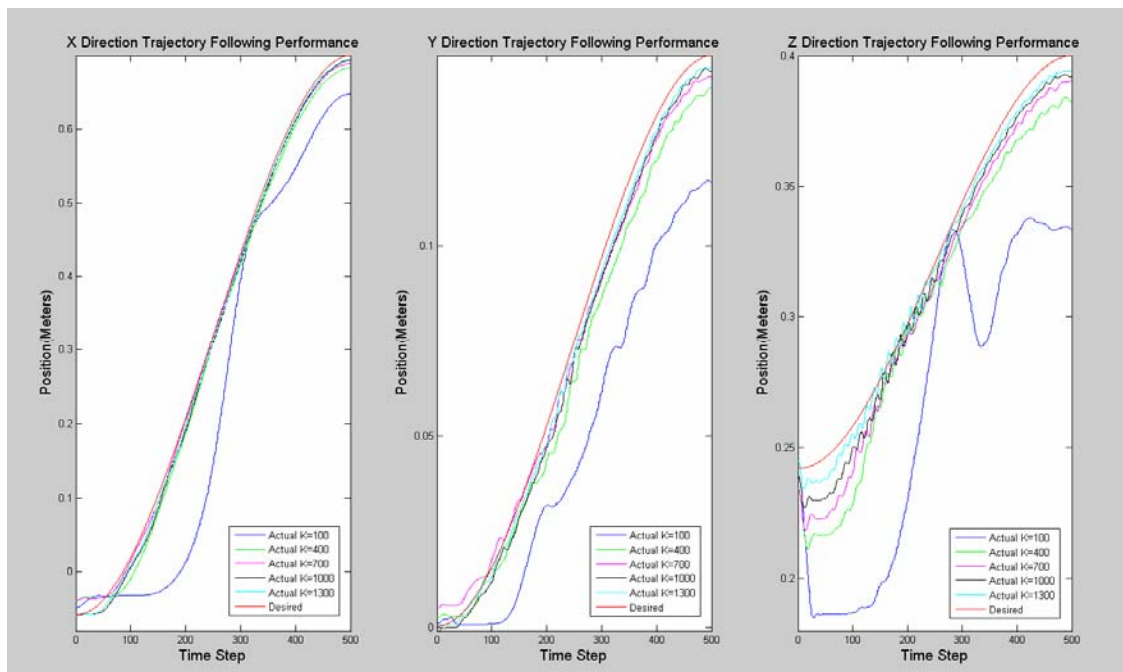


Figure 4-5. Comparison of the three-dimensional trajectory following performance of an impedance controlled WAM for different stiffness gains. The plots are categorized by error in each direction. Notice the additional error present in the Z direction as a result of the effects of gravity.

From this figure, it can be seen that the controller and WAM behave as one would expect. It can also be seen that while the minimum lateral stiffness gain of the impedance controller is theoretically zero, it should never be allowed to fall below 100 because the trajectory following performance of the WAM degrades significantly at lower stiffness levels. It can also be seen that there is little difference in performance for stiffness gains above 400. While increasing the lateral stiffness gains beyond 400 would increase the performance of the system, the visual feedback controller discussed in Chapter 6 can compensate for any relatively small errors. This enables the impedance controller to use any stiffness gain of 400 and higher and achieve very good tracking results. This is also evident in table 4-1, which shows the average trajectory following percent error for each stiffness gain in each direction.

Stiffness Gain (K)	Percent Error in Each Direction (%)		
	X	Y	Z
100	14.47	29.44	16.47
400	2.97	9.09	4.68
700	1.40	4.63	3.22
1000	1.61	4.43	2.14
1300	1.25	3.20	1.11

Table 4-1. Trajectory following percent error for each stiffness gain in each principal direction. Notice that acceptable performance is achieved with stiffness gains of 400 and higher, and there is essentially no appreciable performance increase for gains above 700.

In section 4.1, it was mentioned that the behavior of the impedance controller could be approximated by a mass that is supported by a combination of six linear springs. This is an important assumption that justifies the two-dimensional approach to the physical system modeling performed in Chapter 5. To verify that the behavior of the

system can be approximated this way, the WAM holding the peg was commanded to move to a specific Cartesian position. Then a set of specific stiffness gains were sent to the impedance controller to define the six DOF stiffness of the end effector. The tip of the end effector was then displaced in the pure Z direction exactly ten centimeters at a constant velocity. As mentioned in Chapter 3, the peg end effector is equipped with a JR3 force and torque sensor. This sensor was used to measure the actual force applied to the end effector by the impedance controller to impede the increasing positional error during this displacement. Then a plot of output force versus displacement was created to show that there is a linear relationship between the two values. The slope of this line is equal to the equivalent physical stiffness that a real spring would have to possess to impose the same behavior on the peg. It should be mentioned that the JR3 sensor is substantially stiffer than the impedance controlled WAM robot. So the small compliance due to the slight deflection needed for force measurement can be neglected in the results from these experiments. So we can assume that the measured system stiffness is entirely due to the output of the impedance controller. This process was completed for lateral stiffness values between 100 and 1000. An example of the results from this test for the case when the lateral stiffness gain is set to 500 is shown in figure 4-6.

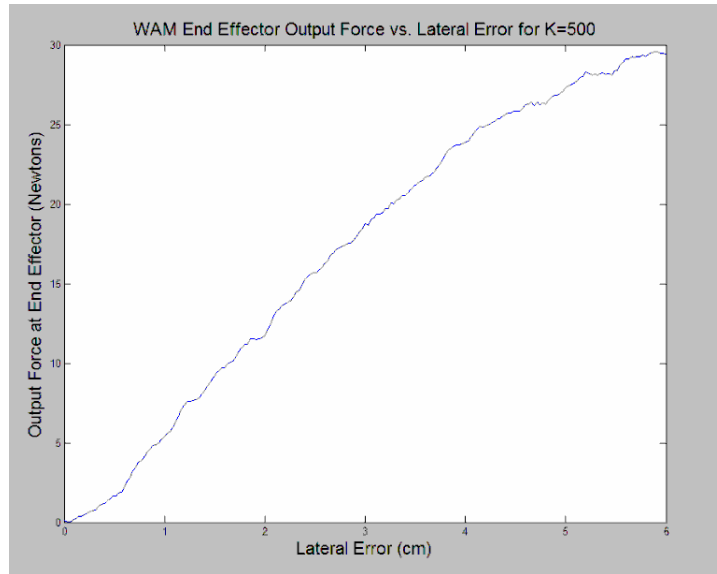


Figure 4-6. With the impedance controller’s lateral stiffness gains set to 500 in all directions, the tip of the peg was displaced from its desired position in the pure axial direction while the JR3 measured the control force applied by the peg to resist the increasing positional error. Notice the linear force and lateral displacement error relationship that is analogous to the spring constant of a real linear spring.

The behavior is clearly linear, so the linear spring approximation should be accurate for system modeling purposes. The stiffness gain vector also controls the rotational stiffness of the end effector relative to orientation errors about the X , Y , and Z axes. It would also be beneficial to show that this rotational stiffness behavior can be approximated by a linear rotational spring. To verify this assumption, a similar test was performed. The difference being that the displacement changed from a linear distance of ten centimeters, to a pure rotation of 30 degrees about the Y axis. The resulting torque applied to the end effector of the robot by the impedance controller as a function of rotational displacement error is shown in figure 4-7.

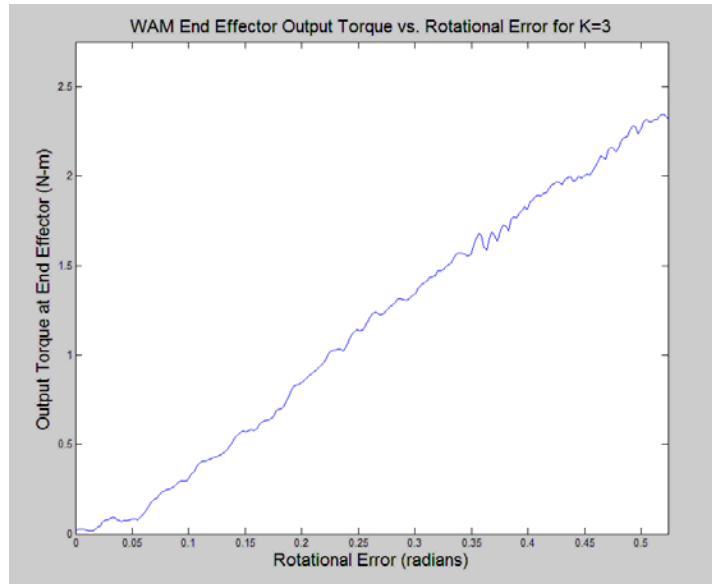


Figure 4-7. Similar to the previous test, the peg was displaced rotationally from its initial horizontal orientation and the torque applied by the robot to resist the increasing rotational error was measured. The rotational error and output torque relationship is also linear.

This relationship has also proved to be linear, so the approximation of the peg's rotational stiffness as a linear spring is also valid. It is also important to note that the stiffness gains of the impedance controller are not measured in values that correspond to a physical meaning, such as pounds per inch. They are instead dimensionless gain values. As mentioned above, force versus displacement testing was performed for many different gains. This allowed the relationship between controller gain values and the corresponding actual physical spring force output to be mapped using a table. The relationship was found by simply by dividing the peak force measured by the sensor by the peak displacement error. This is a valid method due to the linear relationship between force and displacement error. It is necessary to know this relationship for the system modeling in Chapter 5 since the behavior of the peg and hole interaction is governed by actual

spring forces, and not the stiffness gains applied to the controller to achieve them. The stiffness gains tested along with their corresponding equivalent physical stiffness values are shown in table 4-2.

Lateral Stiffness Gain (K_x)	Physical Stiffness Equivalent ($N/meter$)
100	188.6
200	247.8
300	350.1
400	411.9
500	559.1
600	638.3
700	706.3
1000	859.4

Table 4-2. Table of impedance controller lateral stiffness gain values along with their equivalent physical stiffness values.

If these values are plotted together, the result is shown in figure 4-8. This figure gives a visual representation of the relationship between increasing controller gains and the resulting increase in physical stiffness output by the WAM.

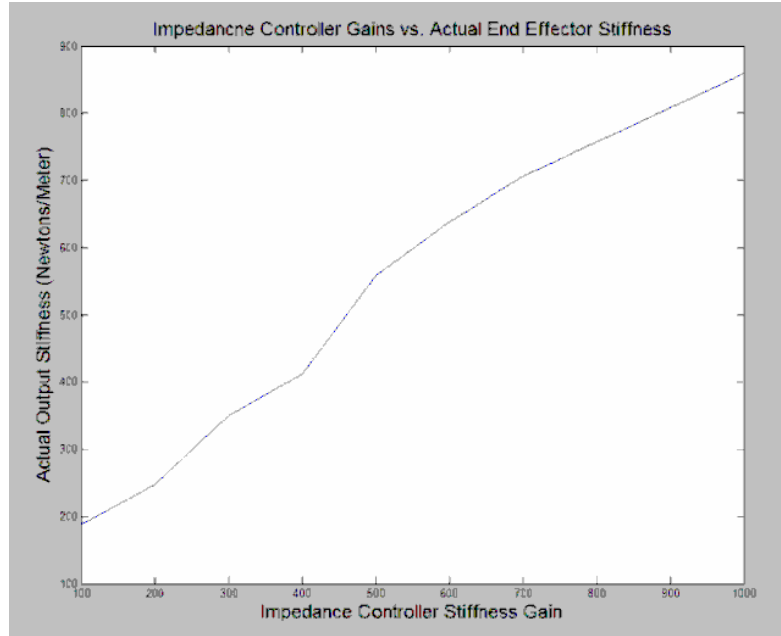


Figure 4-8. This plot demonstrates the linear and direct relationship between the impedance controller stiffness gain and the physical stiffness output by the system.

Figure 4-8 shows that there is an approximate linear relationship between the impedance control gains and the output physical stiffness of the system. This is beneficial to the variable compliance system because it implies that changes in stiffness gains will result in predictable changes in peg and hole behavior. For example, if the system prescribes a small change in stiffness gains, it can be expected that the system will receive a corresponding small change in physical stiffness as well. Similarly, the same study can be performed for the rotational stiffness gains of the impedance controller. The relation between rotational gains and output rotational stiffness are shown in table 4-3 and figure 4-9.

Rotational Stiffness Gain (K_{θ})	Physical Stiffness Equivalent ($N-m/rad$)
1	2.75
2	3.79
3	5.06
4	6.12
5	7.80

Table 4-3. Table of impedance controller rotational stiffness gain values along with their equivalent physical stiffness values.

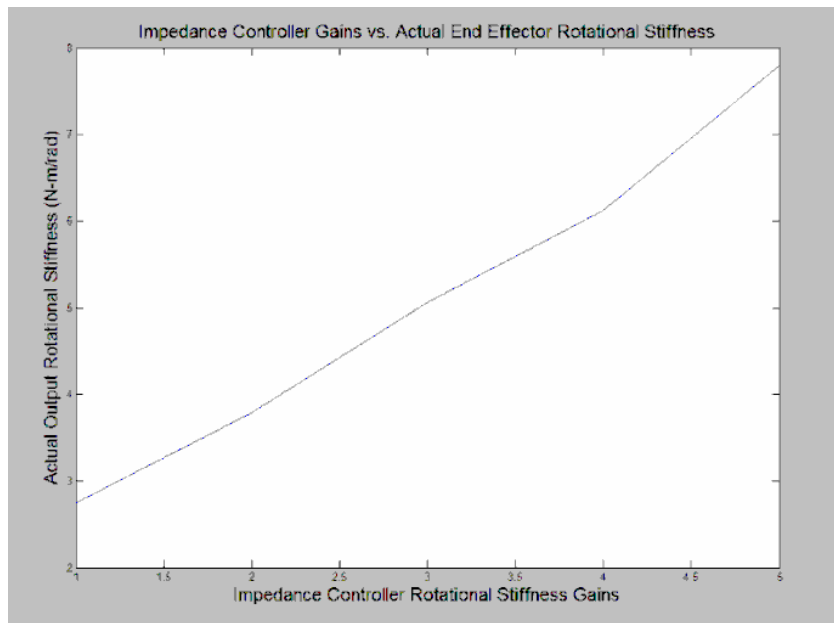


Figure 4-9. This plot demonstrates the linear and direct relationship between the impedance controller rotational stiffness gain and the physical stiffness output by the system.

There is also a linear relationship between increasing the impedance controller rotational stiffness gains and the resulting physical rotational stiffness output values. Now that it has been proven that the impedance controller performs adequately and its behavior can be modeled by the linear spring approximation, system modeling can be performed for the peg and hole assembly system in Chapter 5.

CHAPTER 5

SYSTEM MODELING

In this chapter, a set of governing equations is derived to model the behavior of the complete dual robot peg and hole insertion system. This is accomplished in two parts. First, a kinematic analysis of the peg and hole insertion problem is performed. Second, a coupled dual impedance controlled robot system stability analysis is performed. These equations are used to find both the optimum and the range of allowable impedance controller parameters in Chapter 7. Applying these parameters to the system controllers will guarantee that the completed system will perform the peg and hole assembly task successfully.

5.1 Peg and Hole Kinematic Analysis

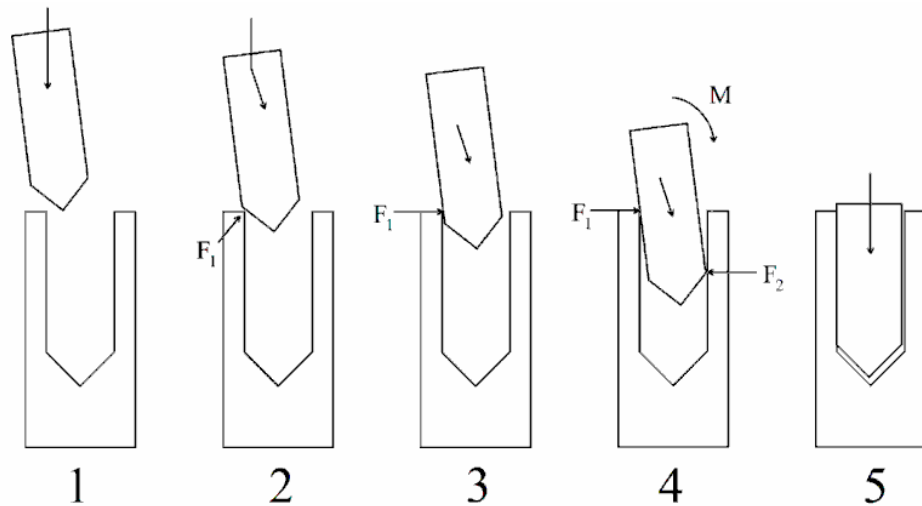


Figure 5-1. Stages of successful peg and hole assembly. 1 is the approach, 2 is chamfer crossing, 3 is one-point contact, 4 is two-point contact, and 5 is line contact and successful assembly.

Figure 5-1 shows a typical two-dimensional progression of a peg as it is inserted into a hole during assembly. The analysis and diagrams presented in this thesis are two-dimensional. Due to the axisymmetric properties of the experimental cylindrical peg and hole assembly task, the two-dimensional model accurately captures all of the kinematics of the three dimensional system. Phase one in figure 5-1 is the approach of the peg to the hole. This is the end of the gross motion phase of the robot's movement that aligns the peg and hole for insertion. This phase defines the initial lateral and rotational error between the peg and hole, which plays a large role in the success of the insertion process. Phase two is known as chamfer crossing. During this phase, the peg slides past the rim of the hole towards its center along the peg's chamfer to compensate for initial lateral positioning errors. The chamfer can be located on the peg, hole, or neither in the case of chamferless peg and hole insertion. During the chamferless case, the peg must be angled as it is inserted to mimic the behavior of the chamfer crossing phase. This process is shown in figure 5-2. Phase three from figure 5-1 represents the one-point contact condition, during which the peg slides past the rim of the hole with only a single point of contact that moves along the peg's body. Phase four represents the two-point contact phase, during which two points on the peg's body are in contact with the hole. The combined moment generated by the two opposing contact forces in this phase can correct the rotational error of the peg relative to the hole if the system's compliance is designed properly. This is the critical phase of the assembly process because this is where failure is most likely to occur as many combinations of forces can result in wedging and jamming instead of error correction. Finally, phase five represents the completed assembly. Intuitively, it is noticed that each phase can only occur over a certain range of insertion

depth. This is a result of the physical geometry of the system, and it is used to signal the transition from one phase to the next during modeling.

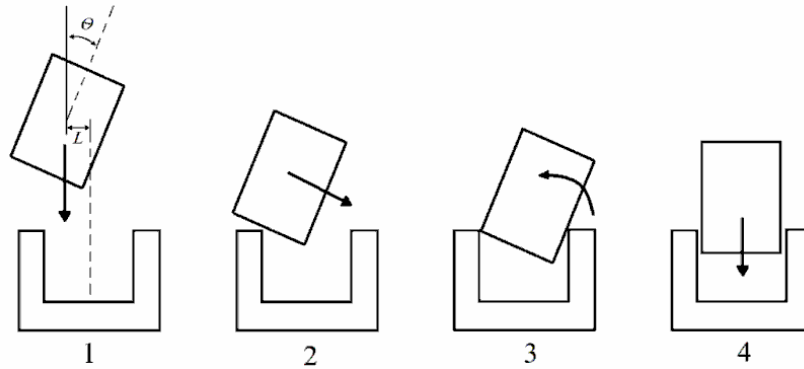


Figure 5-2. Example of a chamferless insertion strategy that requires the body of the peg to perform the chamfer crossing phase of assembly.

The success of the assembly process depends on how the compliant robot system reacts to the contact forces generated during phases two, three, and four from figure 5-1. Accordingly, a two-dimensional analysis of each of these phases will be conducted in the rest of this section to define a set of governing equations to model the forces generated during peg and hole contact. Using this information, values for the planar lateral and rotational stiffnesses as well as the compliance center location can be defined to ensure that the system avoids wedging and jamming. Since wedging and jamming are the two most commonly modeled modes of failure for peg and hole assembly, it is assumed that if the likelihood of these problems is minimized, then the success rate of the entire insertion task is maximized.

The initial positioning error of the peg relative to the hole, the geometry of the system, the forces generated from friction, and the compliance of the peg's support are

the driving factors behind the success or failure of any peg and hole assembly system. Wedging occurs instantly upon the onset of two-point contact if the geometry of the peg and hole create contact forces that align to create a compressive force that deforms the peg instead of trying to better align it with the hole. Wedging is avoided by maintaining proper alignment of the peg and hole as two-point contact approaches. Jamming occurs when the axial force that pushes the peg into the hole is directed too far away from the axis of insertion to actually push the peg into the hole. Jamming is avoided by designing the compliance of the peg to allow it to translate and become aligned as a result of the moments generated during two-point contact.

The system modeling performed in this section is based on the assembly model for compliantly supported rigid parts since the stiffness of the aluminum peg and hole is much higher than the positional and rotational stiffness of the impedance controlled WAM robots. As mentioned before, the success of peg and hole assembly rests on keeping the insertion force, peg, and hole properly aligned. By engineering the compliance of the complete system, it can be reasonably guaranteed that the rigid parts will be allowed to translate and rotate as needed to reject positional errors in the face of contact forces during assembly. To properly design the compliance required by each part of the system, the complete compliant system must be modeled using the geometry of the peg and hole. This is facilitated by the linear spring approximation that was proven in Chapter 4. In the desired system model, linear springs can act to impose a force on the peg as a reaction to translation or rotation of the parts during assembly. Since the peg and hole are allowed to translate and rotate in three dimensions, there are three rotations and three translations in which the peg and hole can move. Each of these degrees of freedom

must be assigned a virtual linear spring and be accounted for when organizing the compliance strategy for each part.

Since the peg and hole can move in a six DOF space, they can be encountered by external forces that can be arbitrarily oriented in the same six DOF space. The compliant interaction of the peg and hole as they encounter these external forces can be represented with the following equation.

$$U_{[6 \times 1]} = K_{[6 \times 6]} F_{[6 \times 1]} \quad (5.1)$$

Where U is displacement, K is the stiffness matrix, and F is a vector of external forces.

Using matrix dimensional analysis, it can be shown that designing the general stiffness of the system would require the selection of 36 variables. While this is possible and covered in published research, it is desirable to simplify this design process. As described in Chapter 2, this is partially accomplished by defining and maintaining a compliance center for the peg. This forces the above stiffness matrix to be diagonal, requiring only three translational and three rotational springs to completely define the behavior and the general compliance of the peg and hole. This simplification makes the modeling process much simpler since each plane of movement can essentially be defined by two springs, one translational and one rotational. To further simplify the modeling process, the compliance of the peg and hole must only be modeled in a single plane due to the axisymmetric geometry of the experimental system studied in this thesis. It is also worth noting that the following analysis is performed under the assumption that the assembly process is composed of relatively slow movements, which allows the insertion

to be studied as a quasi-static process. This allows each step of assembly to be considered to be in static equilibrium, which simplifies the study of the peg and hole's interaction forces since high-speed impacts are not a factor.

The derivation of the desired two-dimensional peg and hole system model begins by visualizing the necessary parameters of the system. The first item that needs to be identified is the clearance ratio of the peg and hole. This is a dimensionless value that quantitatively provides a measure of the clearance between the outer diameter of the peg and the inner diameter of the hole. This value is defined by the following equation.

$$c = \frac{2R - 2r}{2R} = \frac{R - r}{R} \quad (5.2)$$

Where R is the inside radius of the hole and r is the outside radius of the peg.

Wedging is primarily a function of the initial lateral and rotational error of the peg relative to the hole and the location of the peg's compliance center. To begin the study of peg and hole wedging, the first step is to examine the "wobble" angle available between the peg and hole when they are partially assembled as shown in the figure 5-3. From this diagram, a relation between the maximum amount of allowable angular error as a function of insertion depth can be made. This equation is shown below.

$$l \tan(\theta) = c2R \quad (5.3)$$

Where l is the length of the peg that has been inserted into the hole. This length is given by $l = z \cos(\theta)$ for the system shown in figure 5-3.

This equation basically says that the total amount of lateral translation at the tip of the peg, which is a function of rotational error, cannot physically exceed the boundary of the clearance between the peg and the inside of the hole. A visual representation of the total amount of wiggle angle for a generic peg and hole is shown in figure 5-3.

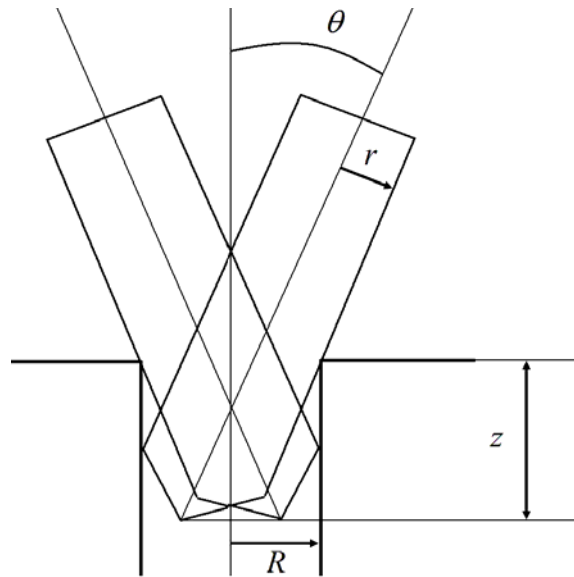


Figure 5-3. Diagram showing the wiggle angle of a peg that has been partially inserted into the hole.

Equation (5.3) is an important tool for the prediction of wedging. This equation shows that the insertion depth and wiggle angle are inversely proportional, meaning that as the insertion depth increases, the total amount of allowable wiggle angle decreases. For increasingly large insertion depths, the wiggle angle decreases and the possibility of success also increases, as wedging and jamming are unlikely for the small rotational errors allowed by the large insertion depth. However, special attention must be paid to the case of small insertion depths. This is because small insertion depths allow a greater range of wiggle angle, which can easily lead to both wedging and jamming. First,

wedging results when the two contact forces generated during two-point contact are pointed at each other and become compressive, storing energy in the peg in the form of deformation. These contact forces are largely friction limited, so a force analysis can be conducted using the idea of a friction angle, which is the two-dimensional equivalent of a friction cone. Figure 5-4 shows a two-dimensional model of a peg and hole with a shallow insertion depth that have become wedged.

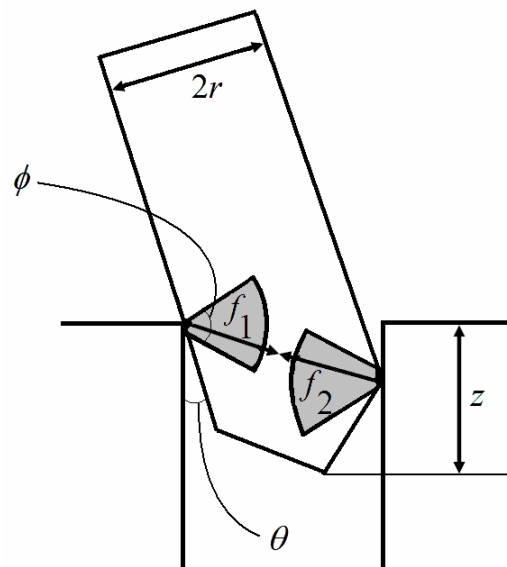


Figure 5-4. Diagram showing a peg that has become wedged in its hole. The wedging is caused by the alignment of the two friction forces that act to compress that peg rather than realign it with its hole.

The friction angle, ϕ , creates the arcs shown as the shaded regions in figures 5-4 and 5-5. The friction forces generated at the contact points must point away from the hole's inner surface as a vector located somewhere within these arcs. From the friction angle definition, it is known that $\tan(\phi) = \mu$, or conversely that $\phi = \tan^{-1}(\mu)$. Using figure 5-5, this relation can be rewritten as the following equation.

$$\mu = \tan(\phi) = \frac{l}{2r} \quad (5.4)$$

Rearranging the above equation results in the following.

$$l = \mu 2r \quad (5.5)$$

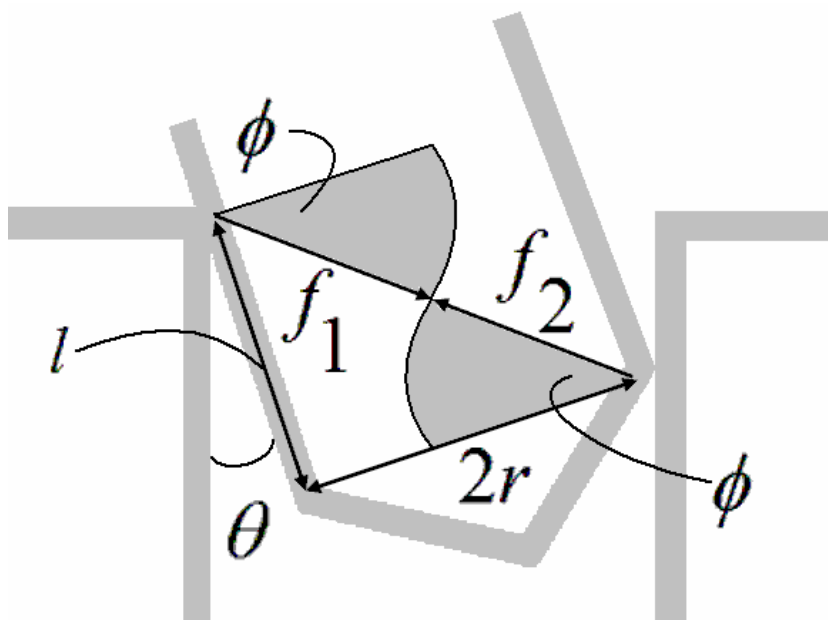


Figure 5-5. Diagram showing the minimum friction angle, ϕ , needed to cause the peg to become wedged in its hole. Using this information, the maximum rotational error that can be tolerated without the onset of wedging can be identified.

This equation represents the smallest insertion depth, l , for which wedging is possible. As stated before, the possibility of wedging becomes negligible for moderate insertion depths. Using the equation derived earlier to determine the wiggle angle of the peg, the maximum rotational error that can be tolerated to avoid wedging can be found.

This maximum rotational error will act as the upper limit on the allowed rotation of the peg relative to the hole, θ .

$$\mu 2r\theta = c 2R \quad (5.6)$$

$$\theta = \frac{c 2R}{\mu 2r} = \frac{(R-r)}{\mu r} \quad (5.7)$$

This is the maximum amount of rotational error that is allowed to ensure that wedging does not occur. When the rotational error of the peg relative to the hole is smaller than this value, the friction angles are too small for the contact forces to align. Limits on the amount of allowable lateral error must also be defined since lateral error can cause the peg to translate laterally and simultaneously rotate about its compliance center. This will cause additional rotational error between the peg and hole. Generally, the maximum amount of allowable lateral error between the peg and hole cannot be greater than the sum of the radius of the hole and the lateral width of the chamfer, which is equal to the radius of the peg in this case. This limit is obvious since an error greater than this would cause the peg to miss the hole completely. This limit is shown by the inequality represented by equation (5.8). Since only small insertion depths are being considered by this wedging study, this limit also represents the allowed initial lateral error, ε_0 , of the peg after phase one of figure 5-1.

$$-(r+R) < \varepsilon_0 < r+R \quad (5.8)$$

This general limit of the amount of lateral error possible must be refined further to limit the behavior of the system enough to avoid wedging. It was mentioned earlier that a compliantly supported peg will simultaneously rotate as it translates in response to reaction forces between the peg and hole unless the compliance center is located at the tip of the peg. Thus, translational reactions to contact forces will also affect the total rotational error of the peg relative to the hole. In figure 5-6, the horizontal translation of the tip of the peg, X , as it slides across the chamfer causes a moment about the center of compliance which increases the rotational error of the system.

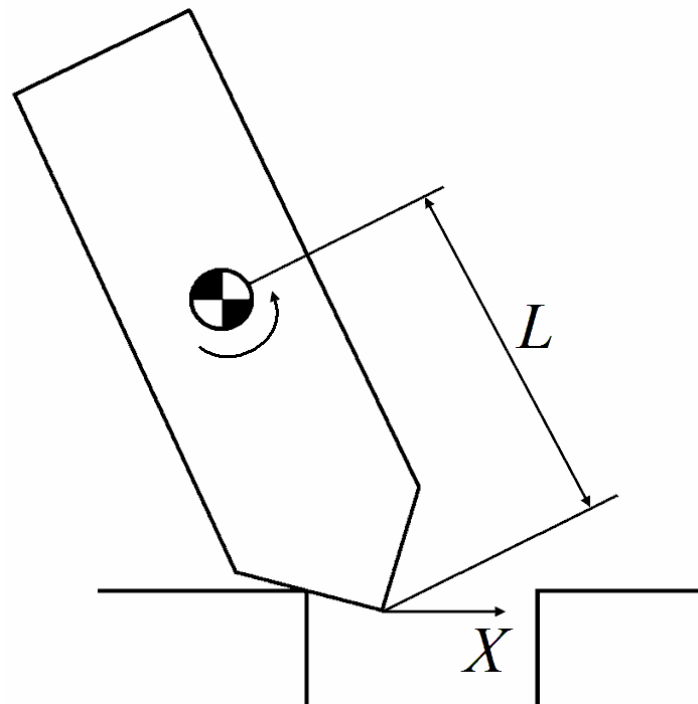


Figure 5-6. Coupled relation between increasing lateral displacement, X , and rotational error between the peg and the hole.

For this reason, the limit on the total amount of allowable rotational error must also account for the possible rotations that will arise from translations of the peg's tip. Whitney showed this relationship to take the form of equation (5.9) for the case of shallow insertion depths [1].

$$\theta_{total} = \theta_0 + S\epsilon_0 \quad (5.9)$$

Where $S = \frac{L}{L^2 + \frac{K_\theta}{K_x}}$ and K_θ, K_x are the rotational and lateral stiffnesses respectively.

Using the relations from equations (5.3) through (5.9), a two-dimensional plot can be created to visualize the possible combinations of initial lateral and rotational errors that will alleviate the concern of wedging. This plot is shown in figure 5-7. From this analysis, it has become apparent that wedging is primarily a function of the initial error of the peg relative to the hole. Thus, wedging avoidance actually becomes a design constraint for the accuracy of the visual compensation system and impedance controller more than compliance selection. As a result, the following diagram is used as a trajectory following performance goal for these controllers, but is not used to define the compliance settings of the system during fine motion insertion. In practice, the visual feedback system is able to actively align the peg and hole so accurately that wedging never becomes a concern.

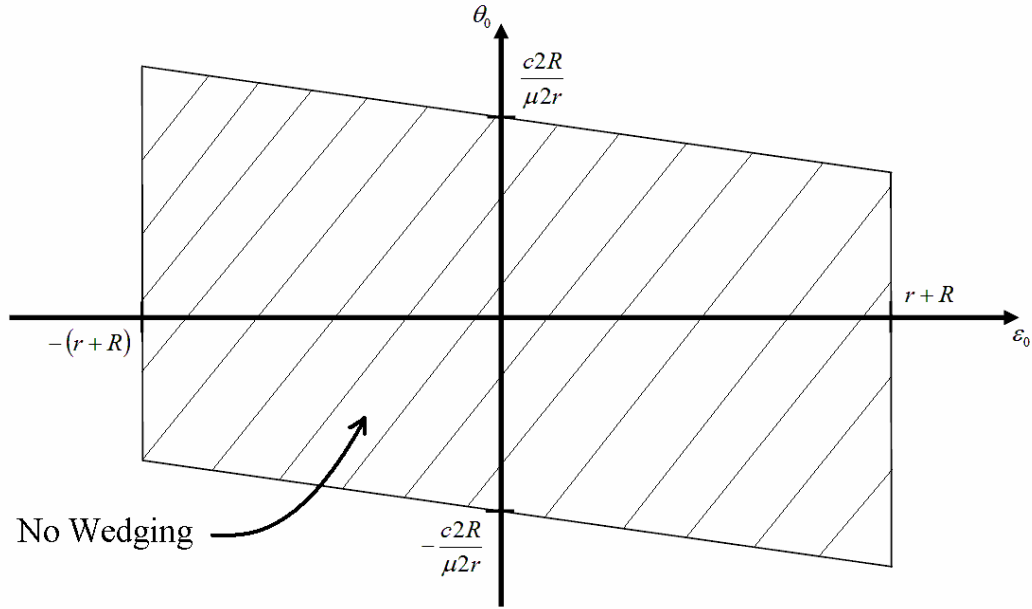


Figure 5-7. Wedging diagram that sets boundaries for the amount of initial lateral and rotational error between the peg and hole that can be tolerated before wedging will result. These boundaries are a function of part geometry and friction.

The region enclosed by the parallelogram in figure 5-7 indicates acceptable combinations of initial lateral and rotational error. The negatively sloped horizontal boundary lines are the result of the relation, S , between lateral error, compliance center location, and rotational error. For the case where the compliance center is located at the tip of the peg, these lines would be horizontal and the resulting plot would be rectangular. This is an indication that placing the compliance center of the peg at its tip is the best design decision with respect to wedging since that would result in the largest acceptable range of initial errors as shown by the wedging diagram. By removing the possible coupling between the translation and rotation of the peg due to interaction forces acting near its tip during chamfer crossing, the assembly process will be more likely to succeed in the face of initial positioning errors if the compliance center is located at the peg's tip.

Now that the problem of wedging has been addressed, the focus of the rest of this study must be shifted to the avoidance of jamming. Jamming is caused by unfavorable combinations of forces that are applied to the peg and combine to produce a resultant force that is no longer acting close enough to the axis of insertion to push the peg into the hole. In this two-dimensional analysis, these forces consist of F_x , F_z , and M . Whitney produced the jamming diagram in figure 5-8 to graphically demonstrate the combinations of applied forces that can guarantee the avoidance of jamming [1]. These combinations are those that lie within the bounds of the parallelogram. This diagram is widely used in peg and hole assembly analysis, and it is adopted by this thesis.

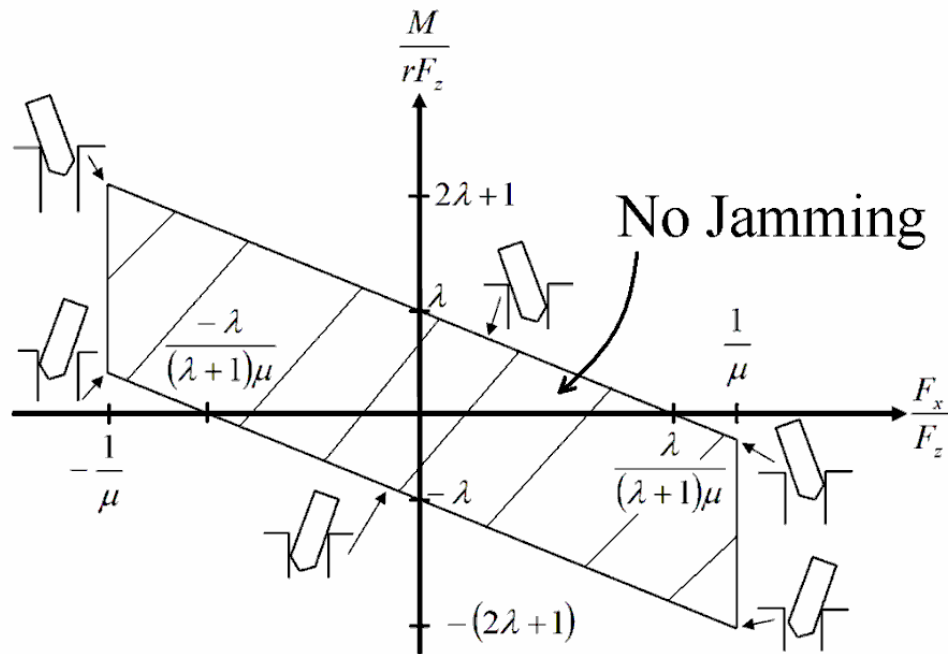


Figure 5-8. Jamming diagram used to set boundaries on the relation between insertion forces and reaction moments that will cause the peg to jam in its hole. The boundaries expand upward as a function of insertion depth as the peg advances into the hole, making success more likely as insertion depth increases.

Unlike the wedging diagram in figure 5-7, which had constant boundaries, the jamming diagram changes shape as a function of the insertion depth of the peg into the hole, l . This relationship is due to the variable λ , which partially defines the boundaries of the jamming diagram. This variable is defined by equation (5.10).

$$\lambda = \frac{l}{\mu 2R} \quad (5.10)$$

Since the insertion depth is the only variable in equation (5.10), it can be seen that there is a direct relationship between λ and l . Thus, as the assembly process proceeds and the insertion depth increases, so does λ . Looking back at figure 5-8, we can see that this increase also increases the height of the horizontal boundaries of the jamming diagram. The width of the vertical boundaries remains unchanged since they are a constant function of friction. This means that the likelihood of successful assembly increases as the peg is inserted farther into the hole, which is logical since the peg's insertion forces are constrained to a more aligned position as the insertion depth increases due to the wiggle angle defined by equation (5.3).

The jamming diagram defines the boundaries of the force and moment relations that lead to successful assembly. However, it does not provide any information on the values of the individual forces and moment applied to the peg during assembly. The equations needed predict the values of the individual forces and moment must be derived for each stage of assembly before the jamming diagram can be used. These applied forces, F_x , F_z , and M , are ultimately functions of the peg's compliance variables,

positional error, and the geometry of the system. Since the geometry and positional error allowed by the visual controller are constants for any assembly task, the jamming diagram can be directly used to tune the peg's compliance variables to achieve allowable combinations of forces that lie in the region of success in the jamming diagram. The production of contact forces is different for each stage of assembly. This requires the peg and hole system to be modeled separately for the three possible contact configurations; chamfer crossing, one-point contact, and two-point contact.

Chamfer crossing is the state during which the peg slides along its chamfer after it makes initial contact with the rim of the hole when there is lateral error present. The equations for the forces generated during chamfer crossing when the system consists of a chamfered peg and non-chamfered hole are derived below. Figure 5-9 shows the general geometry of the chamfer crossing phase of assembly.

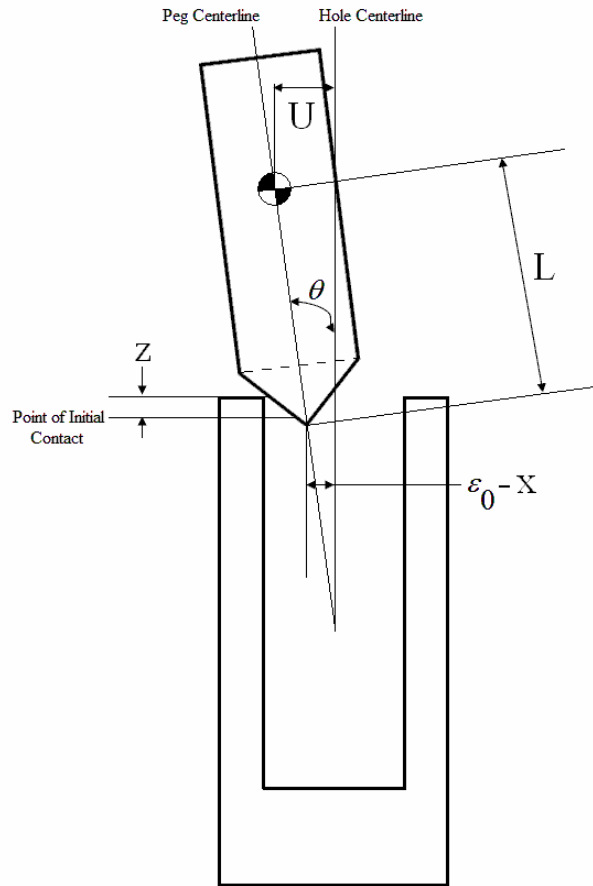


Figure 5-9. Peg and hole geometry during the chamfer crossing stage of peg and hole insertion.

During chamfer crossing, the single point of contact between the peg and the hole is the source of the reaction forces and moments that act to correct the lateral and rotational error between the peg and the hole when the peg is compliantly supported. However, the main concern of this analysis is to find the acceptable forces that can be applied to the peg by the manipulator. This will guide the design of the impedance controller parameters needed by the WAM performing the insertion of the peg to successfully complete the assembly task. This is accomplished by calculating the positional errors of the peg and how much they deform the virtual one-dimensional

springs used to model the compliant support of the peg in this analysis. Accordingly, the peg's error is measured by the position of the peg's compliance center since this point defines how far the virtual springs must deform to accommodate the error. This is because the compliance center is the point on the peg on which the virtual springs directly act in the system model. Looking at the initial conditions of the peg and hole in figure 5-9, it can be seen that the rotational error is simply the rotational angle of the peg, θ , and lateral error is given by the function $U = \varepsilon_0 + L\theta$. If the instant shown in figure 5-9 was the initial point of contact, then later equations would be defined using $U_0 = U$ and $\theta_0 = \theta$ as shown in this figure. Since this is the initial point of contact, it is assumed that the peg has not yet translated or rotated to accommodate positional errors. So the virtual springs supporting the peg have not yet deformed or produced any reaction to the contact forces applied to the peg at these initial lateral and rotational error values. Thus, any change in error from these initial conditions would result in a force applied to the compliance center of the peg by the two springs. These initial conditions can be modeled by the following equation.

$$U_0 = \varepsilon_0 + L\theta_0 \quad (5.11)$$

Where θ_0 is the initial rotational error.

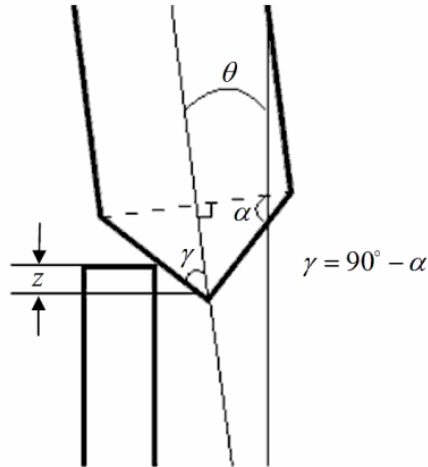


Figure 5-10. Variation of chamfer angle with peg rotational error.

To define an equation to relate the insertion depth of the peg to its resulting lateral position change, the design of the peg's chamfer must be considered. Unlike the typical case of a flat-ended peg being inserted into a chamfered hole, this experimental system has chamfer angles that vary with the rotation of the peg relative to the hole. If figure 5-10 is studied, the relation between insertion depth and lateral position change can be represented by equation (5.12).

$$X = \frac{z}{\tan\left(\theta + \frac{\pi}{2} - \alpha\right)} \quad (5.12)$$

Using this relation, a comprehensive equation can be written to model the relation between lateral displacement and the resulting coupled rotation of the peg. This relation is given by equation (5.13).

$$U = L \sin(\theta) - \frac{z}{\tan(\theta + \pi/2 - \alpha)} + \varepsilon_0 \quad (5.13)$$

However, two equations that represent θ and U independently must be derived to find the equations of the forces applied to the peg as a function of both variables. To do this, equations representing the general forces present when the peg and hole are in quasi-static equilibrium must be derived using statics. Figure 5-11 shows the forces being considered in this two-dimensional analysis.

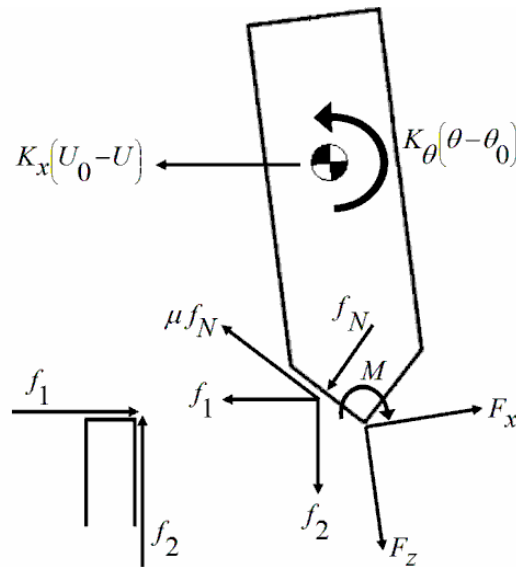


Figure 5-11. Free body diagram of the forces generated between the peg and hole during chamfer crossing.

This problem is solved by considering the contact forces and the forces applied by the virtual springs separately. As mentioned earlier, the contact forces between the peg and the hole are friction limited, thus they can be written as a function of the friction between the two pieces. This is accomplished with equations (5.14) and (5.15).

$$f_1 = f_N \left(\sin\left(\theta + \frac{\pi}{2} - \alpha\right) - \mu \cos\left(\theta + \frac{\pi}{2} - \alpha\right) \right) \quad (5.14)$$

$$f_2 = f_N \left(\cos\left(\theta + \frac{\pi}{2} - \alpha\right) + \mu \sin\left(\theta + \frac{\pi}{2} - \alpha\right) \right) \quad (5.15)$$

Since these two friction forces are the only external forces exerted onto the peg by the environment during chamfer crossing, these are the only equations necessary to completely model the contact forces and the forces applied to the peg by the virtual springs of the robot's impedance controller. It is also worth noting that the moment applied to the tip of the peg is also a function of the friction forces acting about the compliance center of the peg by some distance that is a function of the lateral error and rotation of the peg. This small distance acts as the moment arms for the horizontal and vertical components of the friction force. Thus, the lateral and insertion forces and moment applied to the peg are given by equations (5.16) through (5.18).

$$F_x = -f_1 \quad (5.16)$$

$$F_z = f_2 \quad (5.17)$$

$$M = f_1(L \cos(\theta) - z) + f_2 \left(R - \varepsilon_0 - \frac{z}{\tan\left(\theta + \frac{\pi}{2} - \alpha\right)} - L \sin(\theta) \right) \quad (5.18)$$

However, if it is assumed that the initial lateral and rotational errors are small, which is a valid assumption based on the requirements of the wedging diagram, the moment equation becomes much more simple as it can be closely approximated by

equation (5.19). This will greatly reduce the complexity of future equations representing θ as a function of insertion depth.

$$M = f_2 r \quad (5.19)$$

The forces applied to the peg by the impedance controller of the robot are simply a function of the lateral and rotational displacements that result from the contact forces. This is because we have chosen to model the impedance controller behavior as a set of passive linear spring. These applied forces are represented by equations (5.20) and (5.21). Note that the insertion force, F_z , is applied to the peg by the controller and is largely constant and not a function of the peg and hole interaction. Thus, it should be considered to be large enough to overcome the vertical component of the friction force, f_2 , but it does not need to be solved to complete the static analysis model.

$$F_x = -K_x(U_0 - U) \quad (5.20)$$

$$M = K_x L(U_0 - U) - K_\theta(\theta - \theta_0) \quad (5.21)$$

Combining equations (5.11) , (5.13)-(5.15), (5.19), and (5.21) derived for the chamfer crossing model results in the individual equation for the peg's rotational error as a function of insertion depth. This equation is shown as (5.22).

$$\theta = \theta_0 + \frac{K_x \left(\frac{z}{\tan(\theta + \pi/2 - \alpha)} \right) \left(L(\sin(\theta + \pi/2 - \alpha) - \mu \cos(\theta + \pi/2 - \alpha)) - r(\cos(\theta + \pi/2 - \alpha) + \mu \sin(\theta + \pi/2 - \alpha)) \right)}{(K_x L^2 + K_\theta) \left(\sin(\theta + \pi/2 - \alpha) - \mu \cos(\theta + \pi/2 - \alpha) \right) - K_x L r (\cos(\theta + \pi/2 - \alpha) + \mu \sin(\theta + \pi/2 - \alpha))} \quad (5.22)$$

Applying the assumption of small rotational error, this equation can be simplified further since the chamfer angle on the peg can be assumed to remain approximately constant as it will not vary considerably for small rotations. Thus, the equation for the rotation of the peg as a function of insertion depth becomes the following.

$$\theta = \theta_0 + \frac{K_x \left(\frac{z}{\tan(\pi/2 - \alpha)} \right) \left(L(\sin(\pi/2 - \alpha) - \mu \cos(\pi/2 - \alpha)) - r(\cos(\pi/2 - \alpha) + \mu \sin(\pi/2 - \alpha)) \right)}{(K_x L^2 + K_\theta) \left(\sin(\pi/2 - \alpha) - \mu \cos(\pi/2 - \alpha) \right) - K_x L r (\cos(\pi/2 - \alpha) + \mu \sin(\pi/2 - \alpha))} \quad (5.23)$$

Similarly, an equation to model the lateral displacement of the peg during chamfer crossing as a function of insertion depth can be defined. This equation is shown below.

$$U = U_0 + \frac{K_\theta \left(\frac{z}{\tan(\pi/2 - \alpha)} \right) \left(\sin(\pi/2 - \alpha) - \mu \cos(\pi/2 - \alpha) \right)}{(K_x L^2 + K_\theta) \left(\sin(\pi/2 - \alpha) - \mu \cos(\pi/2 - \alpha) \right) - K_x L r (\cos(\pi/2 - \alpha) + \mu \sin(\pi/2 - \alpha))} \quad (5.24)$$

If we plug equations (5.23) and (5.24) into equations (5.16) through (5.21), we can obtain an equation for the required insertion force, F_z , applied lateral force, F_x , and applied moment, M , as a function of insertion depth during chamfer crossing. These equations are given below.

$$F_z = \frac{K_x K_\theta \left(\cos\left(\frac{\pi}{2} - \alpha\right) + \mu \sin\left(\frac{\pi}{2} - \alpha\right) \right) \left(\frac{z}{\tan\left(\frac{\pi}{2} - \alpha\right)} \right)}{\left(K_x L^2 + K_\theta \right) \left(\sin\left(\frac{\pi}{2} - \alpha\right) - \mu \cos\left(\frac{\pi}{2} - \alpha\right) \right) - K_x L r \left(\cos\left(\frac{\pi}{2} - \alpha\right) + \mu \sin\left(\frac{\pi}{2} - \alpha\right) \right)} \quad (5.25)$$

$$F_x = \frac{-K_x K_\theta \left(\frac{z}{\tan\left(\frac{\pi}{2} - \alpha\right)} \right) \left(\sin\left(\frac{\pi}{2} - \alpha\right) - \mu \cos\left(\frac{\pi}{2} - \alpha\right) \right)}{\left(K_x L^2 + K_\theta \right) \left(\sin\left(\frac{\pi}{2} - \alpha\right) - \mu \cos\left(\frac{\pi}{2} - \alpha\right) \right) - K_x L r \left(\cos\left(\frac{\pi}{2} - \alpha\right) + \mu \sin\left(\frac{\pi}{2} - \alpha\right) \right)} \quad (5.26)$$

$$M = \frac{K_x L K_\theta \left(\frac{z}{\tan\left(\frac{\pi}{2} - \alpha\right)} \right) \left(\sin\left(\frac{\pi}{2} - \alpha\right) - \mu \cos\left(\frac{\pi}{2} - \alpha\right) \right)}{\left(K_x L^2 + K_\theta \right) \left(\sin\left(\frac{\pi}{2} - \alpha\right) - \mu \cos\left(\frac{\pi}{2} - \alpha\right) \right) - K_x L r \left(\cos\left(\frac{\pi}{2} - \alpha\right) + \mu \sin\left(\frac{\pi}{2} - \alpha\right) \right)}$$

$$- \frac{K_x K_\theta \left(\frac{z}{\tan\left(\frac{\pi}{2} - \alpha\right)} \right) \left(L \left(\sin\left(\frac{\pi}{2} - \alpha\right) - \mu \cos\left(\frac{\pi}{2} - \alpha\right) \right) - r \left(\cos\left(\frac{\pi}{2} - \alpha\right) + \mu \sin\left(\frac{\pi}{2} - \alpha\right) \right) \right)}{\left(K_x L^2 + K_\theta \right) \left(\sin\left(\frac{\pi}{2} - \alpha\right) - \mu \cos\left(\frac{\pi}{2} - \alpha\right) \right) - K_x L r \left(\cos\left(\frac{\pi}{2} - \alpha\right) + \mu \sin\left(\frac{\pi}{2} - \alpha\right) \right)} \quad (5.27)$$

Using these three equations, the ratios of the forces applied to the peg can be estimated to determine where they fall on the jamming diagram. In particular, we are interested in the ratios $\frac{M}{rF_z}$ and $\frac{F_x}{F_z}$. Looking closely at these equations, it can be seen that they are only a function of insertion depth, compliance parameters, the coefficient of friction, and the chamfer angle of the peg. Since acceptable ranges for each of these ratios

is known for every insertion depth *a priori* based on the physical geometry of the peg and hole, these equations can be used to select acceptable ranges of the compliance parameters for each insertion depth. Keeping the compliance parameters of the impedance controller within these ranges during assembly will create an insertion system that is theoretically immune to wedging and jamming. Since chamfer crossing is only possible when at least some part of the peg's chamfer is located outside of the hole, we know that equations (5.25)-(5.27) are valid as long as the insertion depth is not greater than the height of the chamfer. Next, the case of one-point contact is considered by the quasi-static peg and hole model. Figure 5-12 below shows the two-dimensional model of the one-point contact case.

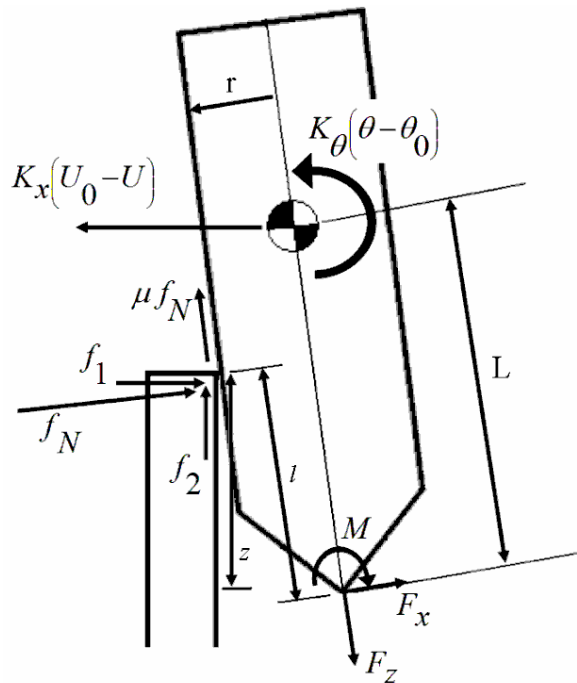


Figure 5-12. Peg and hole geometry and free body diagram for the one-point contact phase of assembly.

Using the one-point contact geometry model, the same force analysis must be performed. Following the same process used to study the chamfer crossing phase, the equation for the lateral displacement of the peg's center of compliance can be found for the case when the peg has fully entered the hole. This equation is shown below.

$$U = cR + L \sin(\theta) - z \sin(\theta) \quad (5.28)$$

For the one-point contact case, there is a single equation to model the relation between the lateral and rotational error of the peg relative to the hole. This equation is shown below.

$$U_0 - U = \varepsilon_0 - cR + L(\theta_0 - \theta) + l\theta \quad (5.29)$$

Using the same equations to represent the peg's contact and applied forces as in (5.16) through (5.21), the independent equations for the rotation and lateral displacement of the peg can be found for the one-point contact case. These equations are given below.

$$\theta = \frac{K_x(L-l-\mu r)(\varepsilon_0 - cR + L\theta_0) + K_\theta\theta_0}{K_x(L-l-\mu r)(L-l) + K_\theta} \quad (5.30)$$

$$U = U_0 - \frac{K_\theta(\varepsilon_0 - cR + L\theta_0)}{K_x(L-l-\mu r)(L-l) + K_\theta} \quad (5.31)$$

Substituting equations (5.30) and (5.31) into equations (5.16) through (5.21), results in an equation for the required insertion force, F_z , applied lateral force, F_x , and applied moment, M , as a function of insertion depth during the one-point contact stage of assembly. These equations are given below.

$$F_z = \frac{\mu K_x K_\theta (\varepsilon_0 - cR + L\theta_0)}{K_x (L - l - \mu r)(L - l) + K_\theta} \quad (5.32)$$

$$F_x = -\frac{K_x K_\theta (\varepsilon_0 - cR + L\theta_0)}{K_x (L - l - \mu r)(L - l) + K_\theta} \quad (5.33)$$

$$M = \frac{K_x L K_\theta (\varepsilon_0 - cR + L\theta_0)}{K_x (L - l - \mu r)(L - l) + K_\theta} - K_\theta \left(\frac{K_x (L - l - \mu r)(\varepsilon_0 - cR + L\theta_0) + K_\theta \theta_0}{K_x (L - l - \mu r)(L - l) + K_\theta} - \theta_0 \right) \quad (5.34)$$

These equations can then be used to select compliance parameters that alleviate the possibility of wedging and jamming for insertion depths in which the one-point contact state is dominant. To finish the peg and hole modeling process, the same analysis must be performed for the case of two-point contact. The geometry of the two-point contact case is shown in figure 5-13 below.

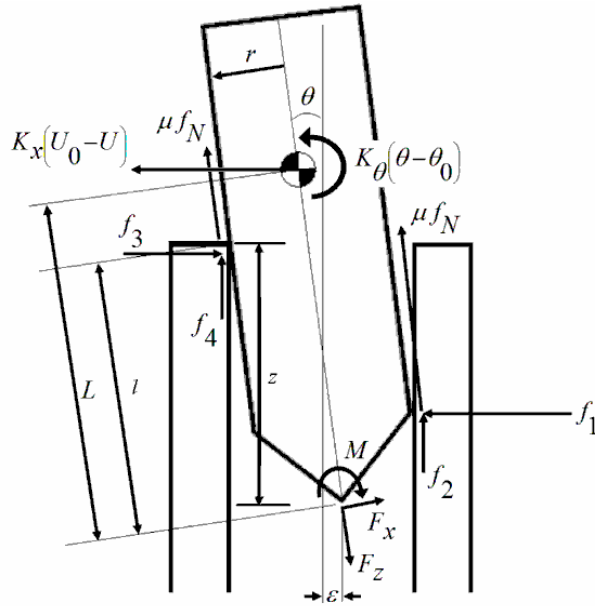


Figure 5-13. Peg and hole geometry and free body diagram for the two-point contact phase of assembly.

Unlike the previous two cases, an equilibrium force analysis does not need to be performed to find the equations for the rotation and translation of the peg as a function of insertion depth for the two-point contact case. This is because the system is fully constrained geometrically. The two-point contact analysis instead begins with the equation derived earlier to represent the wiggle angle for a peg that has been inserted a variable depth into its hole. This equation is reproduced below.

$$l \tan(\theta) = c2R \quad (5.35)$$

After rearranging and modifying this equation so that it more accurately reflects the constraints imposed on the peg by the hole's wall for all θ , the equation becomes the following.

$$R = \frac{l}{2} \tan(\theta) + r \cos(\theta) \quad (5.36)$$

From equation (5.35), it can be shown that as insertion depth increases, the amount of possible rotational error decreases. Since this analysis is being performed for the two-point contact phase of assembly, it can reasonably be assumed that the peg has been inserted a substantial distance into the hole by this assembly phase. This means that only small rotational errors are possible during this stage of assembly. Applying the small rotational error assumption transforms equation (5.35) into equation (5.37) shown below.

$$\theta = \frac{c2R}{l} \quad (5.37)$$

Substituting equation (5.37) into equation (5.29) from the one-point contact analysis results in an equation that relates the lateral and rotational error of the peg during the two-point contact stage of assembly. This equation is shown below.

$$U_0 - U = \varepsilon_0 + cR + L(\theta_0 - \theta) \quad (5.38)$$

A different approach must also be used to find the equations that model the required insertion force, F_z , applied lateral force, F_x , and applied moment, M , as a function of insertion depth for the two-point contact case. This is because there are new force equilibrium equations to account for the additional support location acting on the

peg where it has come into contact with the hole for a second time. Using figure 5-13, the following equilibrium equations can be found.

$$F_x = f_2 - f_1 \quad (5.39)$$

$$F_z = \mu(f_1 + f_2) \quad (5.40)$$

$$M = f_1 l - \mu r(f_2 - f_1) \quad (5.41)$$

Combining equations (5.19), (5.20), (5.37), and (5.38) with the above equilibrium equations for the two-point contact case will result in two equations for the lateral force and moment equations of the peg. These two equations are shown below.

$$F_x = -K_x L \left(\theta_0 - \frac{cD}{l} \right) - K_x (\varepsilon_0 + cR) \quad (5.42)$$

$$M = \left(K_x L^2 + K_\theta \right) \left(\theta_0 - \frac{c2R}{z} \right) + K_x L (\varepsilon_0 + cR) \quad (5.43)$$

Finding the insertion force, F_z , is a little more involved since it must be compatible with the force and moment produced by equations (5.42) and (5.43). Equations (5.39) through (5.41) can be combined to yield the following compatibility equation for the three forces of interest.

$$\frac{M}{rF_z} = \pm\lambda - \frac{F_x}{F_z} \mu(1 + \lambda) \quad (5.44)$$

Where $\lambda = \frac{l}{2r\mu}$ from equation (5.10).

Substituting equations (5.42) and (5.43) into this compatibility equation and solving for F_z yields the following equation to model the required insertion force as a function of insertion depth for the two-point contact state.

$$F_z = \frac{2\mu}{l} \left[(K_x L^2 + K_\theta) \left(\theta_0 - \frac{c2R}{l} \right) + K_x L (\varepsilon_0 + cR) \right] + \mu \left(1 + \frac{\mu 2r}{l} \right) \left[-K_x L \left(\theta_0 - \frac{c2R}{l} \right) - \frac{K_x L (\varepsilon_0 + cR)}{L} \right] \quad (5.45)$$

Two-point contact only occurs after the peg has been inserted far enough into the hole to reach both sides of the hole for a given rotation angle. Using a simplified force analysis, Whitney showed that in general, two-point contact will begin at the following insertion depth [1].

$$l_{start2-point} \cong \frac{c2R}{\theta_0} \quad (5.46)$$

He also states that two-point contact can be shown to terminate around the following insertion depth. At this point, the two-point contact turns into line contact,

where the peg is resting flat against the inner wall of the hole as shown in phase five of figure 5-1.

$$l_{end2-point} \cong \frac{K_{\theta}\theta_0}{K_x(\varepsilon_0 + cR)} - l_{start2-point} \quad (5.47)$$

This is the last equation needed to model the peg and hole system with respect to the jamming diagram. This model will allow the designer to select compliance values that theoretically guarantee successful assembly. Combining this jamming diagram analysis with the results from the *modeFrontier* impedance controller parameter optimization performed in section 7.4 will produce a range of each compliance variable for which successful assembly is guaranteed. The complete design process and an overview of the *modeFrontier* optimization software is provided in Chapter 7.

5.2 Coupled Impedance Control Stability Analysis

The previous section derived the peg and hole model that will be used to design the stiffness parameters for the impedance controller of the WAM holding the peg to guarantee wedging and jamming will not occur. However, the effects these stiffness changes have on the overall stability of the coupled system that results from the interaction of two impedance controlled robots should also be considered. For this analysis, the physical equivalence conjecture will be applied to the coupled system. This conjecture says that the impedance controller, which behaves as a spring-mass-damper system, must follow the same stability requirements of an equivalent physical spring-mass-damper system. The following section uses this method to perform a robustness

analysis for an equivalent physical system that embodies the stiffness settings chosen to accommodate the peg and hole assembly process. The first step in this analysis is the creation of a one dimensional spring-mass-damper model that represents the dynamics of the coupled system. There are many approaches to the design of this model that can be chosen depending on the complexity and number of system properties needed to accurately represent the behavior of the robotic system. In this case, a linear two DOF spring-mass-damper model will be designed to model the behavior of the coupled system.

For the case of a linear system, Colgate [62] proved that the system must have a positive real driving point impedance at any interaction port at which the impedance controller interacts with a passive linear environment to be guaranteed to be stable. One approach to impedance controller stiffness design that satisfies this requirement is to simply make the robot considerably more stiff than everything the robot will be interacting with, allowing the robot to reject error through higher control forces. However, this will not be a viable solution in this experimental system as two robots are to be working together. In this configuration, both robots cannot be significantly stiffer than each other, so a more intensive design process must be performed.

The hardware used in the MTTC robotics research lab consists of two WAM robots that will be working together to insert a peg into a hole. To analyze the stability of this system using the techniques developed by Hogan and Colgate [62], a linear physical system must be created to model the coupled system that occurs during assembly when the two robots are interacting with each other. The resulting model is shown in figure 5-14. In this figure, M_1 represents the effective mass of the robot's peg end effector as it is seen by the impedance controller. In other words, the value defined for this mass should

represent the total mass experienced by the impedance controller after the effects of inertia and gravity compensation have been added to the control system. B_1 represents the physical damping that results from joint friction and inertia that are inevitable as the insertion robot is moving. This damper is located behind the mass since it acts to slow movement in the physical system. K_1 represents the stiffness of the entire WAM drivetrain, to include backlash and backdrivability. This is placed in front of the mass since it acts to push to the end effector of the insertion WAM as seen by the controller. E is the impedance control force that is applied to the peg by the WAM as it is inserted into the hole. This is where the variable compliance controller acts to modify the stiffness of the system associated with the robot's motion. The control force, E , is a function of the impedance controller. In its most simple implementation, E takes the following form.

$$E = -K_E(X_2 - X_0) - B_E(V_2 - V_0) \quad (5.48)$$

Since it is assumed that the coupled robotic system can be approximated by the linear model shown in figure 5-14, equation (5.48) represents the only impedance control terms that can affect the stability of the coupled system. It is also worth noting that it is beneficial to separate the physical stiffness and damping values from those virtually imposed by the impedance controller. This models the fact that there are other factors working in the system that the controller must compensate for, such as the uncontrolled compliance of the robot's hardware. This allows the design process to accommodate the natural behavior of the coupled system to obtain better performance from the system. To

model the passive environment created by the other WAM holding the hole, the right side of the linear model consists of a mass that is compliantly supported by a spring and damper that are imposed by the second impedance controller. These variables are M_2 , K_2 , and B_2 respectively. The general behavior of the second WAM is the reason it was modeled differently. Unlike the WAM holding the peg that moves to perform the insertion, the passive half of the system is only capable of remaining as stationary as possible and absorbing forces from the peg. It can only be displaced from its initial position and return to it. The force acting on the passive system, F , is the reaction force that is generated during contact. The one dimensional model of the coupled system is illustrated in figure 5-14.

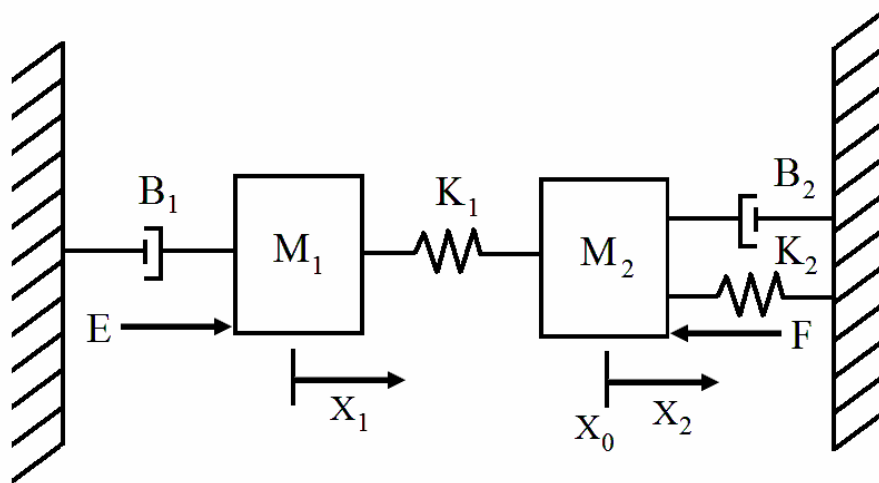


Figure 5-14. Spring-mass-damper physical equivalence model of the coupled dual impedance controlled robot system.

To analyze the stability of the system, a transfer function that represents the dynamics of the system must be developed. This can take on two forms, either a ratio of

the Cartesian position to input force or it can also be in the form of Cartesian velocity to input force, which is the transfer function used in this case. Figure 5-14 is a two degree of freedom system since each mass can remain still while the other moves. This means that two separate equations are needed to define the behavior of the system. These equations of motion for each mass were found using the free-body diagram superposition method. The Laplace transforms of the two equations of motion are shown below.

$$E = -K_1 X_2(s) - (B_1 s + M_1 s^2 + K_1) X_1(s) \quad (5.49)$$

$$F = K_1 X_1(s) - (K_2 + B_2 s + K_1 + M_2 s^2) X_2(s) \quad (5.50)$$

After taking the inverse Laplace transform of the above equations and assuming that there are zero initial conditions, the following two equations that lie in the time domain will result.

$$E = -K_1 X_2 - B_1 \dot{X}_1 - M_1 \ddot{X}_1 - K_1 X_1 \quad (5.51)$$

$$F = K_1 X_1 - K_2 X_2 - B_2 \dot{X}_2 - K_1 X_2 - M_2 \ddot{X}_2 \quad (5.52)$$

Using these equations, it is easy to find the state equations for the one dimensional system. First, the following variable definitions are made to relate the acceleration, velocity, and position of each mass.

$$\ddot{X}_1 = \dot{V}_1$$

$$V_1 = \dot{X}_1$$

$$\ddot{X}_2 = \dot{V}_2$$

$$V_2 = \dot{X}_2$$

Then the state variables are chosen to be X_1 , V_1 , X_2 , and V_2 . Using these selections, the time domain equations of motion become the following.

$$E = -K_1X_2 - B_1V_1 - M_1\dot{V}_1 - K_1X_1 \quad (5.53)$$

$$F = K_1X_1 - K_2X_2 - B_2V_2 - K_1X_2 - M_2\dot{V}_2 \quad (5.54)$$

Writing these equations in vector matrix form gives the state representation of the system.

$$\begin{bmatrix} \dot{X}_1 \\ \dot{V}_1 \\ \dot{X}_2 \\ \dot{V}_2 \end{bmatrix} = \begin{bmatrix} 0 & 1 & 0 & 0 \\ -\frac{K_1}{M_1} & -\frac{B_1}{M_1} & -\frac{K_1}{M_1} & 0 \\ 0 & 0 & 0 & 1 \\ \frac{K_1}{M_2} & 0 & -\frac{(K_1+K_2)}{M_2} & -\frac{B_2}{M_2} \end{bmatrix} \begin{bmatrix} X_1 \\ V_1 \\ X_2 \\ V_2 \end{bmatrix} + \begin{bmatrix} 0 \\ -\frac{1}{M_1} \\ 0 \\ 0 \end{bmatrix} E + \begin{bmatrix} 0 \\ 0 \\ 0 \\ -\frac{1}{M_2} \end{bmatrix} F \quad (5.55)$$

Now that the system has been modeled, the control equation stated in equation (5.48) can be applied to find the transfer function that relates the net force input into the system to the system's output velocity. The reason this transfer function was chosen, as

opposed to finding the transfer function of net force to displacement, is due to the velocity controlled nature of the impedance controller. As mentioned in section 4.1, impedance control is based around the Jacobian matrix, which relates joint velocity to Cartesian velocity. So the velocity transfer function should provide a better model of the actual robot dynamics from the impedance controller perspective. The focus of this study is to consider the coupled effects of the system once the two robots have come into contact with each other. As a result, the system will be studied from the reference frame of the hole, which will only have a velocity output after contact has been established between the peg and hole. The resulting transfer function is shown below.

$$\frac{V_2(s)}{F(s)} = \frac{s(M_1s^2 + B_1s + K_1)}{M_1M_2s^4 + (B_1M_2 + B_2M_1)s^3 + (B_1B_2 + K_1M_1 + K_2M_1 + K_1M_2)s^2 + (B_1(K_1 + K_2) + K_1(B_2 + B_E))s + K_1(K_2 + K_E)} \quad (5.56)$$

Even though the one dimensional model derived earlier applies directly to the state of contact between the robots, it must be shown that the system, including the selected impedance parameters, satisfies the conditions for both free-space and coupled stability to prove that the system is globally stable. Colgate and Hogan clearly derived these conditions for stability. They proved that in order for the system to be stable under free-space operation, the poles of the above transfer function must lie in the left half plane. They also proved that in order for the controlled system to be stable when coupled to a passive environment, the transfer function must also be positive definite. Applying each of the constraints to the above transfer function yields a set of inequalities that will

be used to guide the selection of the impedance controller variables. It is also worth noting that because the WAM manipulating the hole is always set to some nominal stiffness and damping coefficients that do not vary, the only variables in the coupled system model become the stiffness and damping impedance control parameters of the WAM guiding the peg into the hole. These stiffness parameters are the same variables that were used in the previous section to guarantee successful assembly. Thus, a set of stiffness and damping values that satisfy both sets of constraints will result in a coupled assembly system that guarantees successful assembly and controller stability. This is essentially the analysis that will be performed Chapter 7.

Applying the left hand plane pole position constraint to the denominator of the transfer function results in the following constraints that must be satisfied by the impedance controller's virtual stiffness and damping. Satisfying these constraints will guarantee the stability of the system when it is operating in free-space, or when the contact force, F , is zero between the peg and hole.

$$-B_2 - B_1 \left(\frac{K_1 + K_2}{K_1} \right) \leq B_E \leq \frac{B_1^2 B_2}{K_1 M_1} + \frac{B_1 B_2^2}{K_1 M_2} + \frac{B_1 M_2}{M_1} + \frac{B_2 M_1 (K_1 + K_2)}{K_1 M_2} \quad (5.57)$$

$$K_E \geq -K_2 \quad (5.58)$$

$$K_E \leq \frac{[B_1(K_1 + K_2) + K_1(B_2 + B_E)] [B_1^2 B_2 M_2 + B_1 B_2^2 M_1 + B_1 K_1 M_2^2 + B_2 M_1^2 (K_1 + K_2) - K_1 M_1 M_2 B_E]}{K_1 (B_1 M_2 + B_2 M_1)^2} - K_2 \quad (5.59)$$

Applying the positive definite function condition to the transfer function produces the following constraints on the impedance control variables. These constraints must be satisfied to guarantee that the system will also remain stable when the two masses in the model are coupled and a contact force is being exerted on the insertion WAM's impedance controller.

$$K_1^2(B_1 + B_2 + B_E) - B_1 K_E^2 \geq 0 \quad (5.60)$$

$$B_1^2 B_2 - B_2 K_1 M_1 - K_1 M_1 (B_2 + B_E) \leq 0 \quad (5.61)$$

$$\left[B_1^2 B_2 - B_2 K_1 M_1 - K_1 M_1 (B_2 + B_E) \right]^2 - 4 B_2 M_1^2 \left[K_1^2 (B_1 + B_2 + B_E) - B_1 K_1 K_E \right] \leq 0 \quad (5.62)$$

Similar to the wedging and jamming diagrams shown in the previous section, these inequalities can be plotted on a single two-dimensional plane to visualize the effects of each constraint. The axes of this stability constraint plot correspond to the impedance controller's stiffness and damping parameters, K_E and B_E . The completed plot will enclose an area that represents all of the possible combinations of stiffness and damping parameters that can be chosen to meet the requirements of a globally stable system. To show what a plot of the two-dimensional constraints would look like, an example system with the following parameters as related to figure 5-14 will be studied.

$$M_1 = M_2 = 1.0$$

$$K_1 = 600$$

$$K_2 = 300$$

$$B_1 = 4$$

$$B_2 = 6$$

If each of the constraining equations (5.57) through (5.62) are plotted for these variables as functions of the impedance controller's stiffness and damping values, the following plot of the boundaries placed on the parameters by each condition is the produced. There is an obvious and large area on the plot that corresponds to combinations of damping and stiffness that satisfy all of the stability requirements of the system. This area is cross hatched in the plot in figure 5-15.

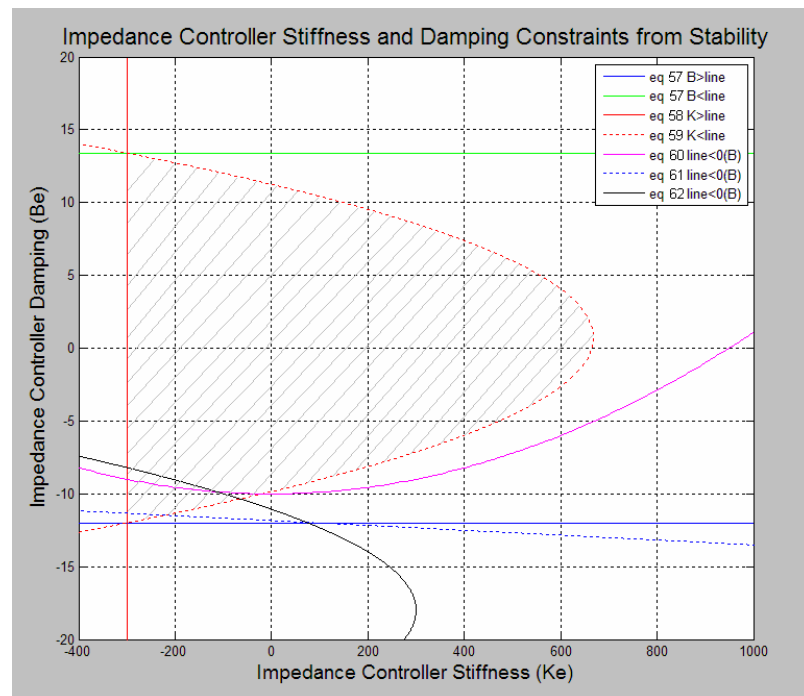


Figure 5-15. Graphical representation of the constraints imposed on the stiffness and damping gains of the peg's impedance controller by the coupled system stability criteria. The shaded region represents the acceptable combinations of stiffness and damping.

These ranges of acceptable stiffness and damping gains are then tested using the peg and hole analysis from the previous section to find combinations of the variables that also provide guaranteed avoidance of jamming in addition to coupled stability. The acceptable combinations of variables that satisfy both sets of requirements are then programmed into the variable compliance controller developed in the next chapter. This enables the system to vary the stiffness of the peg between acceptable combinations of variables as needed during assembly to avoid wedging and jamming. This process is described in more detail in the following chapter.

CHAPTER 6

SYSTEM LEVEL CONTROLLERS

In this chapter, the design and performance of the system level controllers that run on the main control computer are presented. These include the visual trajectory compensation controller and the variable compliance controller. The following section provides an overview of the of the computer vision system that provides sensory feedback to the trajectory compensation controller.

6.1 Vision System

To provide the feedback information needed by the trajectory compensation controller, the vision system needs to be capable of performing three tasks. First, it must be able to recognize which object is the peg and which is the hole within its field of view. It must then find and track the pixel coordinates that correspond to the X and Y position of the tip of each part within the camera's image plane since this is the most important part to be aligned during assembly. Finally, the vision system must also measure the orientation of the parts in the image plane to allow the bodies of the peg and hole to be aligned along the axis of insertion. The system designed to provide this visual feedback was designed to be as simple as possible. This was done for two reasons. First, there are many different forms of stereo triangulation and multi-camera projection that are capable of providing this type of information. However, each of these systems must be carefully calibrated to achieve the sub-millimeter accuracy that is beneficial to the peg and hole assembly system. The calibration process can be tedious and must be redone every time

the cameras are moved in any way. Eliminating this setup step is a huge advantage in the MTTC robotics research lab since its equipment is moved from day to day to accommodate different research projects. Second, and most important, eliminating the complexity associated with more cameras or triangulation algorithms increases the speed at which visual information is output to the controller. The compiled code that makes up the system level controllers runs at a speed close to 100Hz, while well designed triangulation algorithms typically hover around the 20Hz range with the available computing power of the control computer. This is a huge bottleneck that notably affects the performance of the system. Simplifying the vision system increases the bottleneck speed to about 80Hz, which allows the controllers to compensate for system errors four times faster.

The general goal of the vision system is to monitor all six DOF of the peg and hole. However, the axisymmetric peg and hole studied in this thesis eliminates the need to monitor the rotation of the parts about the axis of insertion since any changes to this DOF will not affect the performance of the system. As a result, the vision system needs to only be able to provide five DOF measurements to the controllers for feedback. The minimum number of cameras required to provide this five DOF information is two. Increasing the number of cameras increases the demand on the FireWire based image acquisition hardware and slows the system, so it is beneficial to keep the number of cameras to a minimum. This is accomplished in the experimental system by placing the cameras so that each can capture three DOF, with one DOF being redundant between them. In this case, the redundant information is the position of the parts in the X direction.

The two cameras required by the system are placed so that each camera views a different, but orthogonal plane as shown in figure 6-1 below.

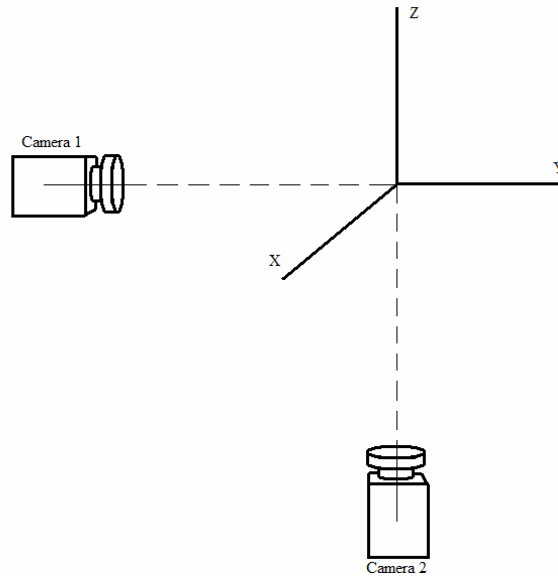


Figure 6-1. Two-camera placement strategy relative to the coordinate system attached to the WAM holding the peg. This camera placement strategy provides the necessary five DOF visual information to the system level controllers.

Now that the desired orientation for the minimum set of cameras has been achieved, the design and programming of the image processing algorithm can begin. The first step to be accomplished by the vision system during image processing is the recognition of the peg and hole in each image. This requires each camera to read an RGB color image and input the data into the system. It was also chosen to limit the resolution of the images produced by the cameras to 320x240 to increase the speed at which the cameras could update the visual information, and also the speed at which the control computer could process it. Once each camera has input its data into the system, the images are run through a simple color filter that enhances one color channel while

filtering out the remaining two unwanted color channels. This method is fast and easily facilitates the color recognition of each part. Accordingly, the object recognition phase has been simplified by using a color coding system that colors the peg with red vinyl adhesive tape and the hole with blue. The filtered data is then passed through a thresholding block that eliminates any pixels that could be false color matches. This block outputs a value of one to an image matrix if the color is a match and a zero if it is not. The output of the thresholding block is a 320x240 binary image that is processed by a blob analysis block that recognizes the large color mass left in the image after filtering. This block approximates the blob with an ellipse and outputs the pixel coordinates of the centroid of the blob, its orientation relative to the positive X axis in the image plane, and the length of its major axis. Using this geometric information, another block calculates the pixel coordinates of the tip of the peg and hole, which are the two points that must be aligned during the approach phase of assembly. Figure 6-2 below shows the input color image along with the two binary images produced by the red and blue filters.

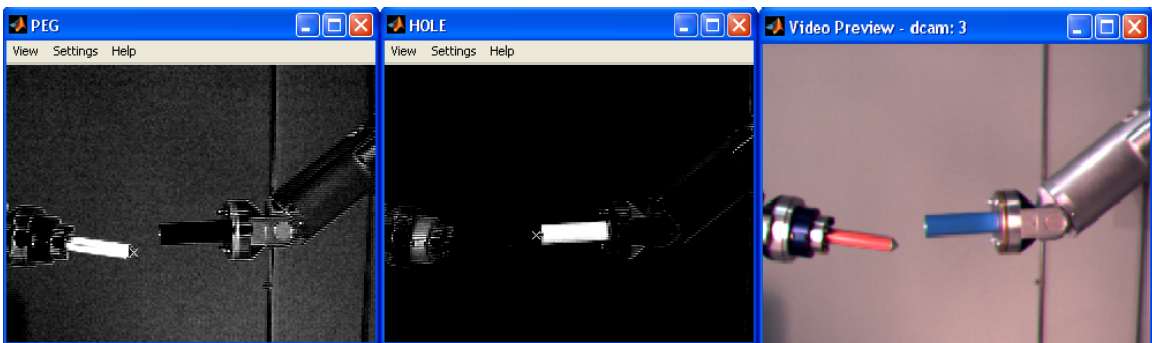


Figure 6-2. Binary images produced by the vision system after color filtering with the calculated pixel coordinate location of the tip of each part marked by an “X”. The figure on the right shows the actual color image that was input into the system by the camera.

This simple vision system is capable of providing all the data needed by the system level controllers at a speed that is notably faster than other vision systems that are based on triangulation. Since the relative position information produced by the vision system is represented in pixel coordinates, as opposed to Cartesian coordinates, a form of visual servoing that is capable of working with pixel based measurements must be adopted. This proved to be quite advantageous as the pixel based system offers sub-millimeter accuracy for the camera placement strategy used in this experimental setup. The visual servoing controller for trajectory compensation developed for this system is explained in the following section. The completed *Simulink* model that intakes image data from two cameras and outputs the $[X, Y, Z, R_y, R_z]$ measurements for the peg and hole is shown in figure 6-3 below.

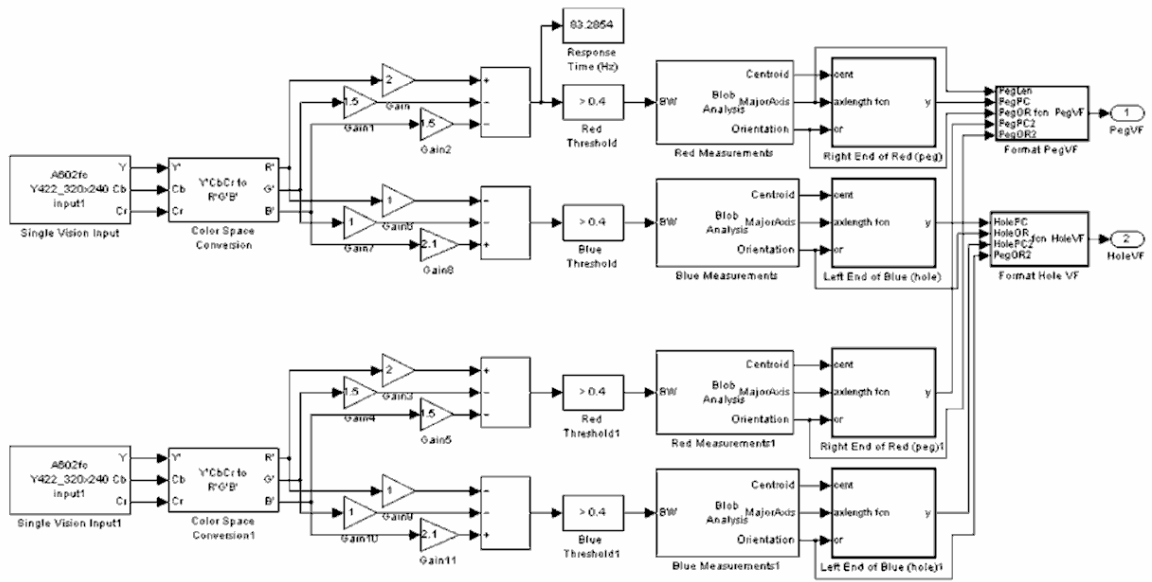


Figure 6-3. *Simulink* model that performs all image acquisition and processing to provide the relevant positional measurements to the control system.

6.2 Visual Trajectory Compensation Controller

The WAM robots are controlled by an impedance controller as described in Chapter 4. This system operates much like a feed forward control loop, as the appropriate joint torques to execute a desired command are calculated by the controller and sent to the robots at each time step of two milliseconds. While this type of control is great for stability and controlling the interaction between the robot and its environment, there is no closed loop system to ensure that the end effector of the WAM accurately follows the desired Cartesian trajectory. Also, impedance control fundamentally imposes a tradeoff between positional accuracy and the compliance of the end effector. For example, a robot running an impedance controller with a very low stiffness struggles to generate enough control force to rigidly follow a trajectory as it stretches away from its base. This is because the stiffness control gain would not be large enough to generate substantial forces to compensate for small errors. The trajectory following problem becomes even more difficult in this system where the stiffnesses are continuously varying, effectively also continuously varying the amount the end effector of the robot droops due to gravity and modeling errors. The compliance afforded to the system can often make up for some of this positional uncertainty in the case of chamfered peg and hole assembly by allowing the peg and hole to correct themselves as a result of contact forces. However, a high level of trajectory following accuracy is beneficial since relatively large initial positional and rotational errors, ε_0 and θ_0 respectively, were shown to be the primary cause of wedging and jamming in the previous chapter.

To boost the positional accuracy of the complete system, visual feedback has been added to provide closed loop behavior to the impedance controller. This could have been

accomplished in a number of ways, but the strategy chosen here was to modify the Cartesian trajectory of each WAM to account for robot droop and align the peg and hole during the approach phase of assembly. This requires the vision system to recognize the relative positions of the tip of the peg and hole as well as their respective rotations. Then, a controller takes the error between the pixel coordinate and rotation measurements and compensates the trajectory input to each WAM, essentially “bumping” the end effector of the robots in the correct direction to completely align them.

The goal of the closed loop system is to eliminate all of the positional error to exactly align the peg and the hole. This implies that the steady-state characteristics of the controller are more important than the transient behavior, assuming that the controller responds with reasonable speed. For this reason, two types of controllers were considered: PID and Finite State Machine (FSM). Though both controllers will produce similar results, they work in fundamentally different ways. The PID controller accepts the desired trajectory input and pixel coordinate error signal and computes a new trajectory to send to the WAMs on the fly to achieve the desired trajectory. However, the FSM builds and continuously modifies a cumulative six DOF compensation vector that is added to each desired six DOF trajectory input as it is sent to the impedance controller to achieve the desired trajectory. Since the peg typically only travels a short distance along a straight line and the hole is held still during assembly, the compensation vector for each robot becomes relatively constant as the controller runs. This is because the vector is essentially compensating for the robot’s kinematic modeling error that is due to small uncertainties in its mass and inertia properties. These modeling errors are also constant for small movements.

The basic closed loop structure of the trajectory compensation system is the same no matter which type of compensation controller is implemented. The block diagram representing the closed loop control system is shown in figure 6-4 below. In this figure, $A(s)$ represents impedance controller of the WAM holding the peg while $B(s)$ represents the impedance controller of the WAM holding the hole. These two systems essentially interact to form their own closed loop system that is governed by the transfer function of the spring-mass-damper model found in section 5.2. The vision controller must precede this system to intercept and modify the incoming desired trajectory data to compensate for the positional errors of the system. The error signal is continually generated at 80Hz from the vision system, as opposed to other forms of time delayed sensors, so there is no direct feedback from the physical system's output.

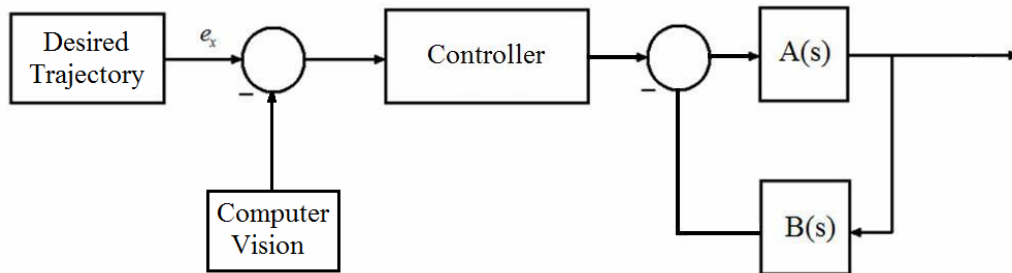


Figure 6-4. Block diagram showing the relation of the trajectory compensation system to the impedance control system. $A(s)$ represents the output motion of the peg and $B(s)$ represents the reaction to the movement caused by contact with the hole.

The first type of controller considered for use was the PID, or proportional-plus-integral-plus-derivative, controller. This type of controller was chosen because it offers very good transient and steady-state tracking behavior due to its derivative and integral actions, respectively. Using the transfer function of the spring-mass-damper model from

section 5.2 as the plant, the *Simulink* block diagram shown in figure 6-5 was created to model the behavior of the PID controller in response to both a step and sinusoidal input. The PID controller was designed using the *Matlab control system design toolbox* and tuned for optimum performance with respect to steady-state error, stability, and control “chatter.” The performance of this system is shown and compared to that of the FSM controller in the following paragraphs.

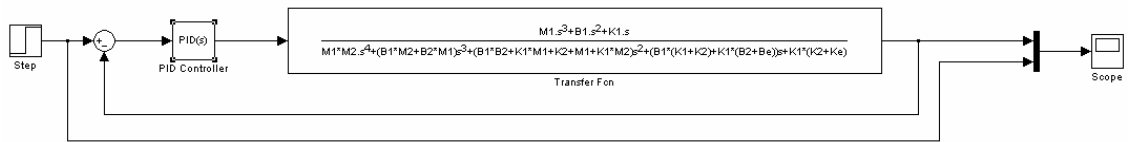


Figure 6-5. *Simulink* block diagram used to simulate the performance of the PID compensation controller in response to a step input. The transfer function representing the behavior of the coupled system was derived in section 5.2.

The second type of controller considered for the visual feedback compensation loop is fundamentally different than the first. The FSM controller operates by accepting input error data, classifying it based on magnitude criteria, then transitioning the system into the appropriate state to add or remove compensation from the system, at which point the controller returns to its initial state to accept more data. The FSM designed for this system is shown in state diagram in figure 6-6. In this FSM, t is the time step of the model, t_{max} is the total time length of the robot’s planned trajectory, T is the running standard deviation of the joint torque values, and cth is the contact threshold, which identifies how much the joint torque standard deviation should change to signify that the assembly process has been completed.

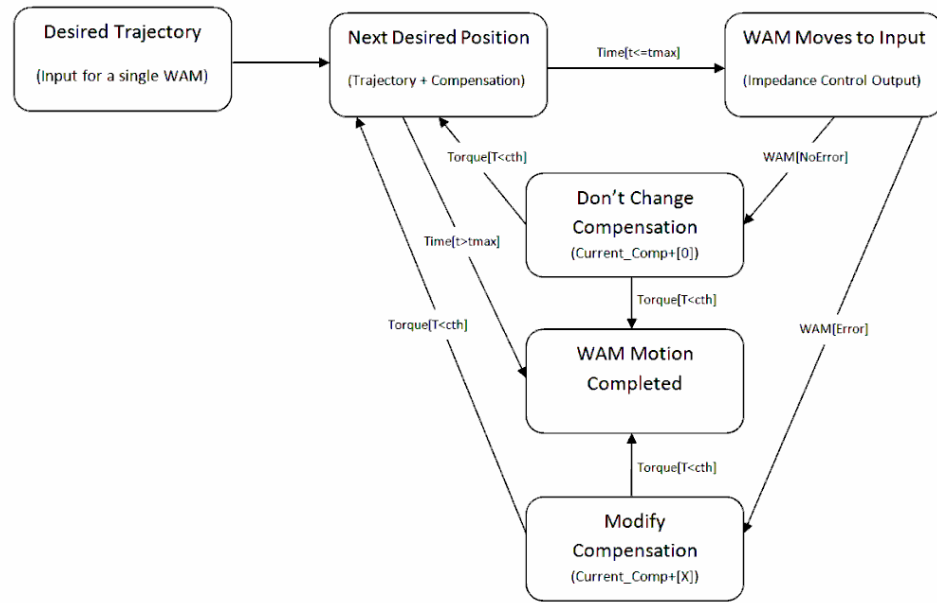


Figure 6-6. State diagram showing the logic and transitions of the visual finite state machine trajectory compensation controller for a single WAM.

This controller starts in the “Next Desired Position” state, in which the next desired Cartesian goal point for the robot is input into the system from the desired trajectory. If the trajectory has not already run longer than it was planned, the goal point is sent to the impedance controller of the WAM. Then the controller executes the command and moves the WAM to the new position. If the vision system detects that there is no error between the alignment of the peg and hole, the system moves to a state where no additional compensation is added to the system, and the next trajectory point is input into the system. If, however, the vision system detects that there is positional error between the peg and the hole, the system instead moves to the “modify compensation” state. In this state, each element of the system’s continuously modified six DOF compensation vector, which is initially set to be a zero vector, is either increased or decreased to correct the system’s error. The FSM model of this compensation block is

shown in figure 6-7. This state essentially classifies the error as greater than or less than several error threshold values, eth , and increases or decreases the compensation vector a fixed amount that is proportional to the size “class” of the error. This compensation vector is then added to the next desired goal point that is input to the impedance controller to compensate for the errors present in the previous step.

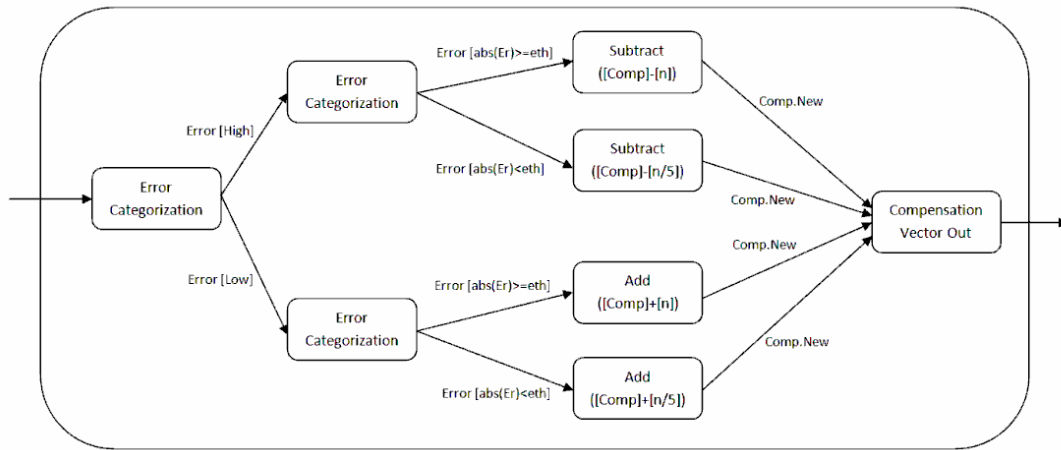


Figure 6-7. State diagram showing the transitions and logic of the compensation vector modification block.

As the WAM is following the trajectory, it is also writing its joint torque readings to the reflective memory where they are available to the control computer, which keeps a running standard deviation for each joint. The FSM controller will check this data for a sudden spike in the standard deviations, which implies that a joint instantaneously has to work harder than before to follow the trajectory, indicating the peg has contacted the back of the hole and the assembly is complete. The control computer then transitions to another state that instructs both WAMs to remain idle so they do not generate excessive force between the peg and the back of the hole.

Another *Simulink* model was created to test the step and sinusoidal input response performance of the FSM controller. The FSM structure was implemented using an embedded *Matlab* code because it runs slightly faster than the comparable *Matlab Stateflow* models. The completed simulation model is shown in figure 6-8.

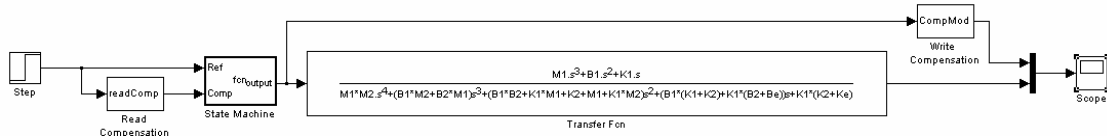


Figure 6-8. *Simulink* model used to simulate the performance of the finite state machine in response to a step input for the transfer function derived in section 5.2.

Now that the simulation models were completed, the performance of each controller could be compared. To run simulations, however, model parameters such as mass and stiffness had to be defined to complete the coupled system's transfer function used for the plant of this simulation. The following example parameters, which correspond to the spring-mass-damper coupled system approximation in figure 5-14, were chosen and substituted into the transfer function.

$$\begin{aligned}
 M_1 &= M_2 = 1 \\
 K_1 &= 600 \\
 K_2 &= K_E = 300 \\
 B_1 &= 4 \\
 B_2 &= 6 \\
 B_E &= 5
 \end{aligned}$$

With the transfer function completed, the simulations could be performed. The first performance test measured the response of each controller to a step input. The results of each controller are shown in figure 6-9.

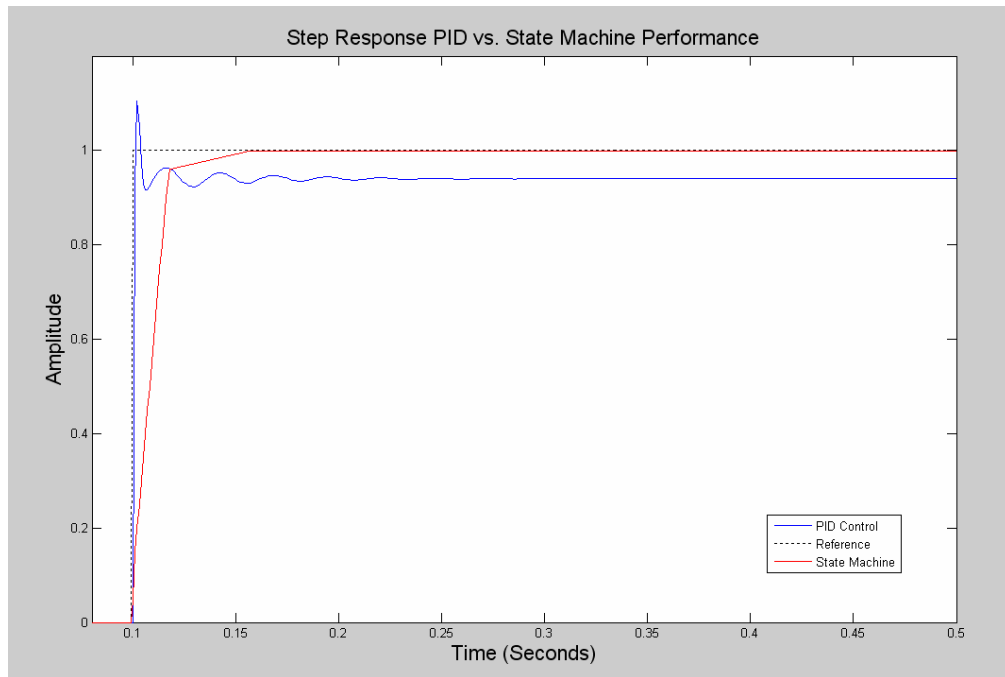


Figure 6-9. Step response of the PID trajectory compensation controller versus the step response of the FSM compensation system.

Both controllers behaved as expected. The PID controller has very good transient response with a 0.00888 second rise time. However it also demonstrates 10.5% overshoot and settles with some steady state error. The FSM on the other hand, essentially operates as a proportional-plus-integral (PI) controller because the cumulative compensation method that continuously adds compensation to the system that is proportional to the error signal essentially implements PI behavior. As a result, the FSM controller has slower rise time due to its lack of derivative action. However, the FSM demonstrates 0%

percent overshoot and no steady state error. Both of these factors, coupled with its reasonable rise time, mean that the FSM controller is the better choice for this system.

The next test demonstrated the ability of each controller to follow a transient input, which was modeled by a sinusoidal input. The results of each controller for this test are shown in figure 6-10 below.

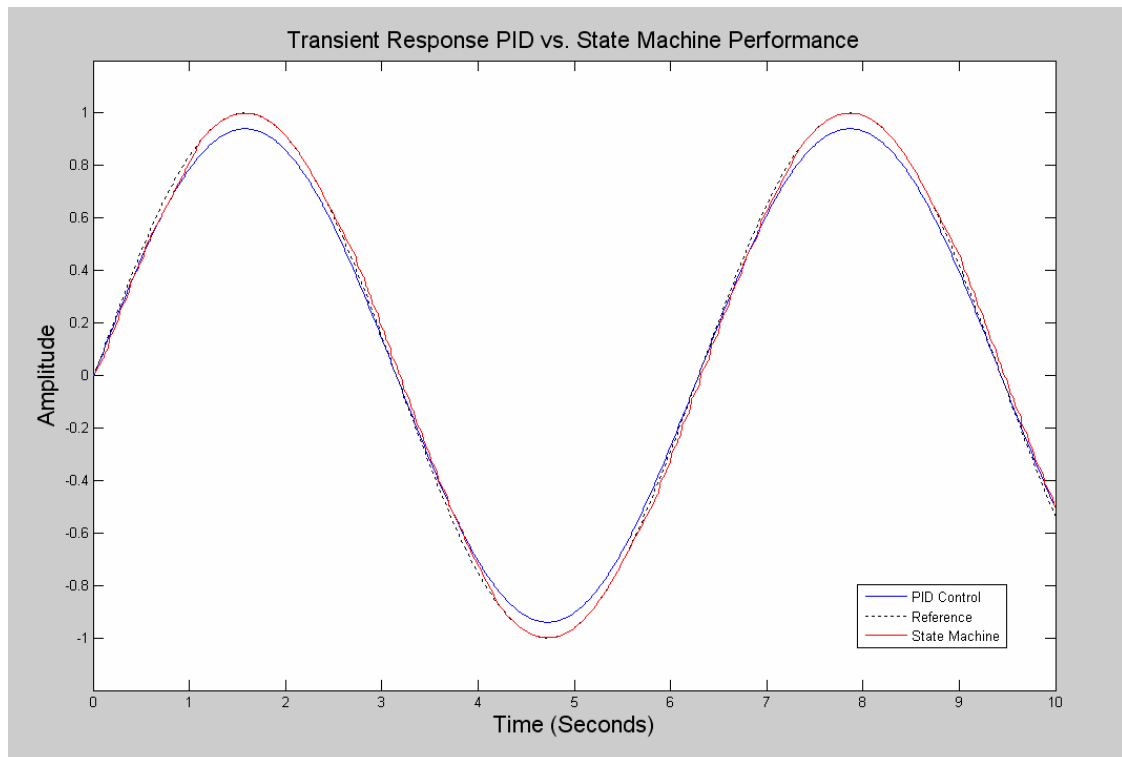


Figure 6-10. Transient trajectory following performance of the PID trajectory compensation controller and FSM compensation system for a sinusoidal input.

The same conclusion can be drawn from this simulation. While the PID controller has a slight advantage in transient response, the FSM controller is the clear winner in steady-state error, which was the most important design goal. Due to these simulations, the FSM controller was the design implemented in the final system. The FSM controller

has another advantage over the PID controller that does not show in these tests. This advantage is the fact that unlike the PID controller, an FSM cannot be unstable. This is due to the strictly bounded compensation allowed by the system's programming. There has been limited research on the stability of state machine controller design. Gore presented two concepts that indicate a stable FSM design in one article. The first stability concept says that changes made to the behavior of a single state in the total state machine should not affect the implementation of the rest of the system. The second concept is similar to the idea of mesh size in numerical computation. This idea states that the state machine should be designed such that every state is used during a run and there are sufficient interfaces to move to each state [60]. In another paper, Tarraf et al. used a mathematical model of the finite state machine to determine the stability of the controller using a linear algorithm that checked the system for three properties. These properties were finite gain input-output stability, external stability, and incremental input-output stability. Each of these requirements focuses on the need of the system to handle inputs consistently and in a bounded way [61]. The FSM presented in this section fulfills all of these requirements, so it is assumed that it will remain stable for all cases. Thus, the stability of the entire system will not depend on any of the visual feedback components of the controller. This greatly simplifies the optimization and design problem by removing variables from the system.

One final test was run to physically prove the benefits of adding the visual feedback loop to the impedance controller. The WAM holding the peg was commanded to move the tip of the peg to a height of 158 millimeters above its base. The hole end effector of the other WAM was placed such that its center was exactly at a height equal to

the target 158 millimeters, but located about ten centimeters in the positive X direction away from the peg's starting position. A horizontal trajectory was then sent to the WAM to command it to move towards the hole. While the WAM was moving, it also output a structure containing its actual trajectory to *Matlab*. If all of the parameters of the impedance controller perfectly modeled the physical WAM system, it would be able to perfectly follow this trajectory and insert the peg into the hole without help from the visual compensation system. However, the impedance controlled system actually does not reach its target height as a result of modeling error and the moderate stiffness gain applied to the impedance controller. This test is most concerned with the ability of the system to compensate for the vertical position errors due to the effects of gravity, since the impedance controller was proven to perform more accurately in the other directions in chapter 4. While the uncompensated peg may only be 1.5 millimeters below its goal height in this test, it was shown in Chapter 5 that small initial errors in alignment between the peg and hole can cause them to wedge almost instantly. Once the visual compensation loop was turned on, the system compensates for the droop in the WAM due to the impedance controller error and the peg is able to very accurately follow its target trajectory and align itself with the hole. The results from this test are shown in figure 6-11.

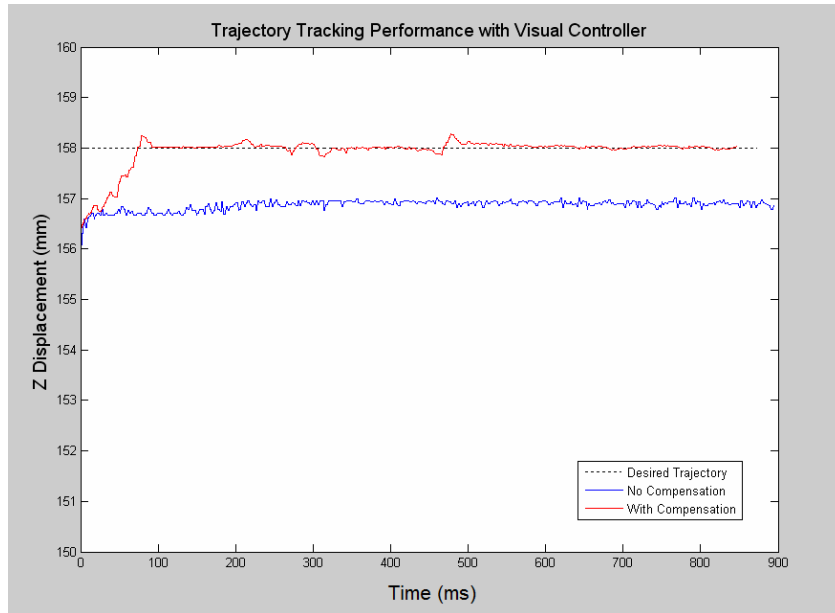


Figure 6-11. Actual trajectory following performance of the WAM in the most difficult vertical direction with and without visual compensation as a function of motion time.

6.3 Variable Compliance Controller

After the vision system has aligned the peg and hole and the compensation vectors have settled at a near constant value, the system will transition to another state that performs the fine motion assembly using a variable compliance controller without visual feedback. During this phase of assembly, the WAM holding the peg is be commanded to move along a short cubic trajectory following the axis of insertion while the WAM holding the hole is compliantly held at a constant position with a constant stiffness. This is because the assembly process is based on the equations derived for a compliantly supported rigid peg being inserted into a rigid hole in Chapter 5. The hole's fixed compliance is used to predictably generate reaction forces to correct the compliantly supported peg's positional error during assembly. The compliance of the peg, however, is varied as it is being inserted into the hole to change how the system

reacts to contact forces. Generally, high lateral stiffness is assigned along the axis of insertion while the stiffness gains in all other directions are left low to allow the parts to passively slide away from the commanded trajectory in the directions normal to the wall of the hole as shown in figure 6-12. This behavior allows the system to accommodate contact forces and avoid jamming. Additionally, the rotational stiffnesses are varied simultaneously with the changes in lateral stiffness to maintain the correct force and moment relationships described in by the jamming diagram in Chapter 5. This is described in more detail in Chapter 7.

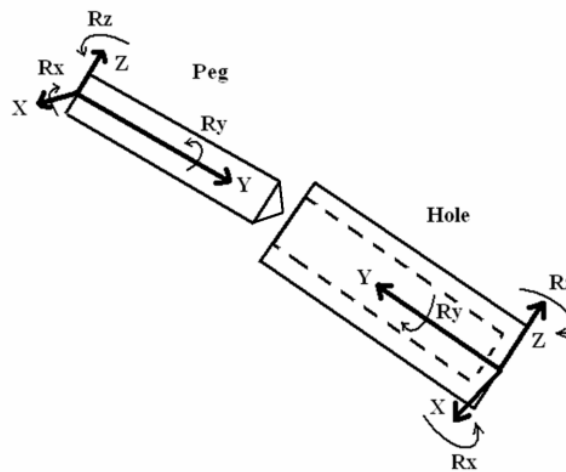


Figure 6-12. Example of the stiffness gains that are set for both the peg and the hole during assembly. The length of the vectors indicates the strength of the stiffness along that direction.

Qualitatively considering the peg and hole insertion problem makes it is easy to see why varying the compliance of the peg will increase the chances of a successful assembly. As a human inserts a peg into a hole, they will naturally allow that peg to follow its own self-corrective path into the hole. For example, if a peg moving with a

moderately stiff compliance comes into contact with the wall of the hole, it naturally wants to “glance” off of the constraint and redirect its tip away from its initial direction of movement to move along the wall and complete the assembly process. In this instant, the stiffness of the peg’s support should decrease to accommodate these reaction forces and allow this motion to take place. However, once the peg has momentarily realigned itself with the hole, it is beneficial to return to the original, higher stiffness to ensure that the peg remains in the control of its support and not that of the hole.

Based on the logic of the above description, the desired goal system must be able to temporarily relax the compliance of the peg as errors build due to misalignment. This requires a system to be designed that can impose this behavior on a WAM. Due to the simple behavior of the desired system, a basic proportional controller has been implemented to actively change the stiffness gains of the impedance controller based on the magnitude of an error signal generated by the peg and hole misalignment. However, there are many options available for the source of this error signal. The original controller design used the vision system to generate an error signal based on the visually measureable rotational misalignment between the peg and hole in each camera frame. However, this turned out to be an unreliable error source due to the success of the FSM visual compensation system. The peg and hole are often aligned so well that the error signal was on the order of thousandths of a radian. Combining such small numerical values with the relatively noisy signal produced by any vision system caused unpredictable compliance control. Combine this issue with the fact that the vision system is about six times slower than the impedance controller and it becomes obvious that a better error source is to be desired. The most accurate and fastest sensors available to the

control system are the joint encoders on each WAM, so it was thought that these sensors would produce the best error signal.

Chapter 4 described the impedance controller's relation between Cartesian position error and output controller force. This is the basis used for the construction of the error signal for the variable compliance controller. Along the axis of insertion, the compliance controller assigns a constant and relatively high stiffness to the peg as explained earlier. This means that as the peg follows its cubic trajectory into the hole along this axis, it should be closely tracking the desired positions. If there is any positional error along the axis of insertion, it will combine with the high stiffness to directly produce large insertion forces to correct the positional error of the tip of the peg. Large insertion forces imply that the peg and hole are on the verge of wedging and jamming since a portion of the WAMs effort is now being stored in the peg and hole in the form of elastic deformation. Increasing the compliance of the system by decreasing stiffness gains in the non-axial directions will allow the internal forces between the peg and hole to translate and realign the parts, causing the insertion force, and its corresponding axial positional error to decrease. Using this method, an error signal can be accurately and quickly produced for the variable compliance controller based on the positional error between the actual position of the WAM and its desired trajectory along the axis of insertion. A block diagram of this controller is shown in figure 6-13. The control law equations that relate displacement error to lateral and rotational stiffness gain change within the "Compute Stiffness Parameters" block are given by equations (7.1) and (7.2). They are derived as a homogeneous part of the optimization process and are presented in section 7.5 of the following chapter.

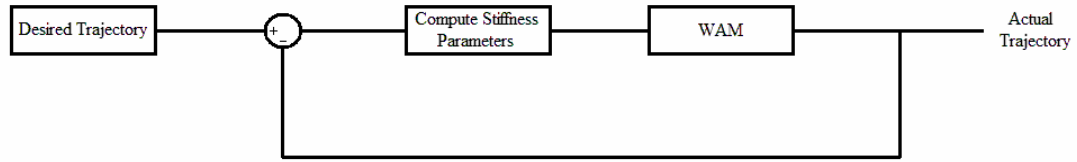


Figure 6-13. Block diagram representation of the proportional variable compliance controller. Changes in compliance are proportional to positional error between the peg's desired and actual positions along the axis of insertion.

Now that the basic control structure is completed, the final task of the design process is to define the optimum stiffness gains for the peg to use as a starting point. Also, the amount the stiffness gains are allowed to decrease must also be derived and programmed into the variable compliance control law. This is important since there is a lower limit to the peg's compliance as described in the design process covered in the following chapter. The *Simulink* model of the complete system-level control structure is shown in figure 6-14. During operation, this control loop compensates for trajectory errors and computes new stiffness parameters at a rate of 80-100Hz.

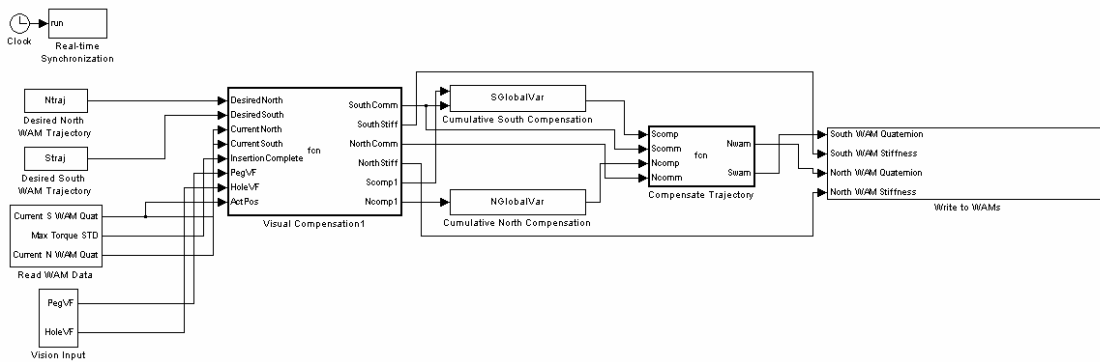


Figure 6-14. Complete *Simulink* model that performs all system-level control computer functions when run.

CHAPTER 7

PARAMETER OPTIMIZATION

In this chapter, the complete system model developed in Chapter 5 is used to optimize the variable impedance control parameters with respect to success, measured by the jamming diagram, and system stability. The range of acceptable stiffness values is also defined to prevent the variable compliance controller from moving the combination of compliance variables to an unacceptable level. The final result of this chapter will be the control law equations that are input into the variable compliance controller to perform the experimental peg and hole assembly task.

7.1 Applying the Stability Criteria

Now that the structure of the cooperative robotic insertion system and the theoretical model to predict its behavior had been completed, the impedance controller parameters, which are the only variables in the system, could be selected to impose the desired behavior on the system. The first step in the design process was the consideration of the constraints imposed on the stiffness and damping impedance controller gains by the coupled system stability analysis presented in section 5.2. This was accomplished by plotting equations (5.57) through (5.62) for the physical parameters of the known experimental system. These physical parameters include the effective mass of the end effector of each robot, the effective stiffness and damping of the uncontrolled robot mechanics plus the controlled impedance controller output force supporting the hole end effector, and the amount of uncontrolled stiffness and damping associated with the

insertion robot's mechanics. The numerical values of these parameters are shown below. M_1 and M_2 were chosen based on the actual mass of the two end effectors. K_2 and B_2 represent the total output of the impedance controller of the passive robot, which is set to have medium compliance and remain constant. It is assumed that the impedance controller force output of the passive robot is much larger than the effects of its mechanical stiffness and damping. So the values K_2 and B_2 are simply the impedance controller stiffness and damping gains. Last, K_1 was chosen to mirror the stiffness of the passive robot on which the peg is acting since this stiffness most likely dominates any stiffness inherited by insertion WAM's hardware. B_1 was chosen to be the minimum value since there is little damping contributed to the system by hardware and friction in comparison to the effects of the impedance controller output.

$$\begin{array}{lll}
 Mass_{peg} = M_1 = 0.5kg & K_1 = 400 & B_1 = 1 \\
 Mass_{hole} = M_2 = 0.2kg & K_2 = 400 & B_2 = 5
 \end{array}$$

Substitution of these values into the coupled stability equations (5.57) through (5.62) and plotting results in figure 7-1. This figure defines a clear region of successful stiffness and damping gains for the "peg" to guarantee a stable system when the two robots are in contact with each other. Notice, two additional constraints were added to this plot. These lines represent the minimum reasonable values of stiffness and damping for the specific WAM impedance control systems developed in this thesis. As shown earlier, choosing a stiffness gain below 100 would produce unreasonably poor trajectory

following performance. Also, a negative damping gain is not a logical possibility for impedance control and would lead to terminal instability, so the minimum damping limit is set at 0.

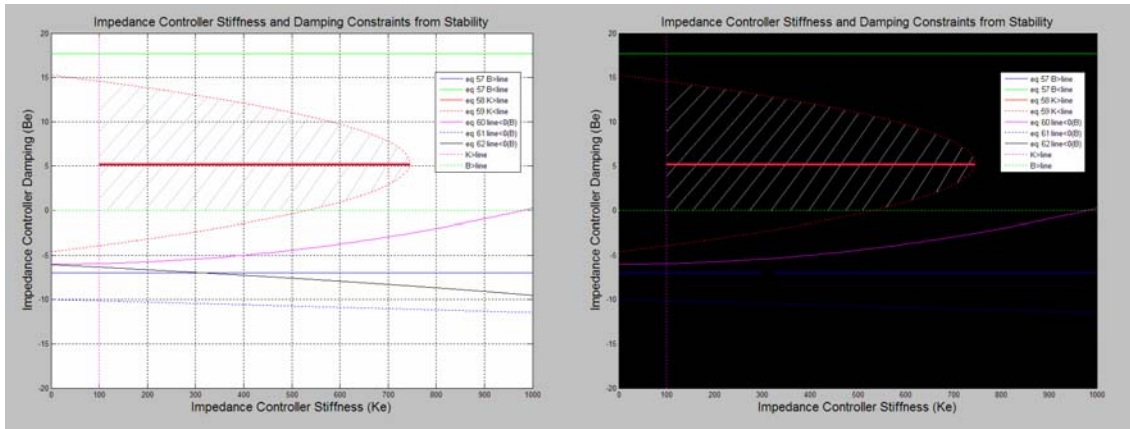


Figure 7-1. Constraints imposed on the stiffness and damping parameters of the experimental system by the coupled stability criteria. The plot on the left is the output from *Matlab*, while the plot on the right has been colored differently to better show the stiffness and damping boundaries. The bold, red, horizontal line represents to range of acceptable stiffness values that correspond to the damping ratio chosen during the design process.

The plot on the left is the output from the *Matlab* script that plots the constraints for the given input values. The plot on the right is the same plot, but with a black background that attempts to make the boundaries more visible. In this plot, the shaded region represents the acceptable combinations stiffness and damping values that satisfy the constraints of coupled system stability. Analyzing this figure allows specific stiffness and damping values to be considered for application in the target impedance controller. While stiffness gains can be altered continuously throughout a single robot motion without affecting the expected performance of the WAM, changing the damping gains while the WAM is in motion can produce very unpredictable behavior. This is why the

design process will instead choose the best damping gain and leave it constant throughout the insertion trajectory. Looking at the plot in figure 7-1 enables the designer to see that choosing a damping gain of 5 is the best choice for two reasons. First, it is located in the middle of the acceptable damping values, so it is less likely to result in an under-damped or over-damped system. Second, this damping gain corresponds to the greatest range of acceptable stiffness gains as represented by the thick red horizontal line in figure 7-1, resulting in the greatest freedom of choice over this parameter. Thus, from this coupled stability analysis, the following conclusions can be drawn. Note that the maximum allowable stiffness value was rounded down to 700 to keep the system from operating on the edge of stability.

$$B_E = 5$$

$$100 \leq K_E \leq 700$$

7.2 System Assumptions and Dimensions

Now that the damping gain for the insertion WAM's impedance controller and a range of acceptable stiffness gains has been established, the next step is to find the optimum single stiffness gain for the insertion WAM with respect to the success of the peg and hole assembly task. This is accomplished using the peg and hole assembly analysis performed in section 5.1. This analysis of the experimental peg and hole system will define the optimum stiffness gains as well as the optimum location of the compliance center of the peg, which is the final design parameter. Keep in mind that the impedance

controller stiffness gain, K_E , is a six-by-one vector representing the six DOF stiffness of the system in the following format.

$$K_E = [K_X \ K_Y \ K_Z \ R_x \ R_y \ R_z]'$$

The two-dimensional peg and hole analysis allows the three pairs of coupled lateral and rotational stiffnesses to be defined by analyzing different planes of movement. To find the complete stiffness vector, two assumptions need to be made. First, it is known that the insertion is occurring horizontally in the experimental insertion. This implies that K_X is the longitudinal stiffness, which must be kept significantly stiffer than the other stiffness directions to assure that the peg is always moving towards completion. For this reason, K_X was set to be set near the maximum stiffness allowed by the stability criteria and remain constant as shown below.

$$K_X = 700$$

Also, due to the axisymmetric properties of the cylindrical peg used in this experiment, the rotation in the “roll” direction has no effect on the performance of the system since no amount of rotation in this direction will make a difference in the system’s geometry. Thus, this stiffness should also be set to a constant. However, it will be set to a low stiffness so that it will not provide any resistance to the necessary rotations in the other two directions. Thus, R_x was defined by the following.

$$R_x = 1$$

Also as a result of the axisymmetric geometry of the experimental system, it can be assumed that the other two sets of coupled stiffnesses, (K_y, R_y) and (K_z, R_z) , can be treated equally since they define the lateral and rotational stiffnesses on two different planes, and the axisymmetric nature of the problem says that any two planes about the longitudinal axis of the peg are equal. Thus the following assumptions can be made for the two-dimensional peg and hole analysis.

$$K_y = K_z = K_x$$

Where K_x is the lateral stiffness in the two-dimensional analysis and not K_x , the stiffness applied along the Cartesian X direction.

$$R_y = R_z = K_\theta$$

As explained in Chapter 5, chamfer crossing and one-point contact are heavily dependent on the initial conditions of the peg's positional error with respect to the hole. Since the insertion system used in this thesis is constantly running a controller that actively aligns the peg and hole with essentially no measurable error, the effects of chamfer crossing and one-point contact are negligible. For the same reason, the system easily satisfies the initial requirements of the wedging diagram, so it is also not a concern for the controller gain design process. Accordingly, the two-dimensional analysis used to define the controller stiffness gains will be governed exclusively by the more critical two-point contact equations. Two-point contact is the most problematic stage of assembly

since jamming and wedging can only occur during this stage. Thus, the stiffness parameters of the insertion WAM will be optimized with respect to equations (5.42)-(5.45) as they are related through the jamming diagram shown in figure 5-8.

Before this analysis can begin, the physical parameters of the peg and hole system must be defined and plugged into the governing equations. The first and most important parameter needed is the coefficient of friction between the peg and the hole. The peg is constructed from machined aluminum, but it is covered with colored vinyl adhesive tape that has been applied to facilitate computer vision recognition. The inside of the hole it is being inserted into is constructed from machined aluminum and has no covering. To measure the actual coefficient of friction between the two surfaces, the force sensor attached to the peg was oriented such that the “Z” measurement axis was perfectly horizontal and the “X” measurement axis was perfectly vertical in the normal plane. Starting with the peg and hole in contact and at rest, a constant force was applied vertically downward and a horizontal force was slowly added until the peg had finished sliding along the hole. Using the readings from the force sensor, the coefficient of friction was estimated using the following equation.

$$\mu = \frac{F_{z_{\max}}}{F_{x_{\text{const}}}} = 0.45$$

The maximum coefficient of friction measured during the experiment was used to design the system to the worst case parameters. Since all contact forces generated by peg and hole contact are friction limited, designing to the highest friction coefficient possible

ensures that the system will be successful for all possible contact forces. This is because less friction corresponds to smaller contact forces that are easier to accommodate than larger forces. Also, it is worth mentioning that this coefficient is quite reasonable and corresponds to many tabulated values of friction between aluminum and plastic. Similarly, the values of initial lateral and rotational error between the peg and hole had to be experimentally defined. Due to the peg and hole alignment controller, these values are typically near zero. However, to account for the worst case scenario with the greatest amount of misalignment, the alignment controller was run ten times. The experimental controller also kept running maximum measurements of the lateral and rotational error between the peg and the hole. After the experiments were finished, the maximum errors allowed by the system over ten runs were the following values.

$$\theta_0 = 0.04 \text{ rad}$$

$$\varepsilon_0 = 0.0032 \text{ meters}$$

The final parameters needed for the peg and hole analysis are the physical dimensions of the peg and hole. These dimensions were simply measured from the physical parts and are shown in figure 7-2.

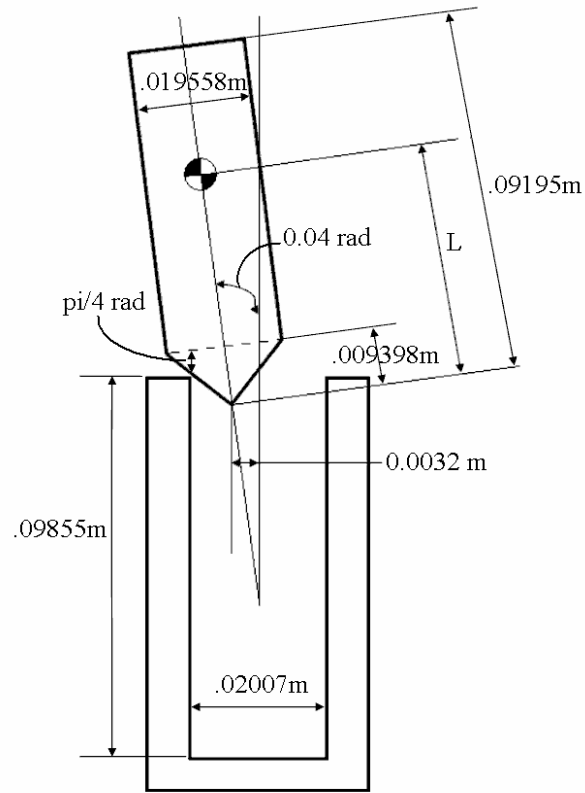


Figure 7-2. Actual peg and hole dimensions from the hardware used during the physical insertion experiments.

7.3 Introduction to *modeFrontier*

ModeFrontier is an optimization software package that allows the user to define visual workflow models that represent input variables, system equations, and output values for a given system. The software is able to substitute different combinations of input variables into the system equations, and find those that optimize the output values with respect to user defined goals. *ModeFrontier* was chosen to perform the optimization described in the introduction paragraph of this chapter because of two key features. The first is *modeFrontier's* ability to solve multi-objective optimization problems. As presented in section 7.4, the optimization task required for this thesis will require three

variables to be optimized with respect to two different goals. This type of optimization problem is difficult because there is often no single optimum solution with respect to both goals, meaning that a set of parameters that optimize one goal may produce poor results with respect to the other. *ModeFrontier* was designed to handle these situations by outputting all solutions that fall on the Pareto frontier, or a series of solutions that cannot be optimized with respect to one goal any further without hurting the system with respect to the other goal. This allows the designer to make an informed choice with respect to the trade-offs between multiple candidate answers [63].

The second desirable feature of *modeFrontier* is its ability to find robust solutions, or those with low sensitivity to changes in the input parameters [63]. This is necessary because the optimized variables in this chapter are the impedance control parameters that will be input into the variable compliance controller shown in figure 6-13 to achieve the optimum conditions to avoid jamming. This controller will actively increase or decrease the impedance control parameters from the optimum values. Stable solutions will ensure that small changes in parameters will not cause large system changes with respect to the optimization goal behavior, or the jamming diagram in this case. It should also be noted that the *modeFrontier* analysis presented in section 7.4 is performed offline and on a computer that is isolated from the rest of the system hardware. Its results are a continuation of the system modeling process from Chapter 5, as *modeFrontier* provides a reliable method to combine all the information available to describe the system and provide optimum values of the impedance controller parameters K_x , K_θ and L with respect to specific design goals. These optimum values are used to partially define the control equations (7.1) and (7.2) that are programmed into the

variable compliance controller that runs on the system control computer during assembly. This is why the *modeFrontier* computer is not included in the system hardware diagram shown in figure 3-1.

7.4 Finding Optimum Parameters with *ModeFrontier*

Now that all the information needed to solve the equations for F_x , F_z , and M applied to the peg during assembly has been defined, the only remaining variables in the system are the impedance controller parameters K_x , K_θ and L . Since the jamming diagram is a function of the forces applied to the peg, and the forces are a function of the impedance controller variables, the governing equations are essentially a set of equations that relate the impedance controller parameters to the likelihood of the system jamming during insertion. The jamming diagram implies that the peg and hole are least likely to jam when the applied force ratios $\frac{M}{rF_z}$ and $\frac{F_x}{F_z}$ are closest to zero and near the center of the diagram. Defining impedance control parameters that put the peg and hole system in the center of the jamming diagram and furthest away from its boundaries was the design goal of this section. Thus, the optimized impedance controller parameters are those that minimize the absolute values of the ratios $\frac{M}{rF_z}$ and $\frac{F_x}{F_z}$. Since the system of equations is clearly defined with three variables that can be varied independently to achieve two minimization goals, *modeFrontier* was easily implemented to find the impedance controller parameters that are optimized with respect to avoiding jamming during two-point contact.

As explained in section 7.3, *modeFrontier* is a software package that allows the user to build a visual “workflow” model of a series of equations to find a solution that has been optimized with respect to the desired goals. The workflow model used to optimize the impedance controller variables is shown in figure 7-3 below.

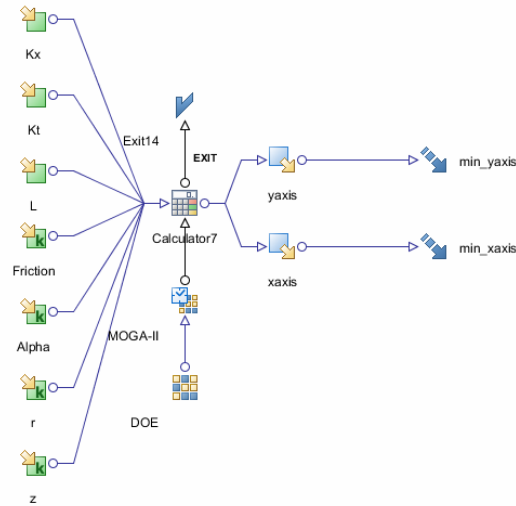


Figure 7-3. *ModeFrontier* workflow model representation of the two-point contact jamming diagram used for parameter optimization.

In this model, the green icons along the left side of the model represent the parameters that are input into the system. The first three icons, K_x , K_t , and L represent the three impedance control variables that are to be optimized. Since their exact values are unknown, they are entered into the model as ranges of possible values. *ModeFrontier* then simultaneously varies them within their given ranges to find the combination that best meets the system optimization goals. The range of each optimization variable is shown below. The range of K_x was defined using the coupled stability analysis. The range of the rotational stiffness, $K_t = K_\theta$, is defined as all the possible rotational

stiffnesses that are allowed by the controller as defined in Chapter 4. Finally, the range of L , the position of the compliance center on the peg, is defined to not exceed the length of the peg.

$$100 \leq K_x \leq 700$$

$$2.75 \leq K_\theta \leq 7.80$$

$$0 \leq L \leq 0.1016$$

The remaining input variables, such as friction and insertion depth, are held constant and they are marked with a “K” on their icons. In section 5.1, it was explained that two-point contact can only begin beyond a specific insertion depth, which can be calculated as shown below.

$$l_{start\ 2-point} = \frac{c2R}{\theta_0} = \frac{0.000508m}{0.04} \approx 0.0127meters$$

Since jamming becomes less likely the farther the peg is inserted into the hole, the shallowest possible insertion depth for two-point contact was chosen for optimization to again assume the worst case conditions during assembly. All of these inputs are fed into a calculator node that calculates the ratios $\frac{M}{rF_z}$ and $\frac{F_x}{F_z}$ based on the input variables using equations (5.42) through (5.45). These ratios are output from the calculator node under

the names “yaxis” and “xaxis” referring to their relation to the jamming diagram. *ModeFrontier* is then set to run the MOGA-II (Multi-Objective Genetic Algorithm) optimization algorithm, which essentially tries all combinations of the variables necessary to find the combination that best meets the optimization goals, which are to minimize the absolute values of $\frac{M}{rF_z}$ and $\frac{F_x}{F_z}$. Running the optimization model takes about five minutes and produces data from around one-hundred different combinations of variables. For this case, there was only a small Pareto frontier as the combinations of variables that minimized one goal often minimized the other. This made it easy to choose the best combination of variables with respect to both goals. If this optimum combination is opened in *modeFrontier*, the spider chart in figure 7-4 is displayed.

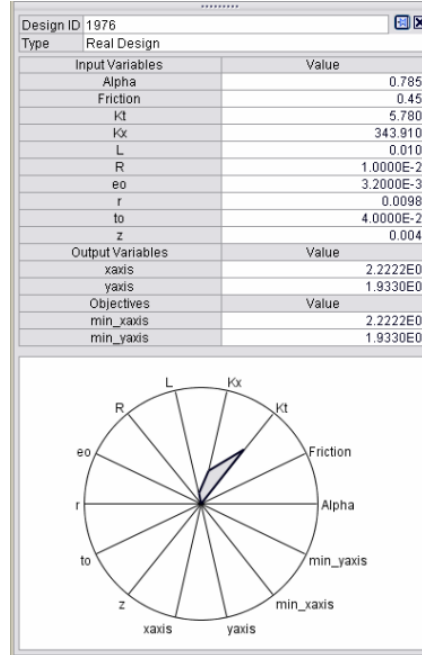


Figure 7-4. Spider chart representation of the three optimal parameter settings for the peg’s impedance controller with respect to jamming avoidance using the ranges of variables that also satisfy the coupled stability constraints.

Looking at the spider chart reveals the optimum impedance controller parameters to be the following.

$$K_{x_{optimum}} \approx 344 \frac{N}{m} \quad K_{\theta_{optimum}} = 5.78 \frac{N-m}{radian} \quad L_{optimum} = 0.01 \text{ meters}$$

In addition to the optimum parameters, *modeFrontier* can also provide the designer with more intuitive information based on the results from the different experimental trials the software had to run to find the single solution. This is best explained through the use of a parallel coordinates plot that can be generated for the optimization process. What this specialized visualization does is plot a single line for each experimental trial that was run by *modeFrontier* during optimization. Each line connects the specific values of the three variables of interest that were chosen for that run and the resulting “xaxis” and “yaxis” values they produced. The parallel coordinates figure showing all 100 runs of the optimization process is shown in figure 7-5.

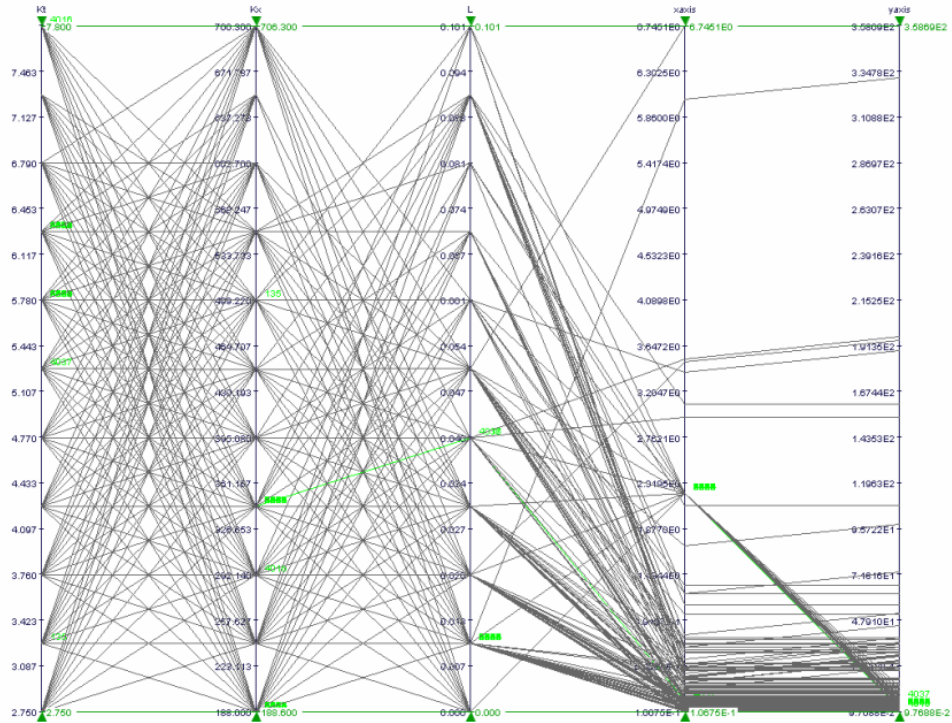


Figure 7-5. Complete parallel coordinates representation of all 100 optimization experiments.

While this all-inclusive plot may be too crowded to make sense of, the results can be filtered to only show the runs that are meaningful to the understanding of the optimum solutions. For example, the rightmost two columns represent the *xaxis* and *yaxis* variables. Since the combinations of variables that produce small values for these two results are all that the designer would be interested in, the results that did not meet this goal can be filtered out of the plot. This produces the plot shown in figure 7-6.

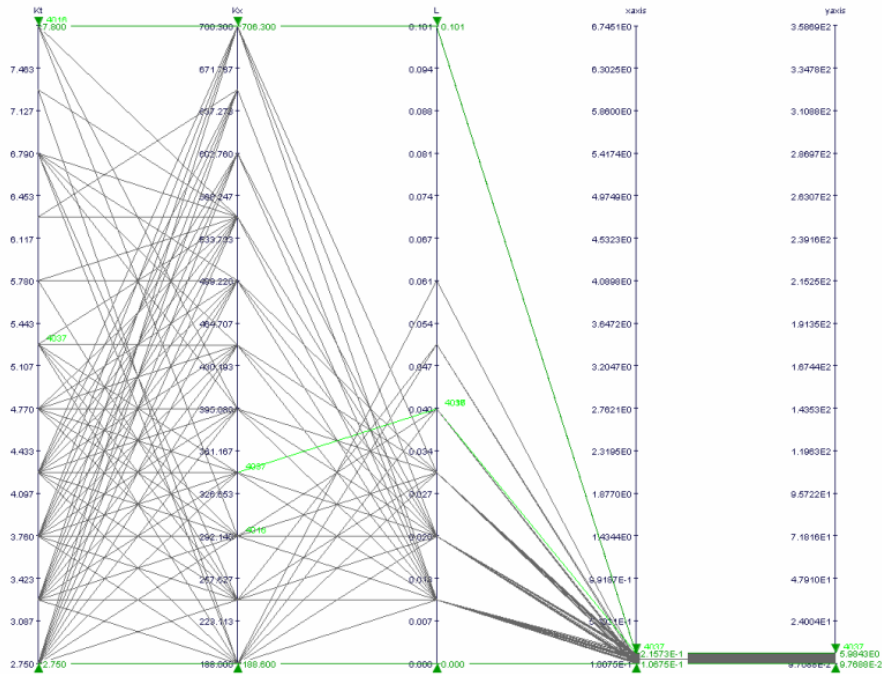


Figure 7-6. Filtered parallel coordinates plot that only shows the experiments that produced desirable results with respect to the system’s position on the jamming diagram.

From this plot, it is obvious that most of the successful combinations of variables included a small value for L , which is shown in the center column. It is commonly cited in literature, and explained earlier in this thesis, that the best place to locate the compliance center is at the tip of the peg, or when $L = 0$, because it decouples the lateral and rotational movement of the peg as a result of contact forces. The results from *modeFrontier* also prove this hypothesis. Taking this into consideration, all of the trials that used anything but the smallest values for L can be filtered out of the plot since these combinations will not be relevant to the final parameters chosen to program the peg’s impedance controller. This filtered plot is shown in figure 7-7.

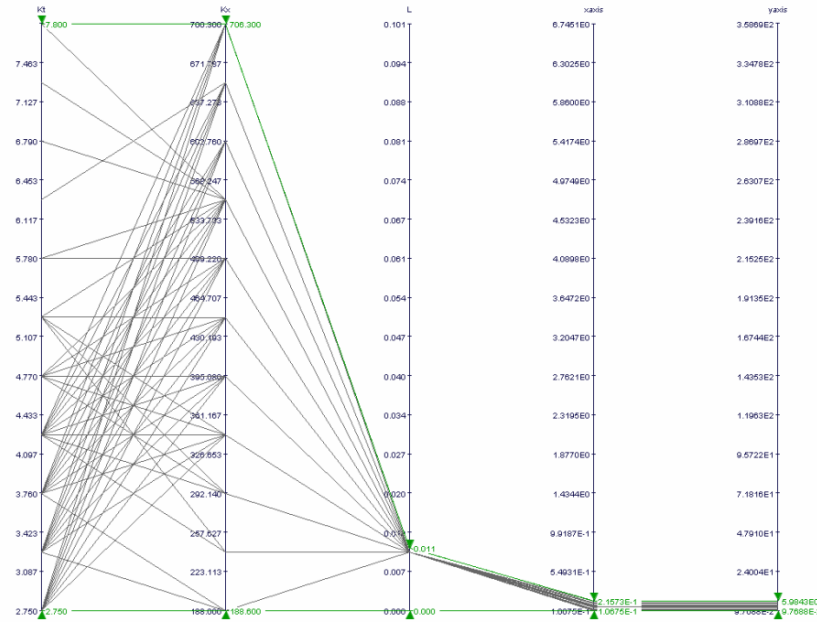


Figure 7-7. Parallel coordinates plot that has been further filtered to only show the experiments that utilized the desired compliance center location near the tip of the peg.

The two leftmost columns are left to analyze. These columns represent the rotational (far left) and lateral stiffness values for the peg. Looking at the slopes of the lines connecting these two columns reveals that there are two general trends for successful parameter definition. One trend shows the successful combination of low rotational stiffness and high lateral stiffness as shown by the large number of lines with steep, positive slopes. The second trend shows that combinations of intermediate rotational and lateral stiffnesses are also successful as shown by the number of horizontal or near-horizontal lines connecting these columns. Since the goal of the peg and hole system designed in this thesis was to create a compliant system, as opposed to a stiff, position controlled system, it would also make sense to filter out the combinations of variables that included high stiffness variables and follow the second trend. After applying this filter, the result is the final parallel coordinates plot is shown in figure 7-8.

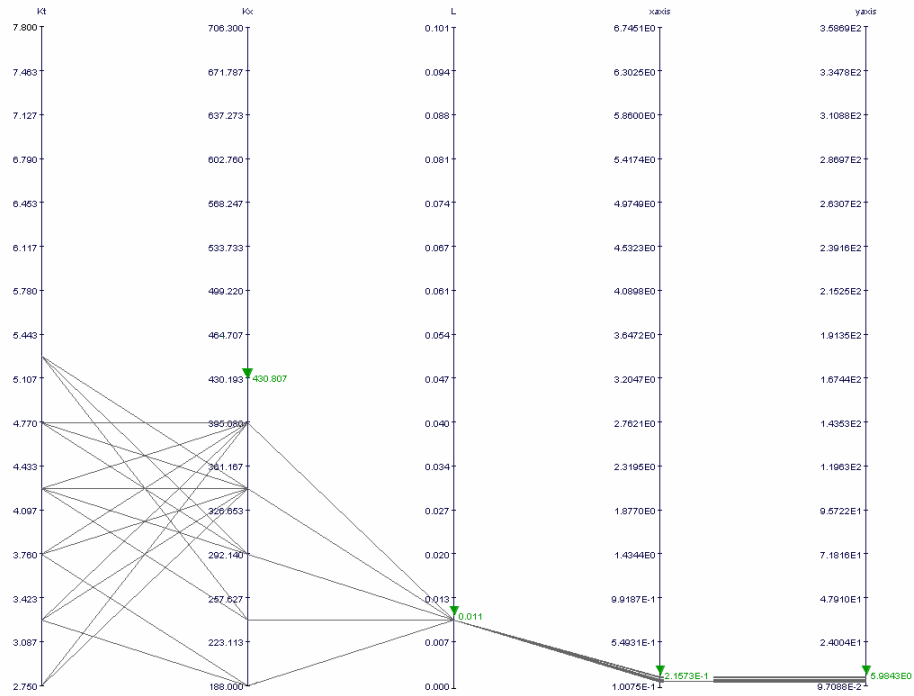


Figure 7-8. Filtered parallel coordinates plot of the experiments that obtained good results using relatively low stiffness parameters.

Figure 7-8 shows that combinations of low and intermediate stiffness values produce the best results while the compliance center is located near the tip of the peg and the rotational and lateral stiffness gains are held in constant proportion. This generalization is supported by the intermediate values of the overall optimum solution presented on the spider chart earlier, and gives the following strategy for varying the stiffness gains during assembly. From *modeFrontier*, the optimum stiffness settings are known. It is also known that if the rotational and lateral stiffness settings need to be varied as the peg encounters near-jamming forces, they should be decreased simultaneously and proportionally. This is shown by the varying heights of the horizontal and near-horizontal lines relating the different successful combinations of lateral and rotational stiffness gains in the parallel coordinates plot.

The last piece of information needed to completely program the variable compliance controller is how far the stiffness gains can be decreased before situations arise in which the jamming diagram is no longer satisfied. *ModeFrontier* only found the optimum values and provided insight into the interaction of the optimization variables, but it did not directly tell us which combinations of variables would be likely to fail. This design problem is considered in the following section.

Section 7.5 Defining Acceptable Compliance Ranges

To obtain this last piece of information, another impedance controller stiffness parameter test needed to be conducted. To perform this test, a *Matlab* script was written to intake all of the possible input constant values and ranges entered into the *modeFrontier* calculator. Then, the script tests every possible combination of lateral and rotational stiffness gains against the jamming diagram for the case where the compliance center is located at the tip of the peg. The script starts with a matrix of zeros that represents each combination of lateral and rotational stiffness by a constant position in the matrix. If the jamming diagram shows that the combination successfully avoids jamming, the script adds a value of one to the position in the matrix that represents that specific combination. If the combination fails, nothing is added to the position. This analysis is then repeated for every possible insertion depth. It is worth noting that this script also includes the equations for F_x , F_z , and F_m during chamfer crossing and one-point contact since they are the applicable equations for the beginning of the insertion. The script automatically switches its modeling equations from chamfer crossing to one-point contact after the insertion depth is greater than the chamfer height. It then switches

from one-point contact to two-point contact at the transition point found earlier. Thus, this script tests the system for jamming for all possible contact cases and all insertion depths. The output is a matrix where higher values are assigned to the stiffness combinations that succeeded most often, and low values indicate stiffness combinations that failed for different contact conditions. A contour map of this matrix can then be plotted to give a visual representation of stiffness ranges that are acceptable for use in the peg's impedance controller to always avoid jamming. The resulting plot is shown in the figure 7-9 below.

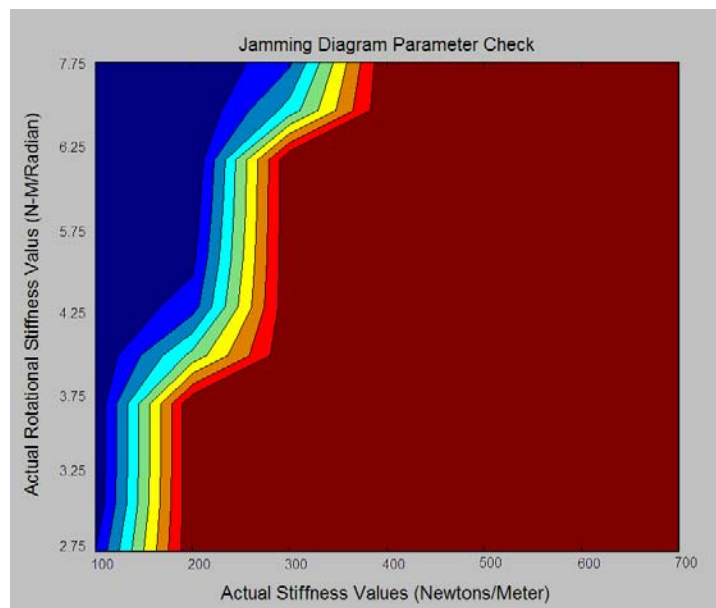


Figure 7-9. Contour plot output by the jamming diagram parameter checking script that tests all possible combinations of stable stiffness and damping parameters for successful assembly through jamming avoidance. Points that are blue (left-most) correspond to combinations of parameters that are never successful while points that are dark red (right-most) correspond to parameter combinations that are always successful.

A lot can be learned from this plot. The first insight is that combinations of high rotational stiffness and low lateral stiffness do not work for peg and hole insertion. The

second thing to notice is the almost linear “ridge” between the combinations that always work and those that never work. This supports the analysis from *modeFrontier* that emphasized the need for rotational and lateral stiffness to be varied simultaneously and in constant proportion, instead of independently, to maintain a successful combination of the two parameters. From this plot, it is reasonable to guess that the optimum proportion in which to vary these stiffness parameters follows the “slope” of the ridge in the contour plot, as this would produce the most compliant combinations of variables that still satisfy the jamming diagram boundaries for all contact cases. This is demonstrated in figure 7-10, which shows the above contour plot that has been labeled to illustrate the final stiffness variation strategy.

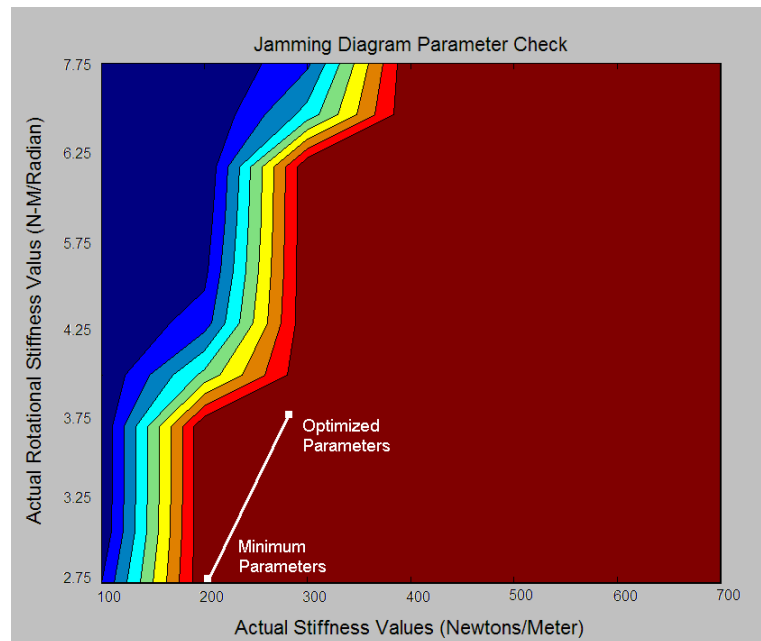


Figure 7-10. A copy of the contour plot from figure 7-9 that has been labeled with the optimized parameters found with *modeFrontier*, the minimum parameters allowed by the jamming diagram, and the range of desirable parameter combinations that the variable compliance controller can choose from while varying the compliance of the system.

In figure 7-10, the position of the optimized rotational and lateral stiffness combination that was produced by *modeFrontier* has been labeled. This point lies near the ridge in the contour plot. This is expected since this area represents the most compliant parameter combinations available that always satisfy the boundaries of the jamming diagram. Following this example, any variations made to the stiffness parameters during assembly should result in a combination that also lies near this ridge. As mentioned earlier, it is only beneficial to make the system more compliant from the optimized parameters, since increasing the stiffness of the WAM would most likely make any jamming problems worse. The best strategy to meet these goals while defining the range of compliance parameters available to the variable compliance controller is to plot a line with the same slope as the ridge, descending from the optimum parameters until it meets a minimum stiffness boundary. The limiting parameter in this case is the rotational stiffness, so this is where the line must terminate. The resulting minimum compliance parameters are shown below.

$$K_{x_{\min}} \approx 200 \frac{N}{m} \quad K_{\theta_{\min}} = 2.75 \frac{N-m}{radian} \quad L = 0.01 \text{ meters}$$

The line drawn in figure 7-10 represents all the possible stiffness combinations that can be input into the impedance controller of the peg's WAM to guarantee successful insertion and system stability. The slope of this line is important because it indicates the proportion in which the lateral and rotational stiffness gains should be decreased from their optimum values to maintain a guaranteed successful system as insertion

displacement errors are experienced. To fully define this relationship, a limit on the maximum allowable insertion displacement error must be defined. From experimentation, it was found that setting this limit to 0.03 meters provides good behavior. This means the error between the desired position of the tip of the peg and its actual position must never exceed three centimeters.

To define the behavior of the variable compliance controller, the optimum and minimum physical stiffnesses must be converted back into controller gains. This was done using tables 4.2 and 4.3 and linear interpolation. The results are shown below.

$$\begin{aligned}
 K_{x_{optimum}} &\approx 294 & K_{\theta_{optimum}} &\approx 3.68 \\
 K_{x_{min}} &\approx 119 & K_{\theta_{min}} &\approx 1 & Error_{max} &= 0.03 \text{ meters}
 \end{aligned}$$

Using these values, the adaptive compliance controller equations can be defined as a function of displacement error as shown below. These equation will constitute the control law of the variable compliance controller.

$$K_x = K_{x_{optimum}} - \frac{K_{x_{optimum}} - K_{x_{min}}}{Error_{max}} (Error_{actual}) = 294 - 5833.3(Error_{actual}) \quad (7.1)$$

$$K_\theta = K_{\theta_{optimum}} - \frac{K_{\theta_{optimum}} - K_{\theta_{min}}}{Error_{max}} (Error_{actual}) = 3.68 - 89.33(Error_{actual}) \quad (7.2)$$

These are the equations that are entered into the controller shown in the figure 6-13 to vary the stiffness gains of the impedance controller as a function of insertion error. Someone could ask why the system would need to deviate from the optimum parameter values during assembly. While it is true that the optimum parameters theoretically guarantee successful assembly for the specific parameters input into *modeFrontier*, there are still many other factors that could negatively influence the system. In the vast majority of these cases, the solution to jamming is to make the system more compliant in the directions normal to the insertion motion's constraints so that the peg and hole can more easily align themselves in the presence of contact forces. The stiffness controller is designed to maintain the optimum values until it detects that there is an error that could lead to jamming. Thus it is only in these situations that the parameters are commanded to temporarily change to compensate for modeling errors that would have otherwise led to jamming.

CHAPTER 8

SYSTEM PERFORMANCE

With the completion of the compliance parameter design, the entire system was ready to be physically run and tested. The stiffness control equations were input into the adaptive compliance controller and the desired compliance center location and damping gain were input into the impedance controller for the WAM holding the peg. The constant compliance parameters were also input into the impedance controller for the WAM holding the hole and at this point, the system was complete and could be run. Next, a trajectory was defined for each WAM that held the hole compliantly still while the peg followed a horizontal trajectory in the X - Z plane to perform the insertion. A small dead time was also programmed before the trajectory was set to begin to allow the peg and hole to align themselves as the finite state machine builds the trajectory compensation vectors. Once this was completed, the system is able to perform the assembly. Pictures of each stage of the successful assembly process are shown in figure 8-1 below.

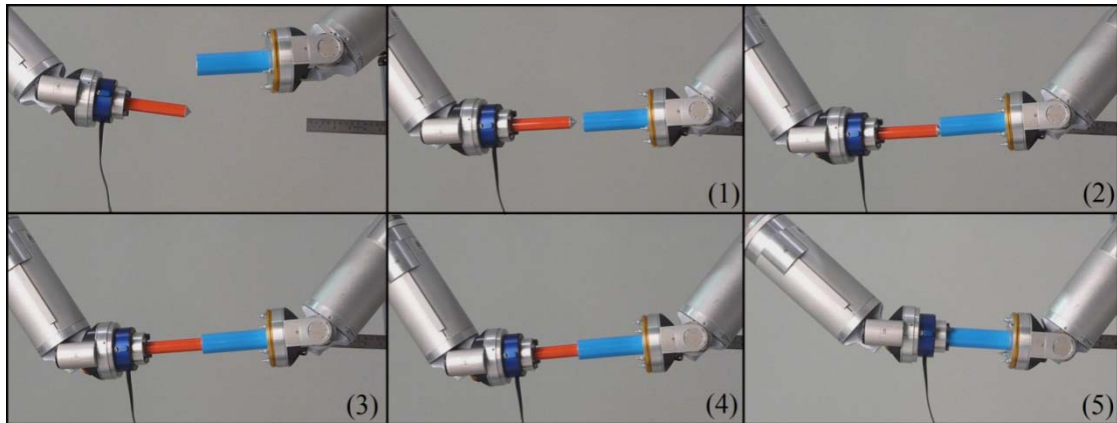


Figure 8-1. Images from different steps of a successful peg and hole insertion operation. The first panel shows the initial position of the peg and hole. Panel one shows the peg and hole after they have been aligned by the visual compensation system. Panels two through five refer to chamfer crossing, one-point contact, two-point contact, and successful assembly with line contact as described by figure 5-1.

During the insertion shown in figure 8-1, the system was also recording force and torque measurement from the JR3 attached to the peg. As discussed in Chapter 5, the very good alignment performance of the visual compensation controller practically eliminates all insertion forces related to chamfer crossing and one-point contact. This was apparent in the insertion force history recorded during the robotic insertion, as there is only one measureable contact state in the data. One of the goals of this thesis was to achieve human-like performance for peg and hole insertion. To quantify the results of the robotic system relative to this goal, the peg end-effector was disconnected from the WAM and held by a human, who then manually performed the insertion of the peg into the hole, which was still compliantly supported by the other WAM. This insertion force history was also recorded and it was again found that the reaction forces due to chamfer crossing and one-point contact were almost non-existent. This could also be the result of performing relatively slow insertion in both cases, since faster insertion processes would

naturally incur larger impact forces for all states of assembly. While comparing insertion force histories, it was also deemed beneficial to show the correlation between the actual insertion force history measurements and the predicted insertion force history produced by equation (5.45). Figure 8-2 below shows the insertion force histories for the robotic insertion, human insertion, and predicted insertion.

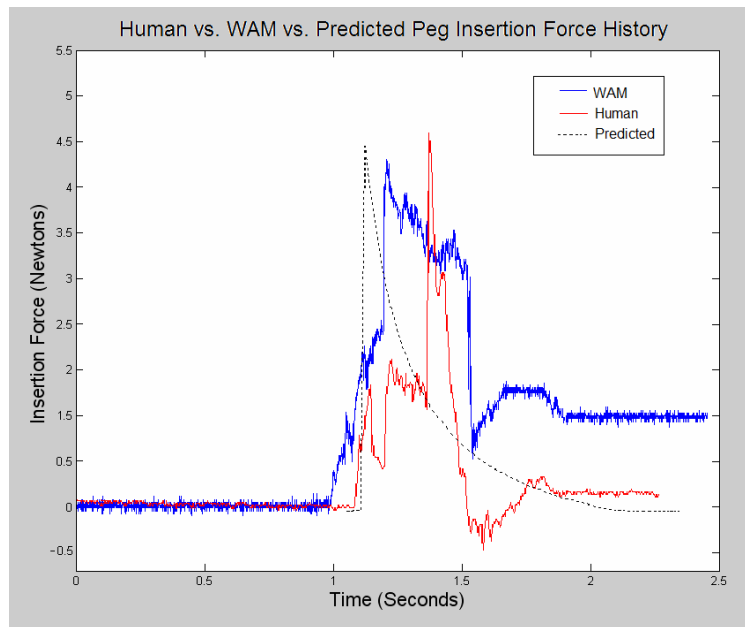


Figure 8-2. Recorded insertion force histories for peg and hole insertions performed by a human, WAM robot, and by a theoretical system.

Figure 8-2 shows that the results of all systems are all quite close. All the values are of the same order of magnitude, with the peak insertion force being almost identical between the three insertion force histories. This can be taken to mean two things. First, these results validate the two-point contact system model from Chapter 5 that was used for optimization since it accurately reflects the behavior of the physical system. Second, this figure supports the claim that the goal of creating a robotic peg and hole insertion

system with human-like performance was achieved for this experimental case, since the system was successful and generated similar levels of insertion force

While the insertion system was running, the *Simulink* system-level controller model was also recording data from the system. This included the values of the compensation vectors, the desired trajectory points, the actual trajectory points achieved by the WAM, and the stiffness gains being sent to the peg's impedance controller. Using this data, it would be beneficial to verify that the system-level controllers behave like they were designed to. The trajectory compensation system has already been proven to work very well in Chapter 6, so the performance of the variable compliance controller should now be verified using the experimental data. To do this, the plot shown in figure 8-3 was created from the data recorded by the system. This plot shows the insertion trajectory error and the corresponding changes in the stiffness parameters sent to the impedance controller as a function of insertion time.

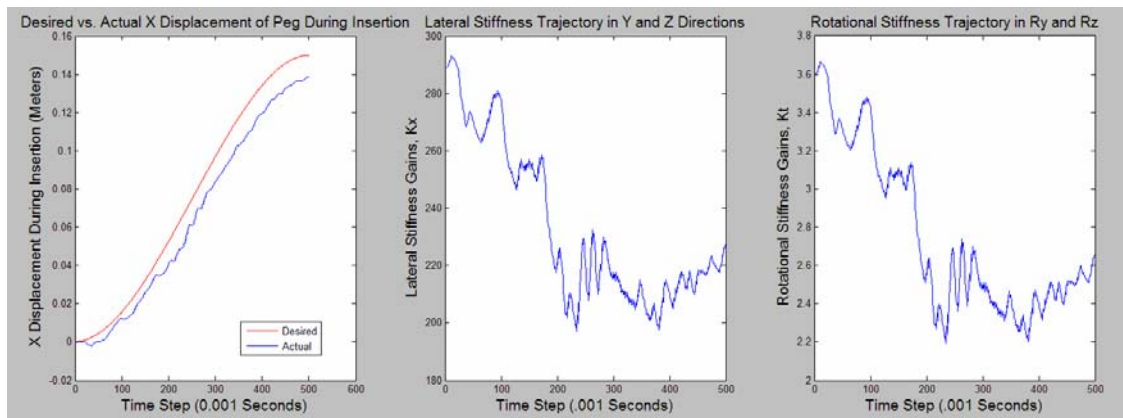


Figure 8-3. Relationship between stiffness gain compensation and the error between the desired and actual positions of the tip of the peg along the axis of insertion.

Figure 8-3 shows that there is almost always an error between the desired and actual positions of the tip of the peg during insertion. This is due to the contact forces between the peg and the hole that impede the progress of the insertion due to the small clearance between the parts. This assumption is supported by the otherwise near perfect free-space tracking performance of the impedance controlled WAM in the X direction when it is not performing insertion. A comparison of the trajectory following performance for free-space movements and insertion movements is given in figure 8-4.

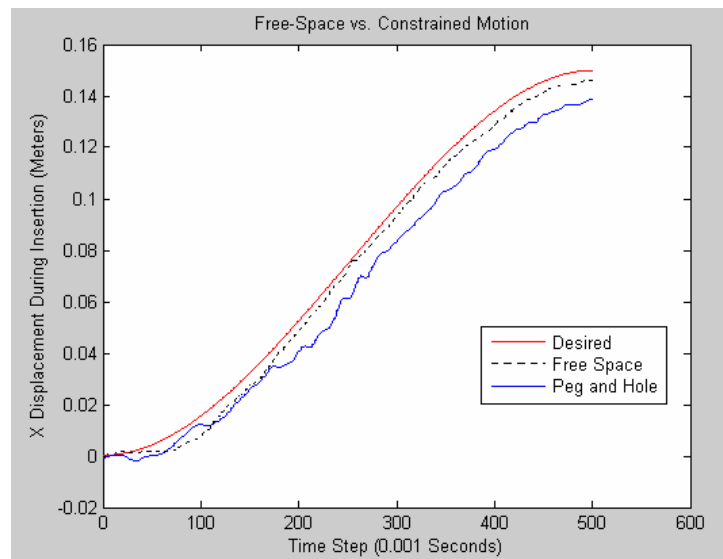


Figure 8-4. Comparison of the trajectory following performance of a WAM operating in free-space versus when it is performing peg and hole insertion in the X direction with $K_x = 700$. Notice the additional error imposed on the movement due to the peg and hole interaction.

The histories of the stiffness gains as they are compensated to accommodate the positional error and its associated increase in insertion force are shown in figure 8-3. These histories show that the variable stiffness controller is behaving correctly. The first thing to notice is that the shapes of the gain histories for the lateral and rotational

stiffnesses are identical. This is expected since the system was designed to simultaneously raise and lower these stiffness parameters to maintain the proper force relations to avoid jamming. It should also be noticed that neither gain was lowered all the way to its minimum, which suggests that the predefined maximum insertion position error was well defined during the derivation of the variable compliance control equations. Last, it should also be noticed that the general trend of the system is to become more compliant as the peg progresses into the hole. This is also logical. The reason the system must become more compliant as the insertion progresses is because it must accommodate the contact forces that result from the constraints imposed on the peg by the inside of the hole. As the peg progresses farther into the hole, its motion becomes more constrained, as demonstrated by the wiggle angle and insertion depth relation. So the system must become more compliant as a result. It should also be noticed that the gains started to rise again towards the end of the assembly, indicating that the peg had transitioned from two-point contact to less restrictive line-contact as the successful assembly stage was approached. This shows that the variable compliance controller was decreasing the compliance of the system to return to the optimum compliance settings as the jamming forces applied to the peg were also decreasing.

Now that the system has been proven to be successful, it should also be shown that the insertion process is less reliable without it. After twenty-five runs with the system fully functioning, the system was successful 100% of the time. The peg and hole never jammed and the insertion was always completed. During other experiments, the WAM robots were run in a near position control state with lateral and rotational impedance controller stiffness gains set to a constant 2000 and 5, respectively. Not only did the

system fail every time, but it also developed insertion forces that were about five times larger than those developed by the variable compliance system. The insertion force history for a trial of this position controlled experiment is shown in figure 8-5.

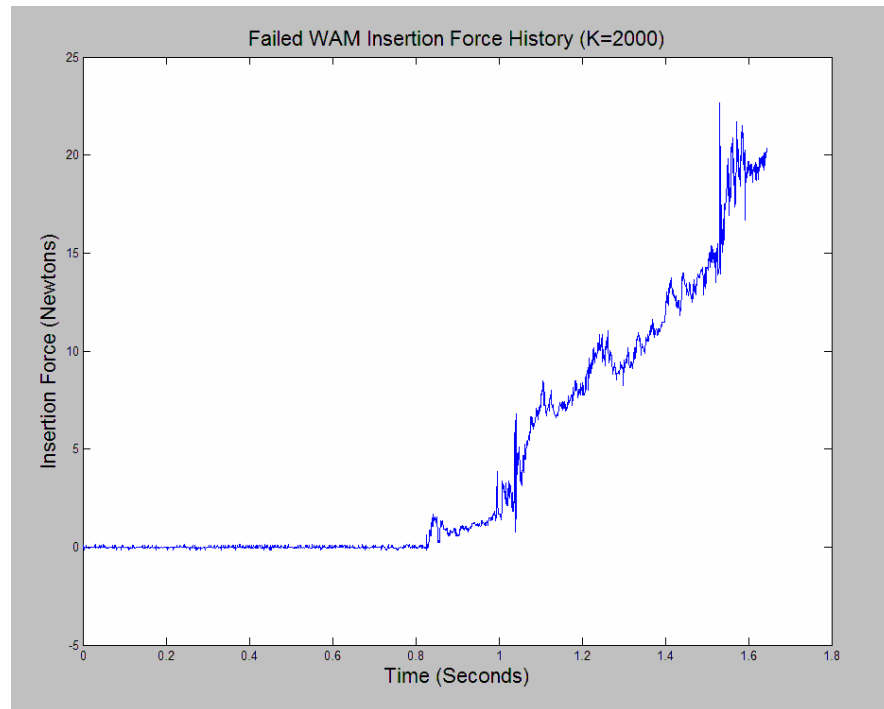


Figure 8-5. Insertion force history for the attempted position controlled peg and hole insertion with stiffnesses gains set to a constant [2000 2000 2000 5 5 5].

Next, the system was run with the visual trajectory compensation turned on, but the lateral and rotational stiffness gains were set to 400 and 4, respectively, and the variable compliance controller was turned off. Even with these reasonable gains that are only slightly beyond the system's optimum, the system still failed four out of five times. At times when the initial conditions were perfect, the system did succeed, but this happened infrequently. This lends some credibility both to the variable compensation controller as well as the optimized parameters found with *modeFrontier*. An example of

the kind of behavior experienced with this setup during a jam is shown in the figure 8-6. In this figure, the peg is aligned with the hole due to the visual compensation system and it successfully makes it past the chamfer crossing and one-point contact states. However, a small rotational error that it most likely immeasurable has caused the peg to jam inside of the hole during two-point contact. Without the stiffness controller to increase the compliance of the system by decreasing the stiffness gains of the impedance controller, the peg is unable to advance any farther into the hole.

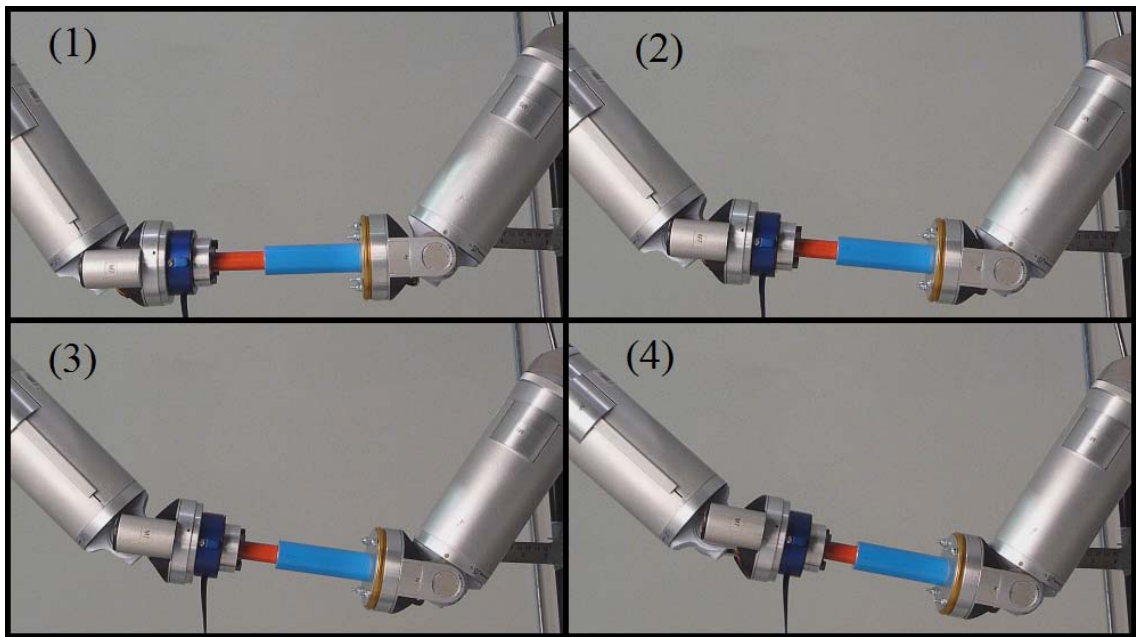


Figure 8-6. Pictures from a failed peg and hole insertion process attempted without the variable compliance system.

The JR3 force sensor was also recording the insertion force history during this failed attempt. This data is shown as a function of time in figure 8-7. Since the stiffness gains were set near the optimized parameters, the peak insertion force generated by the insertion WAM is only marginally higher than it was for the successful insertion

performed by the optimized system. However, it is obvious that this was an unsuccessful assembly attempt and that the parts had become jammed since the reaction forces were never accommodated by the system. This caused the insertion force to continue to grow as a function of increasing positional error along the axis of insertion in an attempt to force the peg into the hole. This instead created a commensurately larger moment that pushed the force relationship out of the jamming diagram's boundaries and the system failed. This final experiment also proves the benefits of using the variable compliance controller for peg and hole assembly.

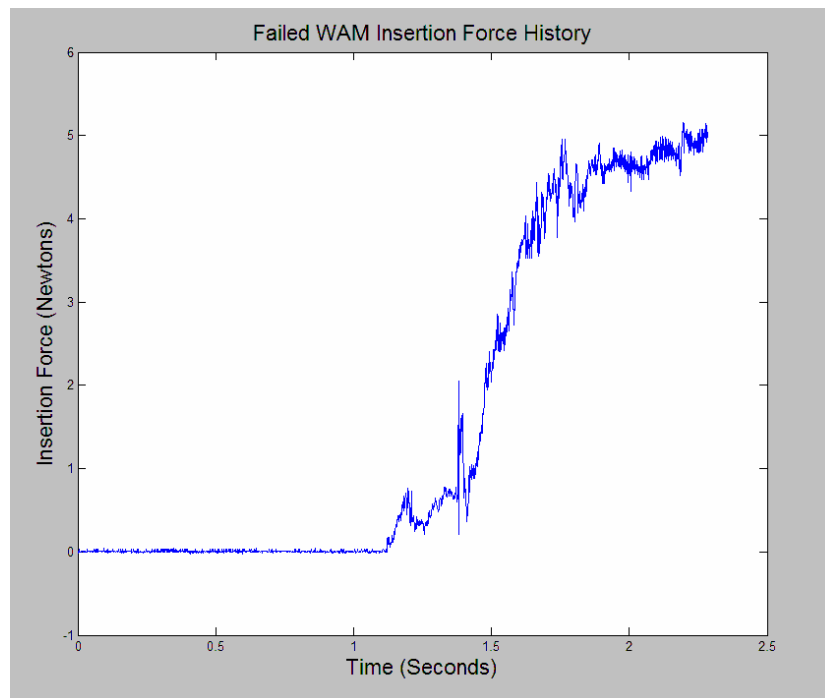


Figure 8-7. Insertion force trajectory for a peg and hole insertion experiment that jammed before completion. This experiment was run without the variable compliance controller and with constant stiffness gains set to [700 400 400 1 4 4].

CHAPTER 9

CONCLUSION

9.1 Review of Thesis

Successful peg and hole assembly systems allow the peg to accommodate forces that arise from different contact states that naturally occur during insertion. Typically, robotic insertion systems are composed of a position or force controlled robot that are fitted with compliant RCC wrist to insert a peg into a hole that is temporarily fixed to the environment. Using similar design principles, a variable compliance control system was produced and utilized in a dual seven DOF robotic arm system that performed rigid peg and hole assembly with human-like performance and a success rate of 100% after twenty-five experimental trials. In addition to the variable compliance control system itself, a novel finite state machine with visual feedback was developed to modify each robot's desired trajectory commands to compensate for the inevitable Cartesian position error associated with impedance control. Both of these components are unlike any other systems in published research, and they work together to satisfy the constraints of the wedging and jamming diagrams that dictate the success of peg and hole assembly. Finally, the unique use of jamming diagram concepts and coupled stability analysis with *modeFrontier* optimization represents a new design method that was proven to produce realistic impedance control parameters to meet a set of specific design goals.

9.2 Future Work

The topic of future work can be divided into two categories: system adaptation and system extension. System adaptation would include changing certain aspects of the system developed in this thesis to allow it to complete other tasks. For example, the square peg and hole problem would require different system modeling equations along with a different vision and compliance control system due to the non-axisymmetric properties of the prismatic peg. Similarly, high-speed peg and hole systems would benefit from additional system modeling equations to account for high-frequency dynamics or impact modeling.

System extension, on the other hand, implies changing some fundamental idea or function of the work. For example, a machine learning algorithm could be substituted for both the system modeling and optimization sections of the current design process. This would greatly simplify the system by eliminating the majority of the controller design work. The complete variable compliance system would operate as it is does now. However, it would need a learning period to establish the optimum and minimum impedance control parameters, as well as define the optimum proportions in which to vary the rotational and lateral stiffness parameters. This could be done using a reinforcement learning scheme that rewards lower insertion forces and successful assembly while varying the impedance controller variables. While this system lacks the ability to be 100% successful from the first time it is turned on, it would result in a system that needed no redesign to accomplish different tasks.

Another example of system extension would be the application of this type of system to the problem of disassembly. Much like the peg and hole problem, robotic

disassembly would require the robot to work in a very constrained environment with a specific impedance required to remove parts. While the problem of task planning would need to be solved by another body of research, the design for interaction and robot control could be performed in much the same way as this work.

REFERENCES

- [1] Nevins, J. L., Whitney, D. E., *Concurrent Design of Products and Processes: A strategy for the next generation in manufacturing*, McGraw-Hill Publishing Company, 1989.
- [2] Boothroyd, G., Dewhurst, P., Knight, W., Dekker, M., *Product Design for manufacture and Assembly, Second Edition, Revised and Expanded*, Marcel Dekker Inc., New York, NY, 2002.
- [3] Qiao, H., Dalay, B. S., Knight, J. A. G., "Robotic Assembly Operation Strategy Investigation Without Force Sensors Through the Research on Contact Point Location and Range of Peg Movement," *Proceedings of the Institution of Mechanical Engineers. Part B, Journal of Engineering Manufacture*, Vol. 210, 1996, p. 471-485.
- [4] Asada, H., Kakumoto, Y., "The Dynamic Analysis and Design of a High-Speed Insertion Hand Using the Generalized Centroid and Virtual Mass," *ASME Journal of Dynamic Systems, Measurements, and Control*, Vol. 112, 1990, p. 120-125.
- [5] Whitney, D., "Quasi Static Assembly of Compliantly Supported Rigid Parts," *ASME Journal of Dynamic Systems Measurement and Control*, Vol. 104, 1982, p.65-77.
- [6] Peshkin, M. A., "Programmed Compliance for Error Corrective Assembly," *IEEE Transactions on Robotics and Automation*, Vol. 6, No. 4, August 1990, p. 473-482.
- [7] Pai, D. K., Leu, M. C., "Uncertainty and Compliance of Robot Manipulators with Applications to Task Feasibility," *The International Journal of Robotics*, Vol. 10, No. 3, 1991, p. 200-213.
- [8] Leu, M. C., Jia, Y. L., "Mating of Rigid Parts by a Manipulator with Its Own Compliance," *Transactions of the ASME, Journal of Engineering for Industry*, Vol. 117, May 1995, p. 240-247.
- [9] Sturges, R. H., Jr., and Laowattana, S., "Design of an Orthogonal Compliance for Polygonal Peg Insertion," *Transactions of the ASME, Journal of Mechanical Design*, Vol. 118, March 1996, p. 105-113.
- [10] Sturges, R. H., Jr., Laowattana, S., "Virtual Wedging in Three-Dimensional Peg Insertion Tasks," *Transactions of the ASME, Journal of Mechanical Design*, Vol. 118, March 1996, p. 99-105.
- [11] Asada, H., Kakumoto, Y., "The Dynamic RCC Hand for High-Speed Assembly," *Proceedings of the IEEE Conference on Robotics and Automation*, 1988, p. 120-126.

- [12] Sangcheol Lee, "Development of a New Variable Remote Center Compliance (VRCC) with Modified Elastomer Shear Pad (ESP) for Robot Assembly," *IEEE Transactions on Automation Science and Engineering*, Vol. 2, No. 2, April 2005, p. 193-198.
- [13] Albu-Schaffer, A., Ott, C., Hirzinger, G., *A Unified Passivity Based Control Framework for Position, Torque and Impedance Control of Flexible Joint Robots*, Report of the Institute of Robotics and Mechatronics, German Aerospace Center.
- [14] Morita, T., Sugano, S., "Development and Evaluation of Seven-D.O.F. MIA ARM," *Proceedings of the 1997 IEEE International Conference on Robotics and Automation*, Albuquerque, NM, April 1997, p. 462-467.
- [15] Lozano-Perez, T., Mason, M. T., Taylor, H., "Automatic Synthesis of Fine-Motion Strategies for Robots," *International Journal of Robots*, Vol. 3, No. 1, 1984, p. 65-96.
- [16] Raibert, M. H., Craig, J. J., "Hybrid Position/Force Control of Manipulators," *ASME Journal of Dynamic Systems Measurement and Control*, Vol. 102, 1981, p. 126-133.
- [17] Mason, M. T., "Compliance and Force Control for Computer Controlled Manipulators," *IEEE Transactions on Systems, Man, and Cybernetics*, Vol. SMC-11, No. 6, June 1981, p. 418-432.
- [18] Anderson, R. J., Spong, M. W., "Hybrid Impedance Control of Robotic Manipulators," *IEEE Journal of Robotics and Automation*, Vol. 4, No. 5, Oct 1988, p. 549-557.
- [19] Whitney, D., "Historical Perspective and State of the Art in Robot Force Control," *Journal of Robotics Research*, Vol. 6, No. 1, 1987, p. 3-14.
- [20] Gravel, D. P., Newman, W. S., "Flexible Robotic Assembly Efforts at Ford Motor Company," *Proceedings of the 2001 IEEE International Symposium on Intelligent Control*, Sept 2001, p. 173-182.
- [21] Wang, J., Tao, X., Cho, H., "Microassembly of Micro Peg and Hole Using an Optimal Visual Proportional Differential Controller," *Proceedings of IMechE*, Vol. 222, Part B: *Journal of Engineering and Manufacturing*, 2008, p. 1171-1182.
- [22] Broenink, J. F., Tiernego, M. L. J., "Peg-in-Hole Assembly Using Impedance Control with a 6 DOF Robot," *Simulation in Industry, Proceedings of the 8th European Simulation Symposium*, Oct 24-26, 1996, Genoa, Italy, 1996, p. 504-509.
- [23] Pauli, J., Schmidt, A., Sommer, G., "Servoing Mechanisms for Peg-in-Hole Assembly Operations," *Robot Vision 2001, LNCS 1998*, 1998, p. 157-166.

- [24] Cutkosky, M. R., Kao, I., "Computing and Controlling the Compliance of a Robotic Hand," *IEEE Transactions on Robotics and Automation*, Vol. 5, 1989, p. 151-165.
- [25] Kang, S. H., Jin, M., Chang, P. H., "A Solution to the Accuracy/Robustness Dilemma in Impedance Control," *IEEE/ASME Transactions on Mechatronics*, Vol. 14, No. 3, June 2009, p. 282-294.
- [26] Valency, T., Zacksenhouse, M., "Accuracy/Robustness Dilemma in Impedance Control," *Transactions of ASME, Journal of Dynamic Systems, Measurement, and Control*, Vol. 125, September 2003, p. 310-319.
- [27] Almeida, F., Lopes, A., Paulo, A., *Force-Impedance Control: A New Control Strategy of Robotic Manipulators*, IDMC Report, Polo FEUP, n.d., p. 1-12.
- [28] Hsia, T. C., Jung, S., "Stability and Convergence Analysis of Robust Adaptive Force Tracking Impedance Control of Robot Manipulators," *Proceedings of the 1999 IEEE/RSJ International Conference on Intelligent Robots and Systems*, 1999, p. 635-640.
- [29] Hogan, N., "Impedance control: An Approach to Manipulation," *Transactions of the ASME Journal of Dynamic Systems, Measurement, and Control*, Vol. 107, March 1985, p. 1-24.
- [30] Fasse, E. D., Broenink, J. F., "A Spatial Impedance Controller for Robotic Manipulation," *IEEE Transactions on Robotics and Automation*, Vol. 13, No. 4, August 1997, p. 546-557.
- [31] Fasse, E. D., "Simplification of Compliance Selection Using Spatial Compliance Control," *Proceedings of the ASME Dynamic Systems and Control Division*, 1995, p. 193-197.
- [32] Surdilovic, D., "Robust Control Design of Impedance Control for Industrial Robots," *Proceedings of the 2007 IEEE/RSJ International Conference on Intelligent Robots and Systems*, 2007, p. 3572-3579.
- [33] Buchili, J., Theodorou, E., Stulp, F., Schaal, S., *Variable Impedance Control: A Reinforcement Learning Approach*, Report of the Computational Learning and Motor Control Lab, USC, 2009, p. 1-8.
- [34] Kelly, R., Carelli, R., Amestsgui, M., Ortega, R., "Adaptive Impedance Control of Robot Manipulators," *International Journal of Robotics and Automation*, Vol. 4, No. 3, 1989, p. 134-141.
- [35] Kelly, R., Carelli, R., "Unified Approach to Adaptive Control of Robotic Manipulators," *Proceedings of the 27th Conference on Decision and Control*, 1988, p. 1598-1603.

- [36] Soltanpour, M. R., Shafiei, S. E., "Design and Stability Analysis of a Robust Impedance Control System for a Robot Manipulator," *Studies in Informatics and Control*, Vol. 19, No. 1, March 2010, p. 5-16.
- [37] Pourboghraat, F., "Virtual Adaptive Compliant Control for Robots," *International Journal of Robotics and Automation*, Vol. 4, No. 3, 1989, p. 148-158.
- [38] Platt, R., Jr., Abdallah, M., Wampler, C., *Multi-Priority Cartesian Impedance Control*, Report, General Motors Manufacturing Systems Research Lab, 2008, p. 1-7.
- [39] Nakabo, Y., Ishikawa, M., "Visual Impedance Using 1ms Visual Feedback System," *Proceedings of the 1998 IEEE International Conference on Robotics & Automation, Leuven, Belgium*, May 1998, p. 2333-2338.
- [40] Kelly, R., Carelli, R., Amestegui, M., Ortega, R., "On Adaptive Impedance Control of Robot Manipulators," *The Institute of Electrical and Electronics Engineering, Computer Society Magazine*, n.d., p. 572-577.
- [41] Colbaugh, R., Seraji, H., Glass, K., "Direct Adaptive Impedance Control of Manipulators," *Proceedings of the 30th Conference on Decision and Control, Brighton, England*, Dec 1991, p. 2410-2415.
- [42] Jung, S., Hsia, T. C., Bonitz, R. G., "Force Tracking Impedance Control of Robot Manipulators Under Unknown Environments," *IEEE Transactions on Control Systems Technology*, Vol. 12, No. 3, May 2004, p. 474-483.
- [43] Liao, H. T., Leu, M. C., "Analysis of Impact in Robotic Peg-in-Hole Assembly," *Robotica*, Vol. 16, 1998, p. 347-356.
- [44] Newman, W. S., Dohring, M. E., "Augmented Impedance Control: An Approach to Impact Reduction for Kinematically Redundant Manipulators," *Proceedings of the IEEE International Conference on Robotics and Automation, Sacramento, CA*, 1991, p. 30-35.
- [45] Yoshida, K., *Impact Dynamics Representation and Control with Extended-Inversed Inertia Tensor for Space Manipulators*, Report, Tokyo Institute of Technology, Department of Mechano-Aerospace Engineering, p. 1-10.
- [46] Youcef-Toumi, K., Gutz, D. A., "Impact and Force Control: Modeling and Experiments," *Journal of Dynamic Systems, Measurement, and Control*, Vol. 116, March 1994, p. 89-98.
- [47] Xia, Y., Yin, Y., Chen, Z., "Dynamic Analysis For Peg-in-Hole Assembly With Contact Deformation," *International Journal of Advanced Manufacturing Technology*, Vol. 30, 2006, p. 118-128.

- [48] Kim, M. G., Wu, C., "A Formal Part Mating Model for Generating Compliance Control Strategies of Assembly Operations," *IEEE International Conference on Robotics and Automation*, 1990, p. 611-616.
- [49] Peshkin, M. A., "Programmed Compliance for Error Corrective Assembly," *IEEE Transactions on Robotics and Automation*, Vol. 6, No. 4, August 1990, p. 473-483.
- [50] Huang, X., Hu, J., Du, K.-L., Zhang, B.-B., "Dynamic Analysis of Assembly Process with Passive Compliance for Robot Manipulators," *Proceedings 2003 IEEE International Symposium on Computational Intelligence in Robotics and Automation*, July 16-20, 2003, Kobe, Japan, 2003, p. 1168-1174.
- [51] Yanqiong, F., Jianfeng, W., Xifang, Z., "Study on Three Dimensional Dual Peg-in-hole in Robot Automatic Assembly," *Industrial Robotics: Programming, Simulation and Application*, Germany, Dec 2006, p. 702-726.
- [52] Sathirakul, K., Sturges, R. H., "Jamming Conditions for Multiple Peg-in-Hole Assemblies," *Robotica*, Vol. 16, 1998, p. 329-345.
- [53] Sturges, R. H., Sathirakul, K., "Modeling Multiple Peg-in-Hole Insertion Tasks," *Japan/USA Symposium on Flexible Automation*, Vol. 2, ASME, 1996, p. 819-821.
- [54] Taylor, R. H., Mason, M. T., Lozano-Perez, T., "Automatic Synthesis of Fine-Motion Strategies for Robots," *Massachusetts Institute of Technology Artificial Intelligence Laboratory, A.I. Memo 759*, Dec 1983, p. 1-34.
- [55] Qiao, H., Tso, S. K., "Three-Step Precise Robotic Peg-Hole Insertion Operation With Symmetric Regular Polyhedral Objects," *International Journal of Production Research*, Vol. 37, No. 15, 1999, p. 3541-3563.
- [56] Huang, S., Schimmels, J. M., "Spatial Admittance Selection Conditions for Frictionless Force-Guided Assembly of Polyhedral Parts in Single Principal Contact," *IEEE Transactions on Robotics*, Vol. 22, No. 2, April 2006, p. 225-240.
- [57] Chung, S.-Y., Lee, D. Y., "Discrete Event Systems Approach to Fixtureless Peg-in-Hole Assembly," *Proceedings of the American Control Conference*, Arlington, VA, June 25-27, 2001, p. 866-872.
- [58] Bruzzone, L. E., Molfino, R. M., Zoppi, M., "Modelling and Control of Peg-in-Hole Assembly Performed by a Translational Robot," *Proceedings of the IASTED International Conference on Modeling, Identification, and Control*, Innsbruck, Austria, Feb 18-21, 2002, p. 512-517.

[59] Naghdy, F., Lukasiaks, J., "Neuro-Fuzzy Control of Robotics Peg-in-Hole Insertion," *Proceedings of International ICSC Congress on Intelligent Systems & Applications ISA'2000, Vol. 2*, 2000, p. 142-148.

[60] Gore, D., "A Stable Design for the State Design Pattern," *International Journal of Software Engineering and Its Applications, Vol. 3, No. 4*, October 2009, p. 33-50.

[61] Tarraf, D. C., Dahleh, M. A., Megretski, A., "Stability of Deterministic Finite State Machines," *2005 American Control Conference*, 2005, p. 3932-3936.

[62] Colgate, J.E., Hogan, N., "Robust Control of Dynamically Interacting Systems," *International Journal of Control, Vol. 47, No. 1*, 1988, p. 65-88.

[63] *ModeFrontier* product page from publishers website, Esteco, 23 March 2011, <www.esteco.com/home/by_esteco.html>.